Mechanisms of Complex Tissue Regeneration and the Functional Outcomes of Craniofacial Dysmorphology

by

Ke'ale W. Louie

A dissertation submitted in partial fulfillment
of the requirements for the degree of
Doctor of Philosophy
(Oral Health Sciences)
in the University of Michigan
2020

Doctoral Committee:

Professor Yuji Mishina, Chair
Assistant Professor Justin A. Colacino
Professor Geoffrey E. Gerstner
Professor Jan C.C. Hu

Ke’ale W. Louie

keale@umich.edu

ORCID iD: 0000-0003-3008-1828

Dedication

To all my friends and family who have tolerated me in Michigan and across different time zones.

Acknowledgements

I would like to first thank my advisor Yuji Mishina for his mentorship, support, and patience since 2013. Your belief in my abilities has been unwavering and has kept me motivated me through all sorts of setbacks. Be they scientific or philosophical, your teachings were also critical for my confidence and development into an independent thinker. I would also like to thank my committee members Geoffrey Gerstner, Jan Hu, and Justin Colacino for their guidance and mentorship throughout my entire graduate school experience. Each of you were invaluable during my journey and your influences can be felt throughout this work.

To my past mentors and present collaborators, thank you for your help, input, and support to make parts of this dissertation possible. Alon Kahana, members of the Kahana lab (Alfonso Saera-Vila, Phil Kish, Amy Robbins, Estelle Chiari-Fort, Amy Stevens, Yi Zhao, Chrissy Tingle, and Curtis Heisel), Brenda Bohnsack, and members of the Bohnsack lab (Bahaar Chawla and Antionette Williams) welcomed me into their zebrafish family and, together, we achieved great things in a very short time. Susan Williams and members of the Williams lab (Stephane Montuelle and Rachel Olson) helped us push the bounds of oral function assessments and I expect much more to come from this continued collaboration.

I would also like to thank the Oral Health Sciences Program and Contracts and Grants Service Center for their help at every step along the way. Without Kimberly Smith, Amy Watson, and Jennifer Linzmeier, I'd be completely lost, much poorer, and unable to

focus on anything scientific. To my OHS buddies, thank you for tolerating my uniqueness since interviewing in 2012. You will all be lifelong friends and I look forward to seeing where and what we end up doing with our lives.

Finally, I would like to thank the past and present members of the Mishina lab – Honghao Zhang, Haichun Pan, Maiko Omi, Hiroki Ueharu, Jingwen Yang, Anshul Kulkarni, and Afriti Chinoy – and again Yuji Mishina. From listening to practice talks to sorting pipette tips, we have been though a lot and I am grateful for your support, friendship, and tolerance of my unique scientific ideas.

Contents

List of Figures

List of Tables

Abstract

There is a clinical need to restore craniofacial tissues affected by disorders of traumatic and/or congenital etiology. Effective therapies within this specialized region must achieve anatomic regeneration while also restoring function. The work in this dissertation attempts to identify mechanisms underlying the former while simultaneously elucidating the latter using mastication as a readout of craniofacial tissue interactions. The global hypothesis is that perturbation of gene expression during adult craniofacial tissue regeneration has functional outcomes that extend beyond the immediately dysmorphic structures. It was additionally hypothesized that: (1) genes differentially expressed at early time points play unique roles during cellular reprogramming and adult muscle regeneration and (2) fundamental changes in dental and craniofacial morphology decrease chewing efficiency.

Zebrafish possess robust regenerative capabilities as demonstrated by the rapid (i.e., 7-10 day) anatomic and functional regeneration of individual craniofacial muscles following >50% surgical resection. Analysis of differentially expressed genes (DEG) at two time points (i.e., 9 and 18 hours post injury(hpi)) within actively regenerating craniofacial muscle identified over 6000 candidates that could play a role during craniofacial muscle regeneration. Subsequent clustering of these DEG by temporal expression patterns then revealed subsets of genes which were transiently upregulated at only the 9hpi (early) or 18hpi (late) time points. Among the early expressed genes were known epigenetic regulators including *ezh2*, *prmt5*, and *prmt7*. *In vivo* knockdown experiments revealed that these genes were necessary for both cellular reprogramming and anatomic regeneration. This differed from late expressed genes such as *fn1a* which was

necessary for anatomic regeneration but not cellular reprogramming. Also among the early expressed genes were twist transcription factors, elements known to affect craniofacial muscle development and epithelial to mesenchymal transitions during tumorigenesis. Of the zebrafish twist paralogs, only *twist3* was necessary for cellular reprogramming and anatomic regeneration in adult zebrafish while *twist1a*, *twist1b*, and *twist2* only affected embryonic muscle development.

Ellis-van Creveld syndrome (EVC) is a rare genetic condition that affects the craniofacial region. However, the etiology of cephalometric differences and the functional outcomes of dental and craniofacial dysmorphology are poorly described in the literature. Use of an animal model for EVC in which a causative gene ortholog (i.e., *Evc2*) was conditionally knocked out (cKO) in neural crest cells revealed that changes in facial profile advanced with age and were secondary effects of a shortened anterior skull base. Further application of our *Evc2*-cKO model revealed that mastication parameters such as bite force and chewing rate were reduced as were molar surface area and complexity. No changes in chewing effectiveness suggested that behaviors such as longer feeding bouts may effectively compensate for anatomic deficits in the craniofacial region.

Investigation into the temporal regulation of adult tissue regeneration and gene subfunctionalization has led to the identification of multiple pathways that represent potentially druggable targets for future regenerative therapies. Assessment and characterization of the functional outcomes in states of congenital craniofacial dysmorphology provide insight into form-function relationships and represent potential metrics by which successful rehabilitation may be measured. However, future studies must further elucidate the additional mechanisms (e.g., histone modification) underlying tissue regeneration as well as assess adaptation by evaluating chewing function at additional developmental and/or post-acute injury time points.

Chapter 1: Introduction

1.1 Review of Craniofacial Muscle Regeneration

1.1.1 Extraocular Muscle Regeneration in Adult Zebrafish

Embryologically and functionally distinct from somitic muscles, craniofacial muscles are involved in many orofacial disorders with degenerative, inflammatory, neoplastic, and traumatic etiologies [1–3]. Mammalian myonuclei are described as postmitotic and muscle repair is limited by both the severity of tissue damage and the paucity of resident stem cells (i.e., satellite cells) available for tissue replacement [4–6]. As a result, tissue replacement following volumetric muscle loss involves a biomechanically inferior fibrotic mass that fills the tissue defect (i.e., form) but critically fails to restore contractile muscle properties (i.e., function) [7,8]. Craniofacial muscle regenerative therapies must therefore overcome the body's innately limited healing capacity while simultaneously addressing the unique physiology of muscles within this region.

Zebrafish are an excellent model for studying regeneration due to their ability to robustly repair tissues (e.g., bone, heart, retina, fin) following severe volumetric injuries [9–14]. This extensive repair, or rather whole tissue regeneration, also varies from mammalian models in that it relies on cellular reprogramming and dedifferentiation. Recent work has identified zebrafish extraocular muscles (EOMs) as convenient models for studying both anatomic and functional muscle regeneration in the craniofacial region [15]. Following ~50% muscle resection, regeneration occurs via the rapid dedifferentiation of residual myocytes into a mesenchymal-like cell pool that undergoes a proliferative burst then re-differentiates to replace the critical mass of lost tissue (Figure 1.1). This dedifferentiation-based process occurs without observable

contributions from Pax7-positive satellite cells, completes within a week post injury, and is not diminished by multiple rounds of injury.

Understanding the mechanisms underlying *de novo* craniofacial muscle regeneration in adult organisms is a topic with widespread clinical implications. Though directly relevant to tissue engineering strategies, the zebrafish EOM model may also provide insight regarding cell fate regulation and subfunctionalization amongst gene paralogs. Regardless, it is an invaluable tool that provides a rapid readout of restored form and function.

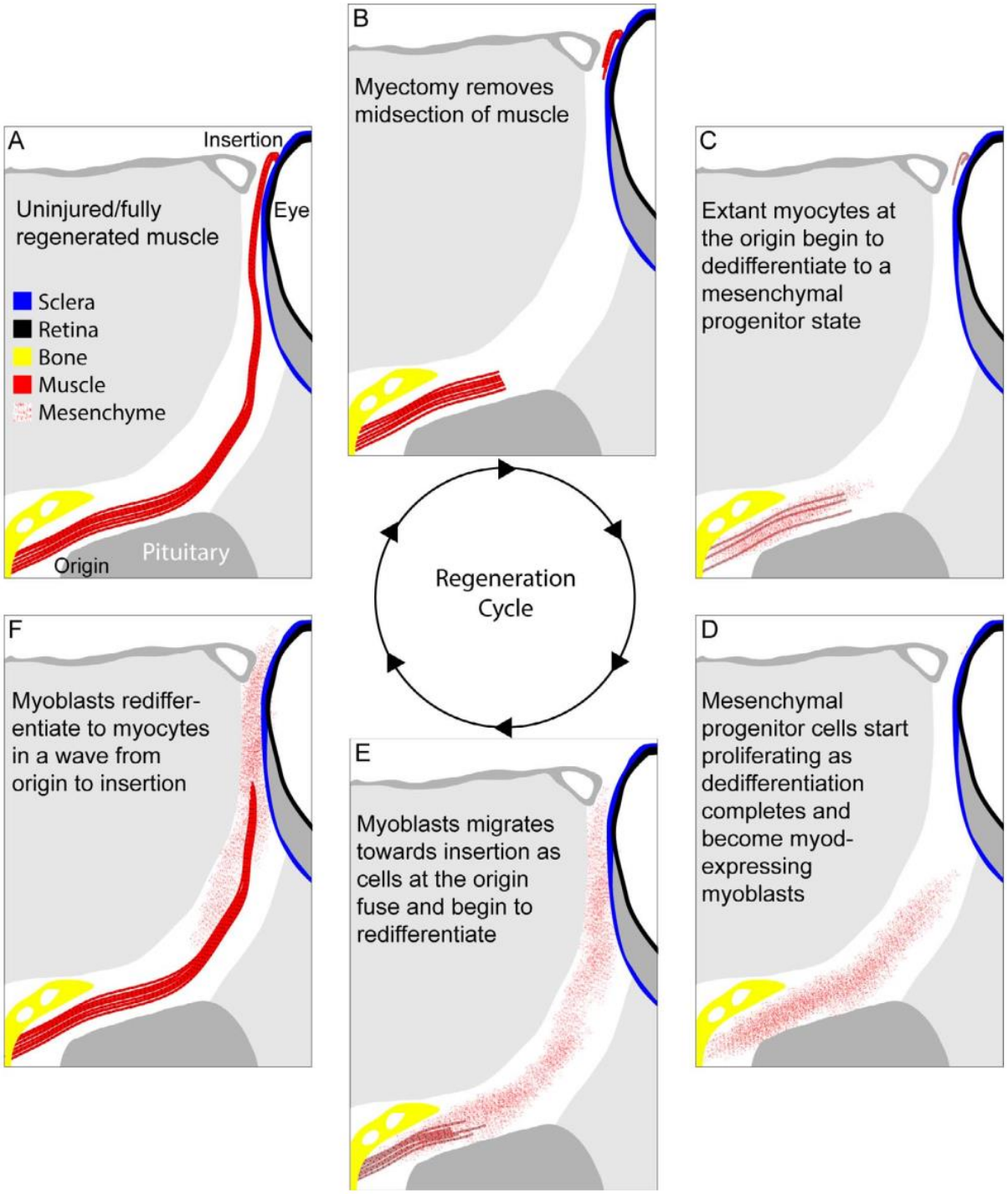

Figure 1.1: Model of EOM Regeneration
Model of EOM regeneration. Following myectomy, the residual muscle undergoes MMT consisting of myocyte reprograming, dedifferentiation, loss of apical cell polarity, and cell cycle reentry to become myoblasts. These proliferating progenitor cells migrate to repopulate the regenerating muscle, followed by fusion and redifferentiation.

1.1.2 References

1. Hall, J. G. Importance of Muscle Movement for Normal Craniofacial Development. *J. Craniofac. Surg.* 21, 1336–1338 (2010).
2. Laumonier, T. & Menetrey, J. Muscle injuries and strategies for improving their repair. *J. Exp. Orthop.* 3, (2016).
3. Sartore, S. *et al.* Fibre types in extraocular muscles: a new myosin isoform in the fast fibres. *J. Muscle Res. Cell Motil.* 8, 161–172 (1987).
4. Mauro, A. Satellite cell of skeletal muscle fibers. *J. Biophys. Biochem. Cytol.* 9, 493–495 (1961).
5. Snow, M. H. Myogenic cell formation in regenerating rat skeletal muscle injured by mincing I. A fine structural study. *Anat. Rec.* 188, 181–199 (1977).
6. Schmalbruch, H. & Lewis, D. M. Dynamics of nuclei of muscle fibers and connective tissue cells in normal and denervated rat muscles. *Muscle and Nerve* 23, 617–626 (2000).
7. Garg, K. *et al.* Volumetric muscle loss: Persistent functional deficits beyond frank loss of tissue. *J. Orthop. Res.* 33, 40–46 (2015).
8. Corona, B. T. *et al.* The promotion of a functional fibrosis in skeletal muscle with volumetric muscle loss injury following the transplantation of muscle-ECM. *Biomaterials* 34, 3324–3335 (2013).
9. Geurtzen, K. *et al.* Mature osteoblasts dedifferentiate in response to traumatic bone injury in the zebrafish fin and skull. *Development* 141, 2225–34 (2014).
10. Poss, K. D., Wilson, L. G. & Keating, M. T. Heart regeneration in zebrafish. *Science (80-.).* 298, 2188–2190 (2002).
11. Jopling, C. *et al.* Zebrafish heart regeneration occurs by cardiomyocyte dedifferentiation and proliferation. *Nature* 464, 606–609 (2010).
12. Thummel, R. *et al.* Inhibition of zebrafish fin regeneration using in vivo electroporation of morpholinos against fgfr1 and msxb. *Dev. Dyn.* 235, 336–346 (2006).
13. Thummel, R. *et al.* Characterization of Müller glia and neuronal progenitors during adult zebrafish retinal regeneration. *Exp. Eye Res.* 87, 433–444 (2008).
14. Singh, S. P., Holdway, J. E. & Poss, K. D. Regeneration of Amputated Zebrafish Fin Rays from De Novo Osteoblasts. *Dev. Cell* 22, 879–886 (2012).
15. Saera-Vila, A. *et al.* Myocyte Dedifferentiation Drives Extraocular Muscle Regeneration in Adult Zebrafish. *Invest. Ophthalmol. Vis. Sci.* 56, 4977–93 (2015).

1.2 Review of Ellis-van Creveld Syndrome (EVC)[1]

1.2.1 Background

First described in 1940, Ellis-van Creveld syndrome (EVC; MIM ID #225500) is a rare, recessive congenital disorder that results in a type of disproportionate dwarfism [1]. Affected individuals represent approximately 1 in every 60,000–200,000 live births with higher occurrence reported in offspring of consanguineous (e.g., first cousin) unions or monotypic populations [2,3]. In addition to short stature (Figure 1.2 A), other conspicuous signs of EVC include extra digits (i.e., polydactyly), dysmorphic faces, and dental anomalies [4]. While none of these directly confer shortened longevity, approximately 60% of patients suffer from underlying cardiac conditions, indicating widespread developmental effects.

Although EVC was known to occur more frequently in certain families and/or communities (e.g., the Pennsylvania Amish), several decades passed before the causative gene(s) (i.e., *EVC* and *EVC2/LIMBIN*) were identified. Mutations in either of these head-to-head genes located on human chromosome 4p were found to contribute to EVC and a dominant but phenotypically milder form called Weyers acrodental dysostosis (also known as Curry–Hall syndrome, WAD; MIM ID #193530)) [3,5]. The primary difference between EVC and WAD is the severity of clinical phenotypes and pattern of inheritance. Though mutations in *EVC* and *EVC2* account for the majority of the patients, there are still patients that present with EVC symptoms despite no mutations in either *EVC* or *EVC2* [6,7]. EVC is an autosomal recessive disorder and is associated with a more severe phenotype, specifically heart abnormalities, which are the main cause of morbidity. Since *EVC* and *EVC2* share limited homology, *EVC* and *EVC2* were named based on a historic timeline of mapping and cloning of causative genes for EVC, and thus they do not form a

[1] Published as Louie KW, Mishina Y, Zhang H. 2020. Molecular and Cellular Pathogenesis of Ellis-van Creveld Syndrome: Lessons from Targeted and Natural Mutations in Animal Models *J. Dev. Biol.* 8(25): https://doi.org/10.3390/jdb8040025.

gene family. In this manuscript, we use both *EVC2* and *LIMBIN* to describe this gene, because pathophysiologic function of this gene was firstly identified as a causative gene of Bovine chondrodysplastic dwarfism and named as *LIMBIN* [8].

Animal models of EVC have been critical for providing insight into disease pathogenesis (detailed in subsequent sections) [9–11]. The initial observation was from *EVC2/LIMBIN* mutant cattle that developed bovine chondrodysplastic dwarfism (BCD) (Figure 1.2 B and C). Studies of mice revealed phenotypes similar to cattle (Figure 1.2 C, E, and F), which is the result of reduced, but not eliminated, hedgehog (Hh) signaling. Both EVC and EVC2/LIMBIN proteins have also been shown to form a complex at the bottom of primary cilia. This has led to the classification of EVC as a ciliopathy or disorder of the primary cilia. Because the management of patients with EVC is currently limited to corrective therapy, deepened understanding of disease pathogenesis from animal models raises the possibility of targeted therapy and improved clinical outcomes.

The review highlights lessons in disease etiology learned from mouse models of EVC with targeted mutations in the causative genes. We will cover: (Section 1.1.2) molecular biology of EVC and EVC2/LIMBIN, (Section 1.1.3) human disease signs, (Section 1.1.4) dysplastic limb development, (Section 1.1.5) craniofacial anomalies, (Section 1.1.6) tooth anomalies, (Section 1.1.7) tracheal cartilage abnormalities, and (Section 1.1.8) EVC-like disorders in non-human species.

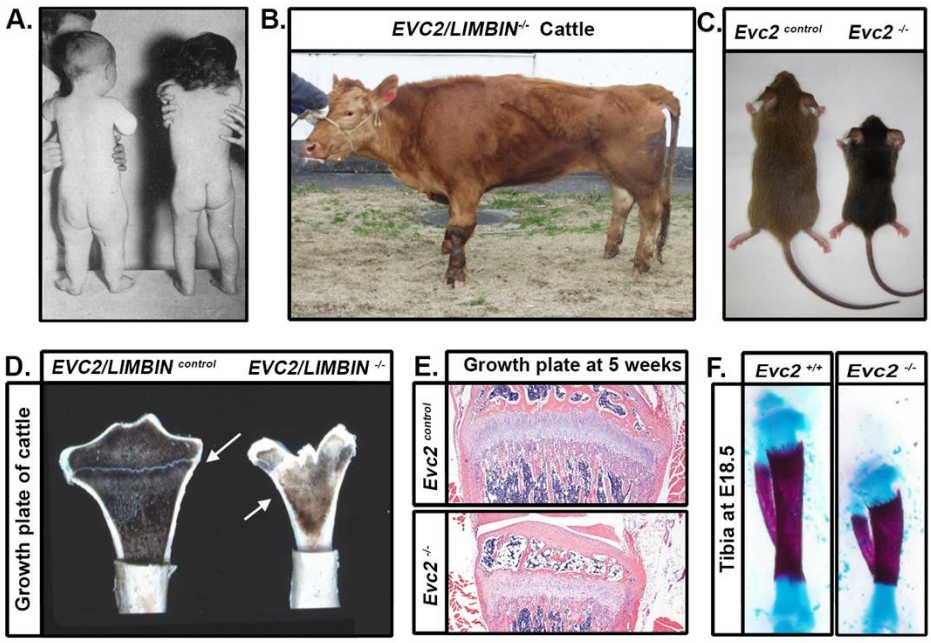

Figure 1.2: Individuals affected by EVC, LIMBIN mutant cattle, and Evc2/Limbin mutant mouse share similar dwarfism.
(**A**) A 20-month-old infant affected by EVC syndrome (left) and a 20-month-old infant without EVC syndrome (right) © BMJ. The infant with EVC syndrome has un-proportional shortened legs. (**B**) A *LIMBIN* mutant cattle bears apparent short legs. (**C**) *Evc2/Limbin* mutant mice with littermate controls exhibit a smaller body size at 5 weeks old. (**D**) *LIMBIN* mutant cattle have decreased size of growth plate (marked in white arrow) in appendicular bones. (**E**) The growth plate of tibia from *Evc2/Limbin* mutant mice demonstrate shorter and disorganized structure at 5 weeks old compared with control mice. Bars indicate 200 um. (**F**) Tibiae from E18.5 mouse embryos were stained with alcian blue for cartilage and alizarin red for bone. Tibiae from *Evc2/Limbin* mutant embryos are shorter than those in control littermates, although body size in these two groups are similar at this stage.

1.2.2 Primary Cilium, Ciliopathy, and EVC

Despite longstanding clinical description, it was not until the late 1990s and early 2000s that the two causative genes of EVC (i.e., *EVC* and *EVC2/LIMBIN*) were successfully mapped in human genomes [3,5]. Subsequent molecular studies have demonstrated that both EVC and EVC2/LIMBIN locate and play an important role within the primary cilium [9–12] (Figure 1.3 A and B). Cilia are rod-shaped microtubule-based surface structures present in nearly all vertebrate cells [13]. Cilia can be categorized into primary cilia and motile cilia, the former of which have

nine pairs of microtubule doublets and are immotile, and the latter of which have one more pair of microtubule doublets in the center of the nine pairs of microtubule doublets and can perform rotary movement [13], which is critical for the normal physiology of brain, lung, and sinus [14,15]. Different from motile cilia, which are only present in specific cells, primary cilia are present in nearly all vertebrate cells and they are critical for various aspects of development, post-development homeostasis, and diseases [16]. The unique receptor composition within the primary cilium makes it an important signaling center in vertebrate cells. Congenital mutations in a series of primary ciliary components leads to dysfunction of the primary cilium and results in syndromic disorders (termed ciliopathies) in which organogenesis during embryonic and postnatal development are affected. Studies in the past 15 years have demonstrated that the primary cilia are involved in regulating Hedgehog, G protein-coupled receptors, WNT, receptor tyrosine kinases, and transforming growth factor-beta (TGF-beta)/bone morphogenetic protein (BMP) [16]. Of these, the regulatory function of the primary cilium in Hedgehog signaling induction is best studied. In the absence of the Hedgehog ligand, Hedgehog signaling receptor (i.e., PTCH1) is enriched within the primary cilium, whereas Hedgehog signaling effector protein (i.e., Smoothened, SMO) is expelled out of the primary cilium [17] (Figure 1.3 D). At this time, transcription factor GLI is processed into repressor form for Hedgehog target genes at the ciliary base. The binding of the Hedgehog ligand with PTCH1 leads to a conformation change of PTCH1, which leads to PTCH1 trafficking out of primary cilium and the accumulation of SMO within the primary cilium [17] (Figure 1.3 E). The accumulation of SMO leads to subsequent ciliary trafficking and ciliary tip accumulation in a series of Hedgehog signaling components, including GLI1, GLI2, GLI3, KIF7, and SUFU [18–20]. Shuttling in and out of the primary cilium leads to the processing of GLI proteins into activators, which translocate into the nucleus after trafficking

out from the primary cilium and function as activators of Hedgehog signaling responsive genes [18] (Figure 1.3 E). EVC and EVC2/LIMBIN form a protein complex with SMO upon induction of Hedgehog signaling and this interaction has been demonstrated to be dependent on the primary cilium [11,12,21]. Based on these, it would be reasonable to expect that the overexpression of wild type *Evc* and *Evc2/Limbin* would lead to increased cellular response to Hedgehog ligand. However, forced expression of *Evc* and *Evc2/Limbin* together in NIH3T3 cells leads to decreased response to Hedgehog ligands [11]. Further studies are needed to delineate the mechanism of how forced expression of *Evc* and *Evc2/Limbin* together leads to decreased response to Hedgehog ligands.

Biochemical studies indicate that both EVC and EVC2/LIMBIN are *N*-terminal anchored membrane proteins that form a protein complex and are mutually required for ciliary localization [22]. While EVC and EVC2/LIMBIN share limited homology, the loss of function of one abolishes ciliary localization of the other, which can explain why clinical signs caused by mutations in *EVC* resemble those caused by mutations in *EVC2/LIMBIN* [11,22]. Within primary cilia, the EVC-EVC2/LIMBIN complex is located in a specific zone between the transition zone and Inversin zone [21] as shown in Figure 1.3 D and E. The specific zone in cilia is therefore named the EVC zone. Correct localization into the primary cilium and correct sub-ciliary localization within the primary cilium is critical for the function of EVC and EVC2/LIMBIN. Compared to EVC, the molecular biology of EVC2/LIMBIN is better studied. There are two major consensus sequences located at the *C*-terminus of EVC2/LIMBIN that are required for its precise localization: the FV domain and W sequence (Figure 1.3 C). The FV domain, containing two amino acids, phenylalanine, and valine, is located at the *C* terminal of EVC2/LIMBIN. It is responsible for locating EVC2/LIMBIN to the primary cilium and is conserved in almost all vertebrate, including fish. A disrupted FV domain leads to failed ciliary EVC2/LIMBIN localization and attenuated

response to the induction of Hedgehog signaling. The W sequence was initially identified in Weyers acrodental dysostosis, a phenotypically milder form of EVC. A functional FV domain but abolished W domain leads to a dominant negative form of EVC2/LIMBIN, which still locates into primary cilium but has aberrant sub-ciliary localization (i.e., generalized as opposed to restricted to the bottom of cilium) (Figure 1.3 G) [21,23]. Consequently, cellular response to Hedgehog signaling induction is attenuated to a lesser degree in cells with the abolished FV domain. Mechanistic studies indicate that protein EFCAB7 is responsible for tethering the EVC-EVC2/LIMBIN complex to the EVC zone within primary cilium via interaction with EVC2′s W domain [21]. These studies provide insight into the genetics of EVC, particularly regarding mutations identified in *EVC2/LIMBIN* (Figure 1.3 F). In the majority of EVC patients with *EVC2/LIMBIN* mutations, disease is inherited in a recessive manner and failed ciliary EVC2/LIMBIN localization can be attributed to non-functional FV caused by frame shift mutation [6]. Dissimilarly, Weyers acrodental dysostosis has a dominant inheritance pattern, a functional FV domain, a non-functional W domain, and a dominant negative form of the mutated EVC2/LIMBIN protein [4,6] (Figure 1.3 G). In contrast to studies on EVC2/LIMBIN, there are almost no biochemical studies on EVC despite many frame shift mutations identified in human patients [6]. This similarity suggests that, like EVC2/LIMBIN, the *C*-terminus of EVC may likewise be critical for the function of the EVC-EVC2/LIMBIN complex. Experimental evidence is warranted to prove the importance of the *C* terminal in EVC. In addition to the frame shift mutations, there are also missense mutations identified in *EVC* and *EVC2* in human affected by EVC [6]. All mutations identified in *EVC* and *EVC2/LIMBIN*, except those in the W domain of *EVC2/LIMBIN*, are recessive alleles. There is a recessive allele that is linked to less severe signs in affected individuals [24], prompting an idea that this recessive allele may be hypomorphic.

However, it is difficult to make a judgement if any *EVC* or *EVC2/LIMBIN* mutations are hypomorphic alleles through the severity of presented signs because 1) the genetic background in human population is complex; 2) the population size of individuals affected by EVC is very small. Mechanistic studies at molecular levels are needed to determine if mutant alleles are hypomorphic.

It should be noted that multiple lines of evidence suggest that EVC or EVC2/LIMBIN loss of function only partially compromises Hedgehog signaling [9,11,25]. This critical detail is supported by both *in vitro* molecular studies and *in vivo* phenotypic studies. For example, *Evc2/Limbin* mutant mouse embryonic fibroblast (MEF) or primary chondrocytes show two thirds of *Gli1* or *Ptch1* expression levels in comparison to control cells [9,11]. This is further supported by comparisons of mRNA levels of *Gli1* and *Ptch1* between multiple tissues between control and *Evc* or *Evc2/Limbin* mutant mice [10,25]. As pointed out by Zhang et al. [25], the partially compromised, instead of largely attenuated, Hedgehog signaling is the likely reason leading to normal lips, palate and neural tube development in humans affected by EVC and in *Evc or Evc2/Limbin* mutant mice [9,10,25], as summarized in Table 1.1. On the other hand, simply believing that the partially compromised Hedgehog signaling is the reason leading to the abnormal phenotypes in mutant mice or signs in humans may lead to an inaccurate understanding of the pathological mechanism. On the other hand, it is still not known if as ciliary components, EVC and EVC2/LIMBIN are involved in the ciliary regulation of other signaling pathways, and how affected non-Hedgehog signaling contributes to the pathological mechanism of EVC is remains elusive.

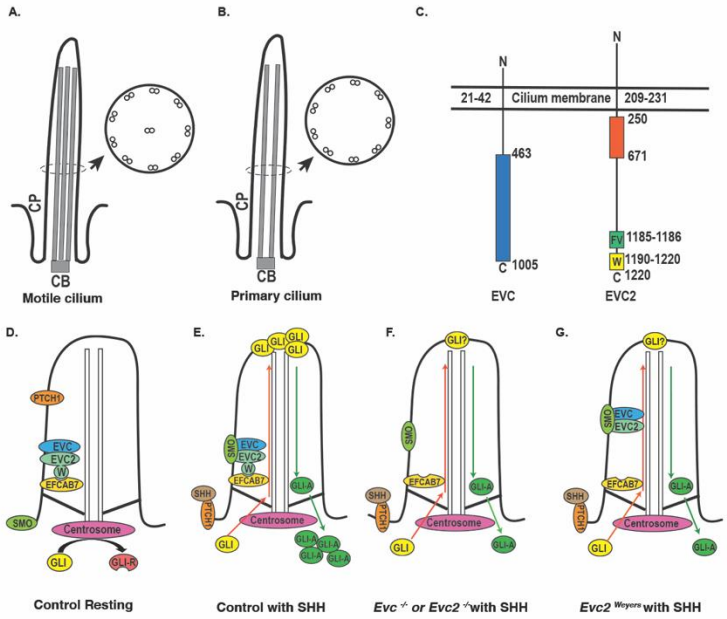

Figure 1.3: Primary cilium, EVC and EVC2/LIMBIN proteins, and the mechanism of EVC-EVC2/LIMBIN in regulating Hedgehog signaling within the primary cilium.
Diagrams of the motile cilium (**A**) and the primary cilium (**B**) are shown. CB, cilium base; CP, cilium pocket. (**C**). Structures of the EVC and the EVC2/LIMBIN are shown. The EVC and EVC2/LIMBIN are *N* terminal anchored proteins. Blue box in the EVC and orange box in the EVC2/LIMBIN indicate domains for interaction with each other. Green box indicates the domain for the ciliary localization of the EVC2/LIMBIN and the yellow box indicates the domain for localization of the EVC2/LIMBIN at the EVC zone. Numbers indicate the numbers of amino acids in each protein. (**D**) EVC-EVC2/LIMBIN complexes are localized at the bottom of cilia by tethering to EFCAB7 through the W domain in EVC2/LIMBIN. In the absence of Hedgehog ligand, PTCH1 resides within the primary cilium, and GLI proteins are processed to the repressor form (GLI-R) at the centrosome. (**E**) In the presence of Hedgehog ligand, binding of the ligands with PTCH1 leads to exclusion of PTCH1 out of the primary cilium, which allows SMO to enter the primary cilium. Within the primary cilium, SMO interacts with EVC-EVC2/LIMBIN at the bottom of the primary cilium, which allows GLI trafficking into the primary cilium and accumulation at the tip of the primary cilium. After entering the primary cilium, GLI are processed to the activator form (GLI-A). GLI activators exit the primary cilium and translocate into the nucleus to activate Hedgehog responsive genes. (**F**) EVC or EVC2/LIMBIN loss of function leads to absence of EVC-EVC2/LIMBIN complexes within the primary cilium. When Hedgehog signaling is activated, SMO still moves into the primary cilium, but without EVC-EVC2/LIMBIN complexes, SMO cannot lead to full activation of GLI. (**G**) In Weyers form of mutant cells, EVC-EVC2/LIMBIN complexes cannot be restricted at the bottom of primary cilium due to no interactions with EFCAB7 caused by loss of the W domain in EVC2/LIMBIN, thus EVC-EVC2/LIMBIN-SMO complex cannot lead to full activation of GLI.

Anatomical Locations	EVC	Weyers acrodental dysostosis	*Evc* mutant mice	*Evc2* mutant mice	Hedgehog signaling defects in mice
Limb	Short	Short (mild)	Short	Short	Short
Craniofacial	Normal	Normal	Normal	Normal	Cleft lips, cleft Palate
Neural tube	Normal	Normal	Normal	Normal	Open neural tube
Digit	Postaxial polydactyly	Postaxial polydactyly	Postaxial polydactyly	Postaxial polydactyly	Preaxial polydactyly (?)

Table 1.1: Clinical signs of EVC and phenotypes of Evc, Evc2/Limbin mutant mice, and mice with Hedgehog signaling defects.

1.2.3 Overview of Human Signs

Classic signs associated with EVC include polydactyly, congenital morbus cordis or heart disease, chondrodysplasia, and ectodermal dysplasia [1]. However, this tetrad is not present in all cases and there are reported degrees of severity [4]. Patients require an interdisciplinary treatment strategy due to symptom variability and prognosis which is ultimately dependent upon the extent of cardiac anomalies [26–28]. As a result, reports of adult patients with EVC are less common, though this may represent a bias towards pediatric diagnosis, based on apparent disease signs (e.g., polydactyly and chondrodysplasia) [28,29]. Individuals surviving beyond the tenuous neonatal period may live a normal lifespan and tend to have normal emotional and intellectual development, though there are reported instances of impairment [30].

Polydactyly, or the presence of extra digits, is the most conspicuous sign of EVC at birth [1,4]. Hands may have between 6–7 digits with extra fingers always present on the ulnar side (i.e., postaxially). Toes, though typically normal in number, may be irregularly aligned; both sets of appendages have dysplastic nails due to the associated ectodermal dysplasia. Patients exhibit progressive distal shortening of the fingers with underdevelopment of distal phalanges that may

include non-functional distal metacarpals. Additional digits can be surgically removed; however, this does not improve the “plump” appearance due to the underlying shortened bones.

Congenital heart disease is present in 50–60% of EVC patients and is the most significant cause of morbidity [4,26–28,31]. Septal defects range in severity with the most severe being cor biloculare or a two chambered heart. Venous anomalies concurrent with either atrial septal defects (ASD) or ventricular septal defects (VSD) may contribute to death via pulmonary hypotension. Accurate diagnosis and management of cardiac abnormalities are therefore necessary for improved disease prognosis.

Chondrodysplasias are disorders of bone growth that manifest as shortened stature. Though potentially non-apparent at birth, disproportionate dwarfism in patients with EVC is the result of long bones that are more shortened at their distal ends [1,32,33]. Patients have a normal length torso but dysplastic primary ossification centers in the paired bones of the arms and legs as well as the digits. Shortened ribs also result in a small chest with a keel-like breastbone that may not allow for proper lung expansion [31]. Musculoskeletal problems, such as genu valgum (knock knee) or talipes equinovarus (club foot), may restrict mobility and require orthopedic intervention (e.g., surgery or casting) to correct [4,33]. Interphalangeal ankylosis, most often seen in the distal metacarpals, may limit dexterity necessitating lifestyle adaptation and/or corrective surgery.

Ectodermal dysplasia affects ectodermal derived tissues, such as the hair, skin, nails, and teeth. Compared to other types of ectodermal dysplasia, hair and skin abnormalities are mild in EVC patients and occur in only about 1/3 of cases [4,34]. As previously mentioned, nails of both the hands and feet of patients with EVC are malformed with those of the hands, and especially supernumerary digits, being more affected. However, all patients with EVC have a dental phenotype that includes hypoplastic enamel, congenitally missing teeth (i.e., hypodontia),

abnormally shaped teeth (e.g., taurodontism or bulbous teeth), and premature eruption and exfoliation [28,35,36]. Abnormal craniofacial morphology may not be apparent at birth but includes a trend towards mandibular prognathism, maxillary deficiency, skeletal open bite, and prominent frontal bossing that gives patients a concave-shaped lateral profile. While not at an inherently increased risk of caries, the loss of oral function often requires extensive prosthodontic rehabilitation (e.g., dentures and implants) starting from a young age [37,38]. Depending on the severity of the craniofacial phenotype, patients with EVC may also benefit from treatment by speech–language pathologists.

In addition to the classic signs of EVC, less common findings include genital abnormalities and strabismus [2,33]. Abnormal urethral location (i.e., hypospadias) and undescended testicles (i.e., cryptorchidism) in males is rare, though the former is common in other forms of ectodermal dysplasia. Strabismus, a vision condition characterized by the misalignment of the eyes, is due to problems associated with the muscles that move the eyes (i.e., extraocular muscles). These muscles develop with influence from cranial neural crest cells, thereby suggesting an expanded role of EVC2/LIMBIN in the craniofacial region (see Section 5: Craniofacial Phenotype) [39]. Both genital and eye muscle abnormalities are non-life threatening and may be corrected with surgery.

1.2.4 Limb Phenotypes

Dwarfism or shortened stature is one of the most typical symptoms present in patients with EVC. Adult patients with EVC usually fall into the height range of 110cm to 155cm (−2 to −4.5 standard deviation scores) [40]. However, growth hormone deficiency is not consistently observed in these patients and growth hormone treatment in pediatric patients does not achieve consistent efficacy [40]. This suggests that dwarfism in patients with EVC is not likely due to deficiency or

abnormal growth hormone levels. Instead, dwarfism in EVC is mainly characterized by the disproportional distal shortening of arms and legs, whereas the trunk size of patients remains unchanged [1]. The pathological mechanism leading to the dwarfism in patients with EVC therefore lies in abnormal appendicular bone development.

Appendicular bone elongation during development occurs through endochondral ossification, a process in which chondrocyte proliferation and maturation in cartilage play vital roles in determining the final length of bones in the arms and legs [41,42]. Appendicular bone development is initiated from the condensation of mesenchymal cells and subsequent differentiation to chondrocytes [41]. Chondrocytes then undergo a series of proliferation and maturation steps, which allows for the formation of the primordial cartilage of appendicular bone. Chondrocyte proliferation and maturation are well orchestrated by a series of locally produced factors that ensure the correct length and shape of each skeletal element. Previous studies have demonstrated that many signaling pathways play important roles in regulating chondrocyte proliferation and maturation (Figure 1.4 A). For example, Fibroblast Growth Factor (FGF) signaling, mediated by FGF18 produced in the perichondrium, is involved in this regulatory network [43–45]. In the growth plate, FGF signaling inhibits chondrocyte proliferation through STAT1-mediated p21 expression and inhibits chondrocyte differentiation through MEK/PERK-mediated signaling [44,45]. Additionally, Indian Hedgehog and parathyroid hormone-related protein (PTHrP) signaling also play important roles in the regulation of chondrocyte proliferation, differentiation, and maturation. Indian Hedgehog is expressed by the pre-hypertrophic chondrocytes and stimulates PTHrP expression in chondrocytes at the distal end of the growth plate. PTHrP promotes chondrocyte proliferation and prevents them from directly progressing to pre-hypertrophic differentiation [46]. Once proliferating chondrocytes are far away enough from

the source of PTHrP (i.e., chondrocytes at the distal end of the growth plate), they differentiate into pre-hypertrophic chondrocytes, start expressing Indian Hedgehog, and then further mature into hypertrophic chondrocyte cells [41,47] (Figure 1.4 A).

Compromised cellular response to Hedgehog signaling seen in *Evc* or *Evc2/Limbin* loss of function mouse models has been originally speculated as the pathological mechanism leading to dwarfism in EVC [10,11,21]. Based on the current understanding, decreased Hedgehog/PTHrP signaling in the chondrocyte should lead to subsequently decreased proliferation and abnormal maturation of chondrocytes in cartilage of the appendicular skeleton. Indeed, studies using mouse models confirmed the decreased Hedgehog signaling and PTHrP expression in the growth plate of both *Evc* and *Evc2/Limbin* mutant mice. However, Zhang et al. [25] presented surprising evidence suggesting that compromised Hedgehog signaling is not the reason leading to dwarfism; chondrocyte specific deletion of *Evc2/Limbin* leads to very mild dwarfism at embryonic day E18.5 and leads to no dwarfism at postnatal day P21 [25].

Subsequent studies of abnormal signaling in the *Evc2/Limbin* mutant growth plate by Zhang et al. [25] implicate an elevated FGF secretion from the perichondrium as a critical contributor to the dwarf phenotype (Figure 1.4 B) [25]. Chondrocyte-specific (note: non-perichondrium) deletion of *Evc2/Limbin* results in a mild dwarf phenotype despite compromised Hedgehog signaling along with unaffected FGF signaling at both embryonic and postnatal stages. On the other hand, concurrent *Evc2/Limbin* deletion in both chondrocytes and perichondrium results in a severe dwarfism with compromised Hedgehog signaling and elevated FGF signaling at embryonic and postnatal stages [25] suggesting that increased FGF18 production in the mutant perichondrium is critical to inhibit chondrocyte proliferation and leads to dwarfism (Figure 1.4 B, red arrow). Though it is still unresolved how *Evc2/Limbin* loss of function within the

perichondrium leads to elevated FGF18 expression, the studies from Zhang et al. [25] highly suggest that elevated FGF signaling is a potential druggable target for dwarfism in patients with EVC [25]. Elevated FGF signaling in the growth plate is the pathological mechanism leading to another form of dwarfism (i.e., achondroplasia) and a soluble form of FGFR3 (sFGFR3) was recently evaluated in a clinical trial for treating this dwarfism [48]. The similar pathological mechanism for dwarfism in achondroplasia and EVC suggests that sFGFR3 may be a viable therapeutic for treating dwarfism in patients with EVC.

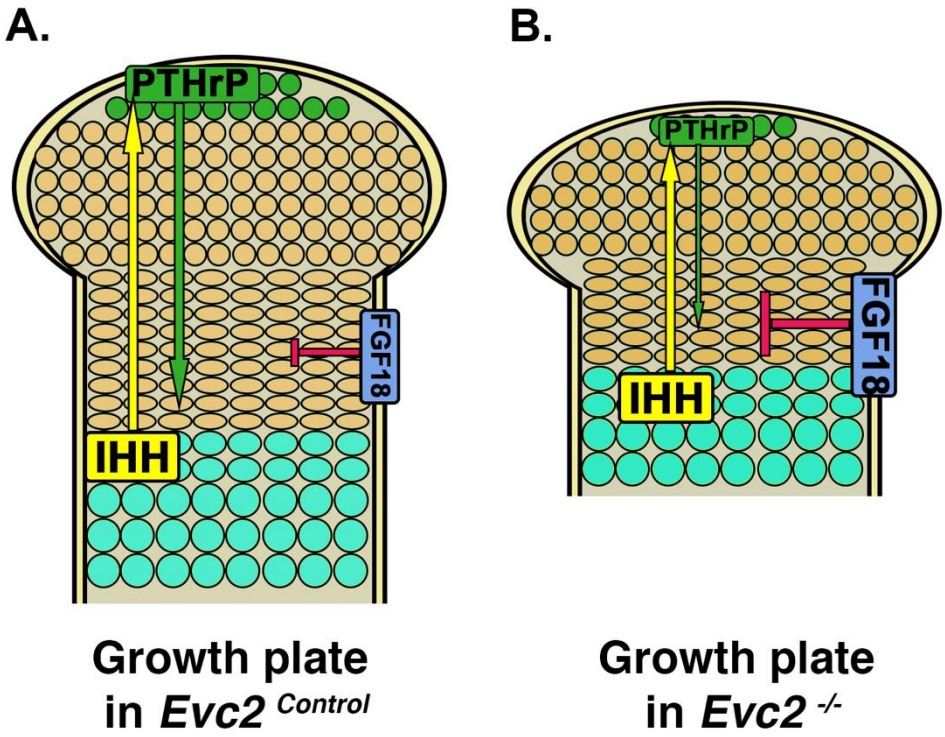

Figure 1.4: Elevated FGF signaling is critical for the pathogenesis of the dwarfism developed in EVC.
(A) In control growth plate, both Hedgehog signaling (yellow-green feedback loop) and FGF signaling (red) work on chondrocytes to ensure regulated proliferation and maturation. (B) In *Evc2/Limbin* mutant growth plate, moderately decreased Hedgehog signaling due to *Evc2/Limbin* loss of function within only chondrocytes moderately contributes to the pathogenesis of dwarfism, whereas elevated FGF signaling due to loss of *Evc2/Limbin* within perichondrium

critically contributes the pathogenesis of the dwarfism. Green, resting chondrocytes; gold sand, proliferating chondrocytes; aqua, hypertrophic chondrocytes, IHH, Indian Hedgehog ligand.

1.2.5 Craniofacial Phenotype

The concave facial profile seen in patients with EVC suggests morphologic differences in the midfacial and skull base regions. Mice highly express both *Evc* and *Evc2/Limbin* within these areas and *Evc* and *Evc2/Limbin* deficient mice show craniofacial phenotypes that recapitulate human signs [9–11,49–51]. *Evc* is expressed in the maxillary and mandibular processes from embryonic day E11.5 and detectable in the nasal septum at E15.5 [10]. *Evc2/Limbin* at E15.5 is similarly expressed within the mandible and maxilla as well as in the nasal, premaxilla, cranial sutures, and spheno-occipital synchondrosis [8,50]. Though no obvious craniofacial differences are discernible at embryonic time points, the structures listed above collectively represent cartilage-derived elements of the braincase and facial skeleton (i.e., neurocranium and viscerocranium), thereby providing insight into postnatal disease pathogenesis.

Many elements within the craniofacial region, specifically the neurocranium and viscerocranium, arise from neural crest cells (NCCs), a special population of cells that maintain their identity despite divergence from the ectoderm in early gastrulation [52]. Abnormal craniofacial morphology (i.e., midfacial depression) in both global and NCC-specific *Evc2/Limbin* deficient mice (referred to as *Evc2/Limbin*-KO and *Evc2/Limbin*-cKO, respectively) is a consequence of abnormalities within NCC-derived elements of the neurocranium and viscerocranium [50,51,53,54]. As with patients with EVC, midfacial depression or retrusion in mice becomes more pronounced with age and can be attributed to positional differences between the nasal bone, jaws, and cranial base [51,53]. Though this suggests a critical, NCC-specific role for *Evc2/Limbin* in determining postnatal craniofacial morphology, it does not indicate which structure (i.e., maxilla vs. skull base) is responsible for the resultant phenotype.

Cephalometric analysis is required to determine the etiology (i.e., maxilla vs. skull base deficiency) of midfacial retrusion in patients with EVC. Although such analyses are rare within the literature, findings from different *Evc2/Limbin*-cKO mouse models implicate the role of *Evc2/Limbin* in the anterior skull base (Figure 1.5 A and C). Though both Cre "drivers" (i.e., Wnt1-Cre and P0-Cre) used to create *Evc2/Limbin*-cKO mice are expressed throughout the jaws and facial skeleton, Wnt1-Cre-based recombination efficiency in the anterior skull base is much higher (100% vs. 50% for Wnt1-Cre and P0-Cre, respectively), results in worse midfacial deficiency, and causes greater skull base defects that in their *Evc2/Limbin*-P0-cKO counterparts [53]. This is significant as the skull base is a midline structure that connects the posterior of the head with the facial region and aberrant skull base morphology has been found to contribute to other syndromic facies.

A part of the neurocranium, the skull base is formed by endochondral ossification and consists of three segments connected by two growth plates or synchondroses, all mirrored and fused across the midline. Though skull base expression of *Evc* and *Evc2/Limbin* is lower than in the facial skeleton, all animal models of EVC (i.e., *Evc*-KO, *Evc2/Limbin*-KO, and *Evc2/Limbin*-cKO) have discernible differences in skull base size, shape, and bone quality [11,49,50,53]. Despite differences in facial gross morphologies, sizes and shapes of calvarial bones (nasal, frontal and parietal) are comparable between mutants and controls (Figure 1.5 B). Morphometric differences in *Evc2/Limbin*-cKO mice were most apparent in the anterior vs. posterior skull base (i.e., presphenoid and basisphenoid vs. basioccipital) where they, as with *Evc*-KO mice, also showed the premature fusion of the intrasphenoidal synchondrosis (ISS) between these two parts [49,53] (Figure 1.5 C). As expected, no differences were seen in the non-NCC-derived basioccipital at the posterior skull base (Figure 1.5 C) and spheno-occipital synchondrosis (SOS)

remains open in the *Evc2/Limbin*-cKO. The collective evidence suggests that *Evc2/Limbin* genes affect postnatal craniofacial morphology by maintaining the ISS and allowing for anterior skull base elongation. This critically explains why patients with EVC present progressively worsening midfacial depression (Figure 1.5).

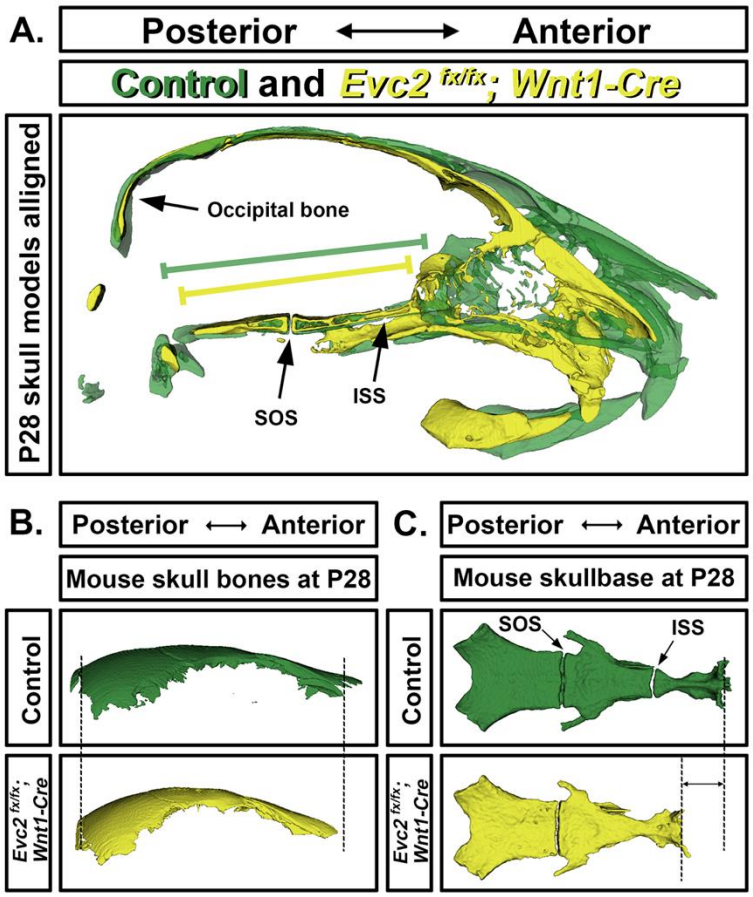

Figure 1.5: A shortened skull base leads to mid-facial defects in Evc2/Limbin mutant mice. (**A**) Surface models of the mid-line regions were generated based on the micro-CT scans of controls (green) and *Evc2/Limbin* mutants (yellow). Two models were then superimposed at the occipital bones of the skull. Green and yellow lines are spanning the entire regions of the skull bases in control and mutant, respectively; black arrows indicate the intersphenoidal synchondrosis (ISS) and the spheno-occipital synchondrosis (SOS) in skull base. (**B**) Models were generated from the skull region containing nasal, frontal and parietal bones from micro-CT scans of control and mutant. No apparent defects were observed in *Evc2/Limbin* mutants in comparing to controls. (**C**) Models were generated from the skull base from micro-CT scans of

controls and mutants. Apparent shortened anterior parts of skull bases from *Evc2/Limbin* mutants are observed in comparison to controls, whereas the posterior part of the mutant skull bases remains the same length with the controls. Black arrows indicate the ISS and the SOS.

1.2.6 Tooth Phenotype

Embryonic tooth development requires a series of morphological differentiations and the interaction between the dental epithelium and mesenchyme. Ameloblasts and odontoblasts arise from the dental epithelium and mesenchyme, respectively, and secrete matrix proteins necessary for the formation of enamel and dentin. Despite this crosstalk, ameloblast and odontoblasts have different developmental origins and, respectively, arise from ectodermal or neural crest cells [55]. The recapitulation of human dental abnormalities in animal models has revealed expanded and cell-specific roles of *Evc* or *Evc2/Limbin* in disease pathogenesis.

Global disruption of *Evc* or *Evc2/Limbin* and NCC-specific disruption of *Evc2/Limbin* in mice all result in a range of dental phenotypes of the likes seen in patients with EVC. This includes enamel hypoplasia, hypodontia (i.e., congenitally missing teeth), and progressively abnormal tooth morphology (e.g., small, conically shaped, fused, and/or short rooted) [9,10,51,56]. Phenotypic similarity between global and NCC-specific *Evc2/Limbin* deficient mice importantly suggests that *Evc2/Limbin* expression in the NCC-derived dental mesenchyme determines tooth morphology and enamel development. This means that tooth and enamel phenotypes seen in patients with EVC are secondary results, driven by misexpression in NCC-derived cells.

1.2.7 Tracheal Cartilage Phenotypes

Unlike other symptoms of EVC that become more apparent throughout childhood, airway obstruction or collapse is an immediate and life-threatening condition that may have been overlooked and underreported for a long time. Neonatal death associated with collapsed airway

has been documented in infant patients with EVC. Biopsies indicate hypomorphic tracheal cartilage that is unable to support the tracheal epithelia during the initiation of breathing [1]. The insufficient cartilaginous support of the airway at laryngeal, tracheal, or bronchi level condition is termed laryngotracheobronchomalacia and may also lead to stridor or noisy breathing in infant patients with EVC [1]. Similarly, neonatal death was reported in *Evc2/Limbin* mutant mice [9]. Whether the neonatal death is due to defective cartilage structure will be worth investigating.

1.2.8 EVC-like disorders in Non-Human Species

Examples of dwarfism or small stature resulting from a medial or genetic condition are not uncommon throughout the animal kingdom. However, while news headlines are dominated by the discovery of insular dwarf species and deliberate selection has led to the development of numerous toy and true "dwarf" animal varieties, chondrodysplastic cases attributable to mutations in animal orthologs (specifically *EVC2/LIMBIN*) are restricted to two breeds of cattle. However, recent comparative studies have the potential to spark interest in the etiology of EVC-like disorders and reveal the evolutionary significance of EVC2/LIMBIN in other species.

The Japanese brown cattle is a horned cattle breed esteemed for its use in beef production, known as wagyu. Starting in the late 1980s, calves from a specific region of Japan were born with a type of dwarfism (i.e., ateliosis) characterized by disproportionately short limbs and joint abnormalities [57]. Termed bovine chondrodysplastic dwarfism (BCD), this unusual phenotype was inherited in an autosomal recessive fashion and was later found to be caused by either deletion or frameshift mutations in a gene (i.e., *LIMBIN*) located on chromosome 6 [57,58]. *LIMBIN* was subsequently identified as an ortholog of human *EVC2* despite the lessened severity of symptoms in bovine vs. human patients [8]. Identification and targeted manipulation of the murine ortholog

laid the groundwork for the generation and phenotypic characterization of non-human models of EVC (see previous sections) that have been invaluable in our mechanistic understanding of disease development.

A similar form of disproportionate dwarfism in Tyrol grey cattle was reported in the early 21st century. The Tyrol grey is a horned, dual purpose breed of Austrian and Italian origin considered endangered due to its small population (<4000 individuals vs. >20,000 for Japanese brown) [59,60]. Affected calves could be traced back to a single ancestor and displayed the characteristic small stature and short limbs seen in both Japanese BCD and human EVC examples [59]. In addition to growth plate abnormalities in long bones indicative of dysplastic chondrocyte function, some Tyrol BCD specimens also displayed acetabular joint laxity, urogenital abnormalities, and cardiac defects reminiscent of human patients with EVC [59,61]. However, orofacial, ectodermal, and digit findings in these cattle were unremarkable and appendages were shortened in a proximal vs. distal manner as indicated by the shortened femur and humerus. Though genetic analyses identified an *EVC2/LIMBIN* mutation (i.e., deletion) at a different location from their Japanese counterparts, these cattle provided an animal model of an EVC-like disorder and expanded insight into the role of EVC2/LIMBIN in skeletogenesis.

Penguins are flightless birds that have undergone numerous morphological adaptations suited to an aquatic lifestyle. These include modification of the upper appendages into robust, flipper-like wings and pronounced shortening of femoral and lower extremity length, characteristics that are superficially like those seen in patients with EVC (see previous sections). Genetic analysis of two penguin species (i.e., *Pygoscelis adeliae* and *P. forsteri*) surprisingly revealed five penguin-specific amino acid changes in EVC2/LIMBIN, the highest amongst all analyzed limb-related genes [62]. An additional amino acid change was seen in the penguin EVC

ortholog. These results suggest important evolutionary roles of *EVC* and *EVC2/LIMBIN* orthologs due to their conserved effects on vertebrate (e.g., mammalian and avian) limb development.

1.2.9 Conclusions

It has been 80 years since the first report of EVC, 13 years since the report of *Evc* mutant mice, and 5 or 8 years since two independent reports of two *Evc2/Limbin* mutant mouse models. Within this short time, genetic mouse models have allowed great insight regarding the pathogenesis of EVC, expanded both breadth and depth of knowledge, and provided potential insight into therapeutic solutions for different aspects of EVC. Beyond patient care, *Evc2/Limbin* mutant mice have become a precious genetic tool for propelling our current understanding in molecular, cellular, and development biology.

1.2.10 References

1. Ellis, R.W.B.; Van Creveld, S. A syndrome characterized by ectodermal dysplasia, polydactyly, chondro-dysplasia and congenital morbus cordis: Report of three cases. *Arch. Dis. Child.* 1940, *15*, 65–84, doi:10.1136/adc.15.82.65.
2. McKusick, V.A. Dwarfism in the Amish I. The Ellis-van Creveld Syndrome. *Bull. Johns Hopkins Hosp.* 1964, *115*, 306–336.
3. Ruiz-Perez, V.L.; Ide, S.E.; Strom, T.M.; Lorenz, B.; Wilson, D.; Woods, K.; King, L.; Francomano, C.; Freisinger, P.; Spranger, S.; et al. Mutations in a new gene in Ellis-van Creveld syndrome and Weyers acrodental dysostosis. *Nat. Genet.* 2000, *24*, 283–286, doi:10.1038/73508.
4. Baujat, G.; Merrer, M.L. Ellis-Van Creveld syndrome. *Orphanet J. Rare Dis.* 2007, *2*, doi:10.1186/1750-1172-2-27.
5. Ruiz-Perez, V.L.; Goodship, J.A. Ellis-van Creveld syndrome and Weyers acrodental dysostosis are caused by cilia-mediated diminished response to Hedgehog ligands. *Am. J. Med. Genet. Part C: Semin. Med. Genet.* 2009, *151*, 341–351, doi:10.1002/ajmg.c.30226.
6. Tompson, S.W.; Ruiz-Perez, V.L.; Blair, H.J.; Barton, S.; Navarro, V.; Robson, J.L.; Wright, M.J.; Goodship, J.A. Sequencing EVC and EVC2 identifies mutations in two-thirds of Ellis-van Creveld syndrome patients. *Hum. Genet.* 2007, *120*, 663–670, doi:10.1007/s00439-006-0237-7.
7. D'Asdia, M.C.; Torrente, I.; Consoli, F.; Ferese, R.; Magliozzi, M.; Bernardini, L.; Guida, V.; Digilio, M.C.; Marino, B.; Dallapiccola, B.; et al. Novel and recurrent EVC and EVC2 mutations in Ellis-van Creveld syndrome and Weyers acrofacial dyostosis. *Eur. J. Med. Genet.* 2013, *56*, 80–87, doi:10.1016/j.ejmg.2012.11.005.
8. Takeda, H.; Takami, M.; Oguni, T.; Tsuji, T.; Yoneda, K.; Sato, H.; Ihara, N.; Itoh, T.; Kata, S.R.; Mishina, Y.; et al. Positional cloning of the gene LIMBIN responsible for bovine chondrodysplastic dwarfism. *Proc. Natl. Acad. Sci. USA*2002, *99*, 10549–10554, doi:10.1073/pnas.152337899.
9. Zhang, H.; Takeda, H.; Tsuji, T.; Kamiya, N.; Rajderkar, S.; Louie, K.A.; Collier, C.; Scott, G.; Ray, M.; Mochida, Y.; et al. Generation of Evc2/Limbin global and conditional KO mice and its roles during mineralized tissue formation. *Genesis* 2015, *53*, 612–626, doi:10.1002/dvg.22879.
10. Ruiz-Perez, V.L.; Blair, H.J.; Rodrigues-Andres, M.E.; Blanco, M.J.; Wilson, A.; Liu, Y.N.; Miles, C.; Peters, H.; Goodship, J.A. Evc is a positive mediator of Ihh-regulated bone growth that localises at the base of chondrocyte cilia. *Development* 2007, *134*, 2903–2912, doi:10.1242/dev.007542.
11. Caparrós-Martín, J.A.; Valencia, M.; Reytor, E.; Pacheco, M.; Fernandez, M.; Perez-Aytes, A.; Gean, E.; Lapunzina, P.; Peters, H.; Goodship, J.A.; et al. The ciliary EVC/EVC2 complex interacts with smo and controls hedgehog pathway activity in chondrocytes by regulating Sufu/Gli3 dissociation and Gli3 trafficking in primary cilia. *Hum. Mol. Genet.* 2013, *22*, 124–139, doi:10.1093/hmg/dds409.

12. Yang, C.; Chen, W.; Chen, Y.; Jiang, J. Smoothened transduces Hedgehog signal by forming a complex with Evc/Evc2. *Cell Res.* 2012, *22*, 1593–1604, doi:10.1038/cr.2012.134.
13. Eggenschwiler, J.T.; Anderson, K.V. Cilia and developmental signaling. *Annu. Rev. Cell Dev. Biol.* 2007, *23*, 345–373, doi:10.1146/annurev.cellbio.23.090506.123249.
14. Afzelius, B.A. Cilia-related diseases. *J. Pathol.* 2004, *204*, 470–477, doi:10.1002/path.1652.
15. Camner, P.; Mossberg, B.; Afzelius, B.A. Evidence of congenitally nonfunctioning cilia in the tracheobronchial tract in two subjects. *Am. Rev. Respir. Dis.* 1975, *112*, 807–809, doi:10.1164/arrd.1975.112.6.807.
16. Anvarian, Z.; Mykytyn, K.; Mukhopadhyay, S.; Pedersen, L.B.; Christensen, S.T. Cellular signalling by primary cilia in development, organ function and disease. *Nat. Rev. Nephrol.* 2019, *15*, 199–219, doi:10.1038/s41581-019-0116-9.
17. Corbit, K.C.; Aanstad, P.; Singla, V.; Norman, A.R.; Stainier, D.Y.; Reiter, J.F. Vertebrate Smoothened functions at the primary cilium. *Nature* 2005, *437*, 1018–1021, doi:10.1038/nature04117.
18. Kim, J.; Kato, M.; Beachy, P.A. Gli2 trafficking links Hedgehog-dependent activation of Smoothened in the primary cilium to transcriptional activation in the nucleus. *Proc. Natl. Acad. Sci. USA* 2009, *106*, 21666–21671, doi:10.1073/pnas.0912180106.
19. Humke, E.W.; Dorn, K.V.; Milenkovic, L.; Scott, M.P.; Rohatgi, R. The output of Hedgehog signaling is controlled by the dynamic association between Suppressor of Fused and the Gli proteins. *Genes Dev.* 2010, *24*, 670–682, doi:10.1101/gad.1902910.
20. Tukachinsky, H.; Lopez, L.V.; Salic, A. A mechanism for vertebrate Hedgehog signaling: recruitment to cilia and dissociation of SuFu-Gli protein complexes. *J Cell Biol.* 2010, *191*, 415–428, doi:10.1083/jcb.201004108.
21. Dorn, K.V.; Hughes, C.E.; Rohatgi, R. A Smoothened-Evc2 complex transduces the Hedgehog signal at primary cilia. *Dev. Cell* 2012, *23*, 823–835, doi:10.1016/j.devcel.2012.07.004.
22. Blair, H.J.; Tompson, S.; Liu, Y.N.; Campbell, J.; MacArthur, K.; Ponting, C.P.; Ruiz-Perez, V.L.; Goodship, J.A. Evc2 is a positive modulator of Hedgehog signalling that interacts with Evc at the cilia membrane and is also found in the nucleus. *BMC Biol.* 2011, *9*, 14, doi:10.1186/1741-7007-9-14.
23. Valencia, M.; Lapunzina, P.; Lim, D.; Zannolli, R.; Bartholdi, D.; Wollnik, B.; Al-Ajlouni, O.; Eid, S.S.; Cox, H.; Buoni, S.; et al. Widening the mutation spectrum of EVC and EVC2: ectopic expression of Weyer variants in NIH 3T3 fibroblasts disrupts Hedgehog signaling. *Hum. Mutat.* 2009, *30*, 1667–1675, doi:10.1002/humu.21117.
24. Ulucan, H.; Guel, D.; Sapp, J.C.; Cockerham, J.; Johnston, J.J.; Biesecker, L.G. Extending the spectrum of Ellis van Creveld syndrome: a large family with a mild mutation in the EVC gene. *BMC Med. Genet.* 2008, *9*, doi:Artn 9210.1186/1471-2350-9-92.
25. Zhang, H.; Kamiya, N.; Tsuji, T.; Takeda, H.; Scott, G.; Rajderkar, S.; Ray, M.K.; Mochida, Y.; Allen, B.; Lefebvre, V.; et al. Elevated Fibroblast Growth Factor Signaling Is Critical for the Pathogenesis of the Dwarfism in Evc2/Limbin Mutant Mice. *PLoS Genet.* 2016, *12*, e1006510, doi:10.1371/journal.pgen.1006510.
26. Alvarez-Borja, A. Ellis-van Creveld Syndrome: Report of two cases. *Pediatrics* 1960, *26*, 301–309, doi:10.1016/S0099-6963(30)90009-9.

27. Husson, G.S.; Parkman, P. Chondroectodermal dysplasia (Ellis-Van Creveld syndrome) with a complex cardiac malformation. *Pediatrics* 1961, *28*, 285–292.
28. Lynch, J.I. Congenital Heart Disease and Chondroectodermal Dysplasia. *Am. J. Dis. Child.* 1968, *115*, 80–80, doi:10.1001/archpedi.1968.02100010082016.
29. Goor, D.; Rotem, Y.; Friedman, A.; Neufeld, H.N. ELLIS-VAN CREVELD SYNDROME IN IDENTICAL TWINS * In 1933 McIntosh (Holt and McIntosh , 1933) described abnormal findings in a girl who had. *Br. Heart J.* 1965, *27*, 797–804.
30. Metrakos, J.D.; Fraser, F.C. Evidence for a hereditary factor in chondroectodermal dysplasia (Ellis-van Creveld syndrome). *Am. J. Hum. Genet.* 1954, *6*, 260–269.
31. Smith, H.L.; Hand, A.M. Chondroectodermal Dysplasia (Ellis-van Creveld Syndrome): Report of Two Cases. *Pediatrics* 1958, *21*, 298–307.
32. Weiss, H.; Crosett, A.D. Chondroectodermal dysplasia: report of a case and review of the literature. *J. Pediatrics* 1955, *46*, 268–275.
33. Mitchell, F.N.; Waddell, W.W. Ellis-van Creveld syndrome: Report of two cases in siblings. *Acta Paediatr.* 1958, *47*, 142–151, doi:10.1007/s12519-011-0256-x.
34. Hill, R.D. Two cases of Ellis van Creveld syndrome in a small island population. *J. Med. Genet.* 1977, *14*, 33–36, doi:10.1136/jmg.14.1.33.
35. Da Silva, E.O.; Janovitz, D.; Cavalcanti De Albuquerque, S. Ellis-van Creveld syndrome: Report of 15 cases in an inbred kindred. *J. Med. Genet.* 1980, *17*, 349–356, doi:10.1136/jmg.17.5.349.
36. Cahuana, A.; Palma, C.; Gonzáles, W.; Geán, E. Oral manifestations in Ellis-van Creveld syndrome: Report of five cases. *Pediatric Dent.* 2004, *26*, 277–282.
37. Hanemann, J.A.C.; de Carvalho, B.C.F.; Franco, E.C. Oral manifestations in Ellis-van Creveld syndrome: report of a case and review of the literature. *J. Oral Maxillofac. Surg.* 2010, *68*, 456–460, doi:10.1016/j.joms.2009.07.026.
38. Naqash, T.A.; Alshahrani, I.; Simasetha, S. Ellis-van creveld syndrome: A rare clinical report of oral rehabilitation by interdisciplinary approach. *Case Rep. Dent.* 2018, *2018*, doi:10.1155/2018/8631602.
39. Bohnsack, B.L.; Gallina, D.; Thompson, H.; Kasprick, D.S.; Lucarelli, M.J.; Dootz, G.; Nelson, C.; McGonnell, I.M.; Kahana, A. Development of extraocular muscles requires early signals from periocular neural crest and the developing eye. *Arch. Ophthalmol.* 2011, *129*, 1030–1041, doi:10.1001/archophthalmol.2011.75.
40. Versteegh, F.G.; Buma, S.A.; Costin, G.; de Jong, W.C.; Hennekam, R.C.; Ev, C.W.P. Growth hormone analysis and treatment in Ellis-van Creveld syndrome. *Am. J. Med. Genet. A* 2007, *143A*, 2113-2121, doi:10.1002/ajmg.a.31891.
41. Kronenberg, H.M. Developmental regulation of the growth plate. *Nature* 2003, *423*, 332–336, doi:10.1038/nature01657nature01657.
42. Long, F.; Ornitz, D.M. Development of the endochondral skeleton. *Cold Spring Harb. Perspect. Biol.* 2013, *5*, a008334, doi:10.1101/cshperspect.a008334.
43. Su, W.C.; Kitagawa, M.; Xue, N.; Xie, B.; Garofalo, S.; Cho, J.; Deng, C.; Horton, W.A.; Fu, X.Y. Activation of Stat1 by mutant fibroblast growth-factor receptor in thanatophoric dysplasia type II dwarfism. *Nature* 1997, *386*, 288–292, doi:10.1038/386288a0.
44. Sahni, M.; Ambrosetti, D.C.; Mansukhani, A.; Gertner, R.; Levy, D.; Basilico, C. FGF signaling inhibits chondrocyte proliferation and regulates bone development through the STAT-1 pathway. *Genes Dev.* 1999, *13*, 1361–1366, doi:10.1101/gad.13.11.1361.

45. Murakami, S.; Balmes, G.; McKinney, S.; Zhang, Z.; Givol, D.; de Crombrugghe, B. Constitutive activation of MEK1 in chondrocytes causes Stat1-independent achondroplasia-like dwarfism and rescues the Fgfr3-deficient mouse phenotype. *Genes Dev.* 2004, *18*, 290–305, doi:10.1101/gad.1179104.
46. St-Jacques, B.; Hammerschmidt, M.; McMahon, A.P. Indian hedgehog signaling regulates proliferation and differentiation of chondrocytes and is essential for bone formation. *Genes Dev.* 1999, *13*, 2072–2086, doi:10.1101/gad.13.16.2072.
47. Vortkamp, A.; Lee, K.; Lanske, B.; Segre, G.V.; Kronenberg, H.M.; Tabin, C.J. Regulation of rate of cartilage differentiation by Indian hedgehog and PTH-related protein. *Science* 1996, *273*, 613–622, doi:10.1126/science.273.5275.613.
48. Garcia, S.; Dirat, B.; Tognacci, T.; Rochet, N.; Mouska, X.; Bonnafous, S.; Patouraux, S.; Tran, A.; Gual, P.; Le Marchand-Brustel, Y.; et al. Postnatal soluble FGFR3 therapy rescues achondroplasia symptoms and restores bone growth in mice. *Sci. Transl. Med.* 2013, *5*, 203ra124, doi:10.1126/scitranslmed.3006247.
49. Pacheco, M.; Valencia, M.; Caparrós-Martín, J.A.; Mulero, F.; Goodship, J.A.; Ruiz-Perez, V.L. Evc works in chondrocytes and osteoblasts to regulate multiple aspects of growth plate development in the appendicular skeleton and cranial base. *Bone* 2012, *50*, 28–41, doi:10.1016/j.bone.2011.08.025.
50. Badri, M.K.; Zhang, H.; Ohyama, Y.; Venkitapathi, S.; Alamoudi, A.; Kamiya, N.; Takeda, H.; Ray, M.; Scott, G.; Tsuji, T.; et al. Expression of Evc2 in craniofacial tissues and craniofacial bone defects in Evc2 knockout mouse. *Arch. Oral Biol.* 2016, *68*, 142–152, doi:10.1016/j.archoralbio.2016.05.002.
51. Badri, M.K.; Zhang, H.; Ohyama, Y.; Venkitapathi, S.; Kamiya, N.; Takeda, H.; Ray, M.; Scott, G.; Tsuji, T.; Kunieda, T.; et al. Ellis Van Creveld2 is Required for Postnatal Craniofacial Bone Development. *Anat. Rec.* 2016, *299*, 1110–1120, doi:10.1002/ar.23353.
52. Mishina, Y.; Snider, T.N. Neural crest cell signaling pathways critical to cranial bone development and pathology. *Exp. Cell Res.* 2015, *325*, 138–147, doi:10.1016/j.yexcr.2014.01.019.
53. Kulkarni, A.K.; Louie, K.a.W.; Yatabe, M.; De Oliveira Ruellas, A.C.; Mochida, Y.; Cevidanes, L.H.S.; Mishina, Y.; Zhang, H. A Ciliary Protein EVC2/LIMBIN Plays a Critical Role in the Skull Base for Mid-Facial Development. *Front. Physiol.* 2018, *9*, 1–13, doi:10.3389/fphys.2018.01484.
54. Kwon, E.K.; Louie, K.a.W.; Kulkarni, A.; Yatabe, M.; Carlos, A.; Ruellas, D.E.O.; Snider, T.N.; Mochida, Y.; Cevidanes, L.H.S.; Mishina, Y. The Role of Ellis-Van Creveld 2 (EVC2) in Mice During Cranial Bone Development. *Anat. Rec.* 2018, *301*, 46–55, doi:10.1002/ar.23692.
55. Thesleff, I.; Hurmerinta, K. Tissue Interactions in Tooth Development. *Differentiation* 1981, *18*, 75–88, doi:10.1111/j.1432-0436.1981.tb01107.x.
56. Zhang, H.; Takeda, H.; Tsuji, T.; Kamiya, N.; Kunieda, T.; Mochida, Y.; Mishina, Y. Loss of Function of Evc2 in Dental Mesenchyme Leads to Hypomorphic Enamel. *J. Dent. Res.* 2017, *96*, 421–429, doi:10.1177/0022034516683674.
57. Morimoto, Y.; Ishibashi, T.; Ashizawa, H.; Shibata, T. Chondrodysplastic Dwarfism in Japanese Brown Cattle. *J. Jpn. Vet. Med Assoc.* 1989, *42*, 173–177, doi:10.12935/jvma1951.42.173.

58. Yoneda, K.; Moritomo, Y.; Takami, M.; Hirata, S.; Kikukawa, Y.; Kunieda, T. Localization of a locus responsible for the bovine chondrodysplastic dwarfism (bcd) on chromosome 6. *Mamm. Genome* 1999, *10*, 597–600, doi:10.1007/s003359901052.
59. Murgiano, L.; Jagannathan, V.; Benazzi, C.; Bolcato, M.; Brunetti, B.; Muscatello, L.V.; Dittmer, K.; Piffer, C.; Gentile, A.; Drögemüller, C. Deletion in the EVC2 gene causes chondrodysplastic dwarfism in Tyrolean grey cattle. *PLoS ONE* 2014, *9*, doi:10.1371/journal.pone.0094861.
60. Gotoh, T.; Nishimura, T.; Kuchida, K.; Mannen, H. The Japanese Wagyu beef industry: Current situation and future prospects - A review. *Asian-Australas. J. Anim. Sci.* 2018, *31*, 933–950, doi:10.5713/ajas.18.0333.
61. Muscatello, L.V.; Benazzi, C.; Dittmer, K.E.; Thompson, K.G.; Murgiano, L.; Drögemüller, C.; Avallone, G.; Gentile, A.; Edwards, J.F.; Piffer, C.; et al. Ellis–van Creveld Syndrome in Grey Alpine Cattle: Morphologic, Immunophenotypic, and Molecular Characterization. *Vet. Pathol.* 2015, *52*, 957–966, doi:10.1177/0300985815588610.
62. Li, C.; Zhang, Y.; Li, J.; Kong, L.; Hu, H.; Pan, H.; Xu, L.; Deng, Y.; Li, Q.; Jin, L.; et al. Two Antarctic penguin genomes reveal insights into their evolutionary history and molecular changes related to the Antarctic environment. *GigaScience* 2014, *3*, 1–15, doi:10.1186/2047-217X-3-27.

1.3 Hypotheses and Aims

There is a clinical need to restore craniofacial tissues affected by disorders of traumatic and/or congenital etiology. Effective therapeutic approaches within this specialized area require both anatomic regeneration and the effective restoration of function. Regardless of etiology, adaptation represents a crucial corrective mechanism necessary for functional restoration and, ultimately, the maintenance of life. The work in this dissertation attempts to identify mechanisms underlying the regeneration while simultaneously elucidating oral function and adaptation using mastication as a readout of craniofacial tissue interactions.

Global Hypothesis: Perturbation of gene expression during adult craniofacial tissue regeneration has functional outcomes that extend beyond the dysmorphic structures.

Hypothesis 1: Genes differentially expressed at early time points play unique roles during myocyte reprogramming and adult muscle regeneration.

Aim 1: Utilize RNA-seq to identify candidate genes and pathways that affect myocyte reprogramming and craniofacial muscle regeneration in a model with robust regenerative capacity (i.e., zebrafish). Phenotypic screening following gene knockdown will then be used to assess the necessity of identified targets at different points (e.g., early vs. late) during the muscle regeneration process. Gene paralog subfunctionalization and key differences between adult tissue regeneration and embryogenesis will then be investigated using a combined knockdown approach of related genes (e.g., twist1a, twist1b, twist2, and twist3).

Hypothesis 2: Fundamental changes in dental and craniofacial morphology decrease chewing efficiency.

Aim 2: Characterize craniofacial and dental morphology in an animal model of a human genetic disorder (i.e., Ellis-van Creveld syndrome). After establishing fundamental changes in craniofacial architecture (e.g., skull base, jaws, and teeth), chewing motions and efficiency will then be used as a readout of complex tissue interactions. Changes in functional parameters (e.g., bite force, chewing rate, and efficiency) will then be used to identify compensatory adaptations occurring within this clinically relevant tool.

1.4 Summary and Organization

In Chapter 2, a high throughput approach is used to identify genes and pathways that regulate the muscle-to-mesenchymal transition (MMT) observed in myocytes following a volumetric muscle loss injury. Chapter 3 address the unique role of a specific gene paralog (i.e., *twist3*) during regeneration but not embryonic muscle development. Chapter 4 marks the transition to Aim 2 and presents a detailed craniofacial characterization of an animal model of a human genetic disorder (i.e., EVC) at different stages of maturation. Chapter 5 then examines dental morphology in the same animal model and evaluates the effect of changes on chewing performance. Chapter 6 finally summarizes the key findings of this body of work while discussing future directions.

Chapter 2: Regulation of Craniofacial Muscle Regeneration[2]

2.1 Background

The goal of regenerative medicine is to replace lost tissue with fully functional regenerated tissue following trauma or disease. Given their highly specialized structure and function, skeletal muscles are particularly prone to tissue loss following disease or injury, with devastating effects on function and quality of life [1,2] Although humans do not have extensive muscle regeneration capabilities that persist beyond the embryonic stage, tissue regeneration is observed in other vertebrate lineages and has been well studied in both amphibian and piscine models [3–5].

Regeneration of lost muscle requires the generation of an adequate number of myocytes to match the lost tissue and provide replacement function. Accumulation of such a regenerative cell mass can occur via proliferative expansion of resident tissue stem cells (i.e., satellite cells; [6,7]), recruitment of cells from outside the damaged tissue area, or dedifferentiation of residual cells into progenitor cells capable of robust proliferation and redifferentiation [8,9]. Blastema formation is observed in both urodele amphibian leg regeneration models and fish fin regeneration models [10,11] and appears to utilize all three regenerative pathways [5]. On the other hand, regeneration of zebrafish retina, bone, cartilage, heart, liver, and extraocular muscles (EOMs) primarily utilizes dedifferentiation of residual cells [8,9,12–15]. The ability to reprogram "post-mitotic" cells into

[2] Published as Louie KW, Saera-Vila A, Kish PE, Colacino JA, Kahana A. 2017. Temporally distinct transcriptional regulation of myocyte dedifferentiation and Myofiber growth during muscle regeneration. *BMC Genomics* 18(1):854.

dedifferentiated proliferating progenitor cells represents a particularly potent approach to adult tissue regeneration that circumvents the limitations of stem cell-based techniques [16].

Zebrafish EOMs regenerate very rapidly following tissue loss, with myocyte reprogramming leading to myoblast proliferation by 20 hours post injury (hpi), anatomic muscle regeneration within 5-7 days post injury (dpi), and functional recovery within 8-10 dpi [9]. In order to understand the biological events that lead to reprogramming a highly-specialized cell such as a "post-mitotic" multinucleated syncytial myocyte, we focused on the transcriptional events that occur at time points (9 and 18 hpi) ending just prior to cell cycle reentry by dedifferentiated myoblasts seen at 20 hpi. Aided by the relatively homogenous population of dedifferentiating cells and utilizing these pre-proliferative time points, we performed a comprehensive transcriptome analysis. We were particularly interested in the broad, network-like interactions expected to occur within the dynamic biological landscape of reprogramming cells [9,17,18].

We report that following a partial myectomy, genes encoding muscle differentiation and morphogenic programs are downregulated over time. At the same time, cellular metabolism is rewired to accommodate the new needs, while new protein synthesis, along with lysosomal. and ubiquitin ligated proteolysis, is upregulated to reshape the cellular proteome. Programs related to DNA replication, repair, and chromosome condensation are similarly upregulated and prepare the cell to reenter the cell cycle. The rapid activation of epigenetic regulators of transcription likely reflects the genomic regulatory changes driving myocyte dedifferentiation. Based on this functional analysis, we formulated and tested the hypothesis that early-activated genes would be important for the early events of myocyte cellular reprogramming and dedifferentiation, while late-activated genes would regulate the later anatomic regeneration of the muscle but would not affect the initial reprogramming events. The results of our in vivo experiments reveal that myocyte

dedifferentiation appears to depend on transcriptional and epigenetic regulation, with key roles for early activated genes such as the Polycomb group factors ezh2 and suz12a. On the other hand, late-activated genes, such as fn1 (encoding fibronectin - an extracellular matrix protein involved in cell migration), are not required for cell reprogramming yet are necessary for tissue growth/elongation. These separate processes, and their distinct regulatory networks, provide critical insights into the regenerative process and could provide differential targets for harnessing de novo tissue regeneration therapeutically.

2.2 Materials and Methods

2.2.1 Zebrafish (*Danio rerio*) Rearing and Surgery

All animal work was performed in compliance with the Association for Research in Vision and Ophthalmology Statement for the Use of Animals in Ophthalmic and Vision Research and approved by the University of Michigan Committee on the Use and Care of Animals, protocol 06034. Sexually mature adult (4–18 months of age) wild-type and transgenic (α-actin::EGFP) zebrafish were spawned in our fish facility and raised according to standard protocol at 28°C with a 14-h light:10-h dark cycle.

Adult zebrafish were anesthetized using 0.05% tricaine methanosulfate (Tricaine-S; Western Chemical, Ferndale, WA) and approximately 50% of the lateral rectus (LR) muscle was surgically removed [9]. The amount of muscle remaining after surgery (46.77 ± 4.8%, average ± S.D.) was quantified by craniectomy as described previously [9]. No significant mortality was noted.

2.2.2 RNA Isolation and Sequencing

Zebrafish heads were decalcified for 2-3 days in a citrate-buffered (pH 5.6) solution containing 10% ethylenediamine-tetraacetic acid (EDTA; Thermo Fisher Scientific, Waltham, MA) saturated with ammonium sulfate (Promega, Madison, WI) to preserve RNA quality [19]. Specimens were directly placed in Shandon M-1 Embedding Matrix (Thermo Fisher Scientific, Waltham, MA) frozen on dry ice and coronal frozen sections (16 µm, cryostat temperature -35 to -40°C (CM3050S disposable blade cryostat; Leica Microsystems Inc., Buffalo Grove, IL)) were placed onto PEN-membrane framed slides (Leica, PN 11505151) and stored at -80ºC. Slides were washed and dehydrated (1 min 70% EtOH, 30 sec RNAse-free water, 30 sec 70% EtOH, 2 x 1 min 100% EtOH). LR muscle tissue was dissected from frozen sections using laser micro-dissection (LMD7000; Leica Microsystems Inc., Buffalo Grove, IL). Micro-dissected tissue was collected in 30 µL aliquots of RLT buffer (Qiagen, Valencia, CA) with 2-mercaptoethanol added (10 µL/mL). Pooled aliqouts from several dissected slides had areas that ranged from 27 to 71 million µm2 per sample. RNA was isolated in a fixed volume of 1 mL of TRIzol (Invitrogen, Inc., Carlsbad, CA) and the manufacturer's protocol was followed except for the addition of 0.2 mL of dH2O per mL of Trizol. Phase separation after chloroform addition was performed using phase lock gel tubes - Heavy 2 mL (5-Prime, Gaithersburg, MD). The RNA was further purified on microcolumns with DNAse treatment (ReliaPrep RNA Tissue Miniprep System, Promega, Madison WI) after addition of an equal volume of 100% EtOH to the Trizol aqueous layer and application to the column. Elution was with 15 µL RNAase free water.

RNA quantity was assessed using a Nanodrop spectrophotometer (Thermo Fisher Scientific, Waltham, MA) and both RNA quality and quantity were reassessed using an Agilent 2200 TapeStation (Agilent Technologies, Santa Clara, CA). Only samples with RIN's greater than 7 were further used for RNA-sequencing. Illumina's TruSeq Stranded mRNA Library Prep Kit and

0.1 - 4 µg total mRNA from pooled purified RNA samples were used for performing ribosomal-depletion (Ribo-Zero Gold rRNA Removal Kit, Illumina) and library preparation.

Sequencing was performed by the UM DNA Sequencing Core, using an Illumina Hi-Seq (50-cycle, single end read) platform (Illumina, Inc., San Diego, CA).

2.2.3 Transcriptome Assembly and Differentially Expressed Gene Identification

The sequencing reads files were concatenated into a single fastq file for each sample. The quality of the sequencing reads was assessed using FastQC v0.11.3 (http://www.bioinformatics.babraham.ac.uk/projects/fastqc/). The Tuxedo Suite package was used for alignment, differential expression analysis, and post-analysis diagnostics [20–22]. Briefly, all filtered reads were mapped to the reference genome followed by the transcriptome (GRCz10) using TopHat v2.0.13 and Bowtie v2.2.1. The default parameter settings for alignment were used, with the exception of: "--b2-very-sensitive" and "--max-intron-length" of 400 kbs as described previously [23]. Novel transcript discovery was not performed, employing "--no-coverage-search" and "--no-novel-juncs" to limit the read mapping to known transcripts. Cufflinks/CuffDiff v2.2.1 were used for expression quantitation and differential expression analysis, using NCBI GRCz10.fa as the reference genome sequence and NCBI GRCz10.gtf as the reference transcriptome annotation. For this analysis, the following parameters were used: "--multi-read-correct" to adjust expression calculations for reads that map in more than one locus, as well as "--compatible-hits-norm" and "--upper-quartile –norm" for normalization of expression values. Locally developed scripts were used to identify differentially expressed genes (DEG) based on three criteria: test status = "OK", FDR < 0.05, and fold change ≥ 1.5. Genes and isoforms were annotated using NCBI Entrez Gene IDs.

2.2.4 Clustering and Gene Set Analysis

Default parameter settings of the R package "cummeRbund" v2.14.0, part of the Tuxedo Suite package, were used to perform hierarchical clustering of the results (csDendro function with the "replicates=T" option;[24]).

Kyoto Encyclopedia of Genes and Genomes (KEGG) pathway and Gene ontology (GO) term analyses of the whole data set of DEG were performed using the "Generally Acceptable Gene set Enrichment" (GAGE v.2.22.0) package implemented in R [25,26]. Briefly, default parameter settings were used for comparisons of log-scaled gene set expression data between different time points (gage function with the options: compare=unpaired, q value < 0.1). Gene sets were derived through Bioconductor (www.bioconductor.org) and compiled using Entrez Gene IDs, mapping information, and gene set names contained in GAGE v2.22.0 and other actively maintained annotation packages (go.db v3.2.2 and kegg.db v3.2.2). The R package "pathview" v.1.12.0 was used to visualize gene set expression data in the context of functional pathways [27]. Expression data was rendered over pathway maps (pathview function with default parameters) derived from KEGG and compiled using KEGGgraph v1.30.0 [28].

CummeRbund was used to perform K-means (csCluster and csClusterPlot functions) clustering analyses setting the number of clusters from 3 to 30. The K-means analysis of 18 clusters was selected following two criteria: 1) maximize the number of clusters with new expression profiles; and 2) minimize the number of clusters that resulted from a simple division of a previous cluster into two new ones with the same expression profile. Thus, cluster number 8 (Figure 2.4 E) appeared in the analysis of only 4 clusters while cluster 15 (Figure 2.4 H) did not appear until the number of clusters was set to 18, and did not change in the following analyses (number of clusters set from 19 to 30). Locally developed scripts were used to track the cluster of each gene from one analysis to the next one (criteria number 2).

2.2.5 Morpholino Oligonucleotide Injection

Microinjection and electroporation of morpholino oligonucleotides (MOs; Gene-Tools, LLC, Philomath, OR) was used as described for knockdown experiments in adult zebrafish [31–33]. Briefly, lissamine-tagged MOs (~0.2 μL, 1mM in nuclease-free H_2O) were directly microinjected into the LR muscle followed by electroporation (6 to 10 pulses at 48 V/cm, BTX ECM830 electroporator; Harvard Apparatus, Holliston, MA). Microinjections were performed 3 hours prior to LR injury, and MO uptake was confirmed via lissamine fluorescence prior to myectomy. MOs were designed to target the 5'-UTR of respective mRNAs (translational blocking MOs), and were compared to a standard control MO (CON) targeting a human beta-globin intron mutation. When possible, previously published MOs were utilized (Table 2.1). For all others, MO sequence design was performed as a service by Gene Tools. All MOs were injected at the same concentration, and all experiments were performed using 5 fish per experimental group per time point, unless stated otherwise in the text and/or figure legend. No significant mortality was noted.

Table 2.1: Sequence of the morpholino antisense oligonucleotides (MOs).

	Sequence	Reference
ezh2	5′-CGATTTCCTCCCGGTCAATCCCATG	[34]
fn1a	5′-TTTTTTCACAGGTGCGATTGAACAC	[35]
suz12a	5′-GAGCCATCCTAAAATAGCGTTCGTG	[36]
Control (CON)	5′-CCTCTTACCTCAGTTACAATTTATA	[37]

2.2.6 Specimen Processing and Cell Proliferation Assay

Zebrafish heads were removed and fixed in 4% paraformaldehyde in PBS (PFA; Sigma-Aldrich, St. Louis, MO) overnight at 4ºC. Decalcification was performed for 48-h using Morse's solution (45% formic acid in H2O, ACROS Organics, Fair Lawn, NJ; 20% sodium citrate in H2O, R&D Systems, Bristol, UK). Fixed and decalcified tissues were cryopreserved with 20% sucrose in PBS (ACROS Organics, Fair Lawn, NJ), embedded in OCT (Thermo Fisher Scientific, Waltham, MA), and frozen.

Cellular proliferation was assessed by intra-peritoneal injections of 5-ethynyl-2'-deoxyuridine (EdU; Invitrogen, Inc., Carlsbad, CA) [38]. Wild-type fish were injected with EdU (25 μL, 10 mM in PBS) at 44 h post injury and sacrificed 4 h later (Figure 2.5 A). The injured muscles of 4-8 fish per experimental group were evaluated microscopically using transverse frozen sections (10 μm) as described previously [9]. EdU+ and total (DAPI) nuclei were counted from 3-4 non-sequential sections per muscle (more than 30 sections per experiment were analyzed), representing approximately 700 total nuclei (range: 296-1176) per muscle. Cell proliferation is represented as the percentage of EdU+ nuclei in the injured muscle of target gene MO injected fish relative to the percentage of EdU+ nuclei in the injured muscle of control MO injected fish.

2.2.7 Regeneration Assay

Transgenic α-actin::EGFP zebrafish were used to visualize the LR muscles and measure regeneration by craniectomy 4 or 8 dpi (Figure 2.6 A) as described previously [9]. Briefly, calvarial bones of the skull and the brain were removed to allow visualization of the skull base where both LR muscles originate. Regeneration is represented as the length of the injured muscle compared to the non-injured muscle of MO injected fish relative to the length of the injured muscle compared

to the non-injured muscle of control MO injected fish. All experiments were performed using 5 fish per experimental group per time point unless stated otherwise in the text and/or figure legend.

2.3 Results

2.3.1 Differentially Expressed Genes During Early Muscle Regeneration

Adult zebrafish EOMs can regenerate de novo using residual myocytes that reprogram into dedifferentiated myoblasts capable of proliferation. Starting with "postmitotic" myocytes, the entire reprogramming process takes just under 20 h, at which time myonuclear proliferation can be detected [9]. To characterize the reprogramming process at the transcriptional level, we chose to focus on two time points – 9 and 18 hpi – that occur prior to cell cycle reentry by dedifferentiated myoblasts. RNA was isolated from uninjured lateral rectus (LR) muscles (CON) and injured LR muscles at 9 (H9) and 18 (H18) hpi, followed by ribosomal RNA depletion and reverse transcription to prepare a cDNA library for deep sequencing utilizing an Illumina Hi-Seq platform. Four replicates were used for CON and five replicates were used for both H9 and H18; biological replicates consisted of pooled LR tissue from 15 to 20 zebrafish. Mapping against the zebrafish reference genome sequence revealed alignment to 31,014 unique features.

A total of 6596 unique differentially expressed genes (DEG) were identified among CON, H9, and H18 samples. There were more DEGs in CON vs. H9 and CON vs. H18 comparisons (4717 and 4735 genes, respectively) than in H9 vs. H18 comparisons (1923 genes) (Figure 2.1 A). A heat map of all DEG revealed the occurrence of multiple gene subsets with distinct expression patterns (Figure 2.1 B). 538 DEGs were common to all three comparisons and the highest overlap occurred between CON vs. H9 and CON vs. H18 comparisons (2793 genes) (Figure 2.1 C).

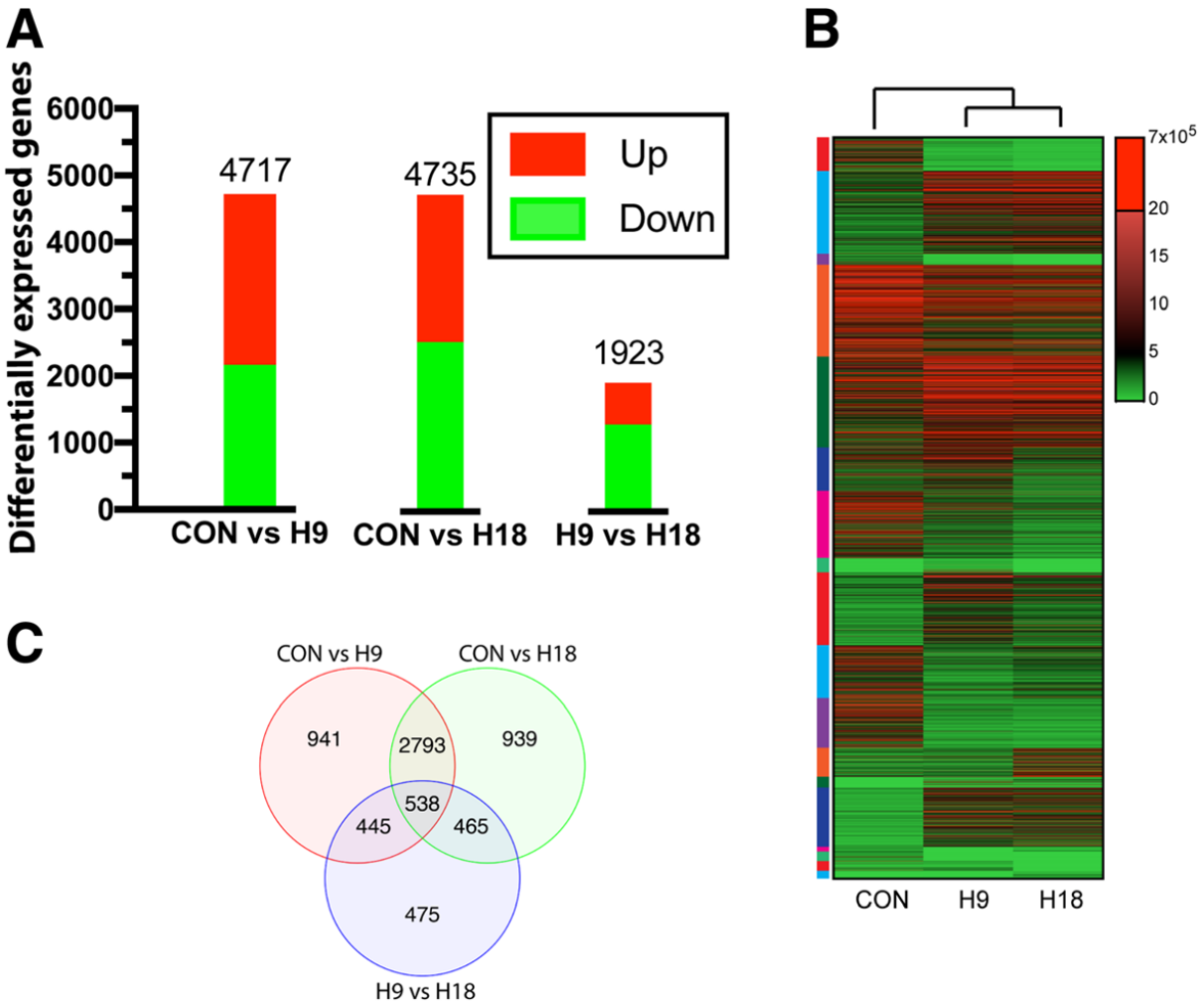

Figure 2.1: Differential gene expression during muscle regeneration.
A. Distribution of DEG of the three pair-wise comparisons. B. Heat map of DEG. Sample names are listed below the heat maps and the expression-based hierarchical clustering separating CON from H9 and H18 samples is shown above it. Color scale (right) indicates gene expression (FPKM). FPKM <5 is shown in green and indicates low transcript abundance. FPKM >5 is shown in red and indicates high transcript abundance. DEG are ordered according to numeric clusters from Figure 2.4, represented as a color bar on the left side (color code is shown in Figure 2.4 over each cluster plot). C. Venn diagram showing overlap of DEG between CON, H9, and H18 sample comparisons.

2.3.2 Functional Classification of Differentially Expressed Genes (DEG)

Comparisons between CON, H9, and H18 samples revealed that the majority of significantly perturbed KEGG pathways were downregulated (Figure 2.2 A-E). About half of these

downregulated pathways (5 of 11) were perturbed in CON vs. H9 and CON vs. H18 comparisons but not in the H9 vs. H18 comparison, thus indicating a rapid and sustained change starting at 9 hpi; see cardiac muscle contraction pathway (dre04260) for example (Figure 2.2 F). Almost all other downregulated pathways (4 of 11) were perturbed in each comparison indicating a gradual change over time; see calcium signaling pathway (dre04020) for example. On the other hand upregulation of the phagosome pathway (dre04145) was common to all three comparisons while the lysosome pathway (dre04142) was upregulated in only CON vs. H18 and H9 vs. H18 comparisons (Figure 2.2 G).

The magnitude of lysosome pathway (dre04142) upregulation between H9 and H18 was the largest of all comparisons suggesting a critical role during muscle remodeling at 18 hpi. The downregulation of the pathways for pyruvate metabolism (dre00620), oxidative phosphorylation (dre00190), citrate cycle (TCA cycle) (dre00020), 2-oxocarboxylic acid metabolism (mainly TCA cycle components; dre01210), glycolysis/gluconeogenesis (dre00010), and carbon metabolism (dre01200) suggests a reduction in the mitochondrial oxidative capacity of reprogramming cells. Interestingly, genes of the MAPK signaling pathway (dre04010) showed a very dynamic expression pattern that was only significantly downregulated between H9 and H18. This would indicate a change in the cellular MAPK configuration during reprogramming and expands on our characterization of the Erk pathway in EOM regeneration [19].

Comparisons between CON, H9, and H18 samples revealed that, like KEGG pathways, the majority of significantly perturbed GO terms were downregulated (Figure 2.3 A-I). Consequently, there was a general expression decrease of genes included in these GO terms (Figure 2.3 K-L). GO terms downregulated in all three comparisons (representing a gradual downregulation) and in CON vs. H18 and H9 vs. H18 (representing a late decrease in gene expression levels) were related

to similar categories including muscle development, differentiation and function [muscle fiber development (GO:0048747), muscle cell differentiation (GO:0042692), z disc (GO:0030018), and striated muscle contraction (GO:0006941)]; nucleic acid metabolism [nucleoside metabolic process (GO:0009116), pyridine nucleotide metabolic process (GO:0019362), and purine nucleotide metabolic process (GO:0006163)]; energy metabolism [oxidation-reduction process (GO:0055114), tricarboxylic acid cycle (GO:0006099), proton-transporting ATP synthase complex (GO:0045259), mitochondrial inner membrane (GO:0005743), and carbohydrate catabolic process (GO:0016052)]; and calcium related processes [cellular calcium ion homeostasis (GO:0006874), calcium ion binding (GO:0005509), and calcium ion transport (GO:0006816)]. Interestingly, genes of GO terms related to catabolic functions were mainly upregulated at the expression level (Figure 2.3 J-L). Specifically, GO term upregulation was only observed in CON vs. H18 and H9 vs. H18 comparisons and consisted primarily of catabolic functions such as cysteine-type peptidase activity (GO:0008234), lysosome (GO:0005764), and cellular protein catabolic process (GO:0044257). The internal consistency between the KEGG pathways and GO terms obtained (e.g., cardiac muscle contraction and striated muscle contraction, calcium signaling pathway, cellular calcium ion homeostasis, and lysosome in both KEGG and GO analyses) supports the validity of the results.

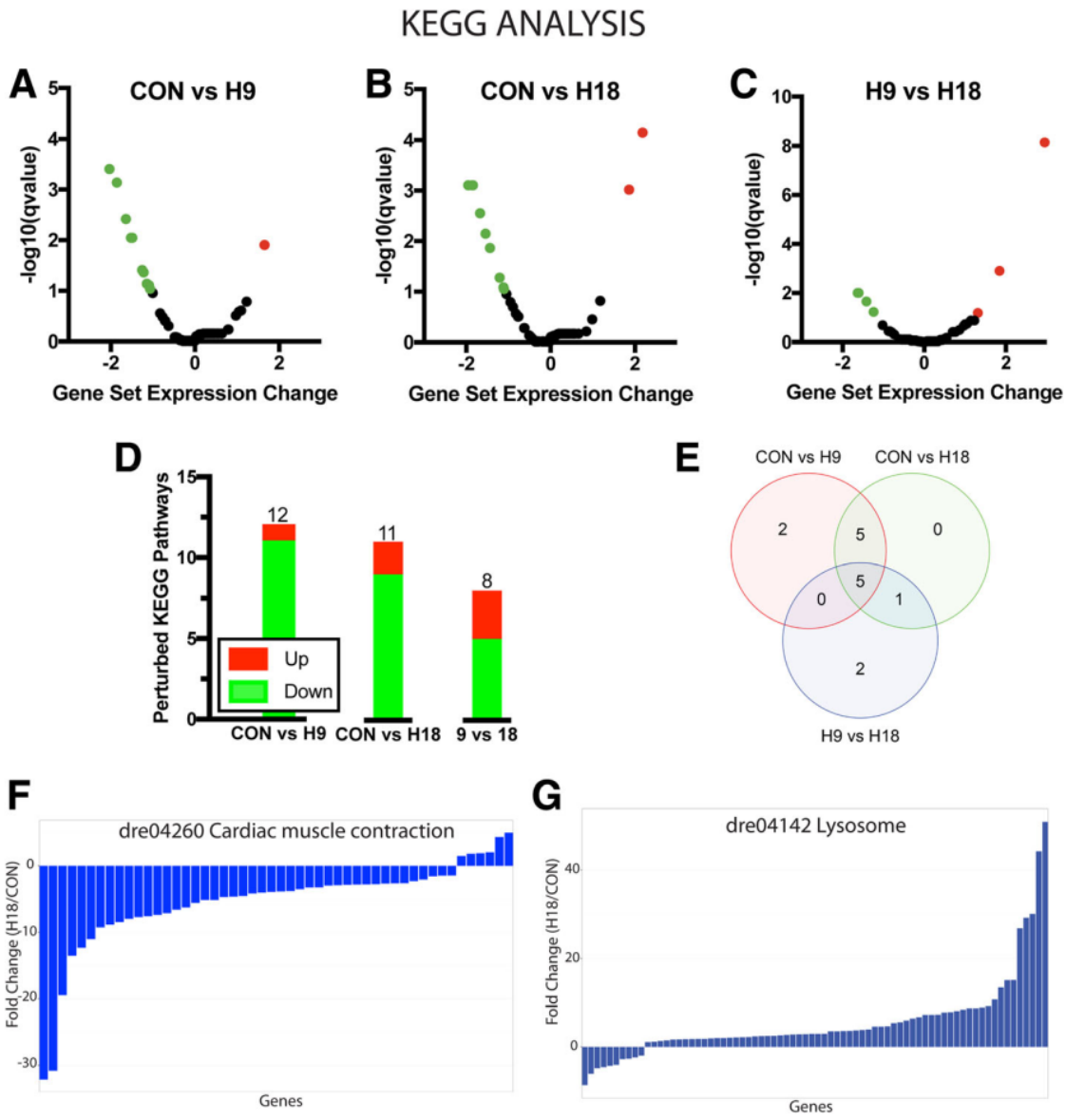

Figure 2.2: KEGG pathway classification of differentially expressed genes.
Volcano plots of KEGG pathways in CON vs H9 (A), CON vs H18 (B), and H9 vs. H18 (C) comparisons. Gene set expression change (x-axis) of DEG within a KEGG pathway is a normalized enrichment score based on comparisons between different time points and relative to the entire DEG gene set. Significantly downregulated pathways are shown in green and significantly upregulated pathways are shown in red. D Distribution of significantly perturbed KEGG pathways in the three pair-wise comparisons. Significantly downregulated terms are shown in green. Significantly upregulated terms are shown in red. Cutoff for significance was q < 0.1 according to default values and parameters of the R package "gage" v2.22.0. E Venn diagram showing overlap of perturbed KEGG terms between CON, H9, and H18 sample comparisons. Cutoff for significance was q < 0.1 according to default values and parameters of

the R package “gage” v2.22.0. Fold change (H18/CON) of the DEG of the dre04260 Cardiac muscle contraction (F) and dre04142 Lysosome (G) KEGG pathways.

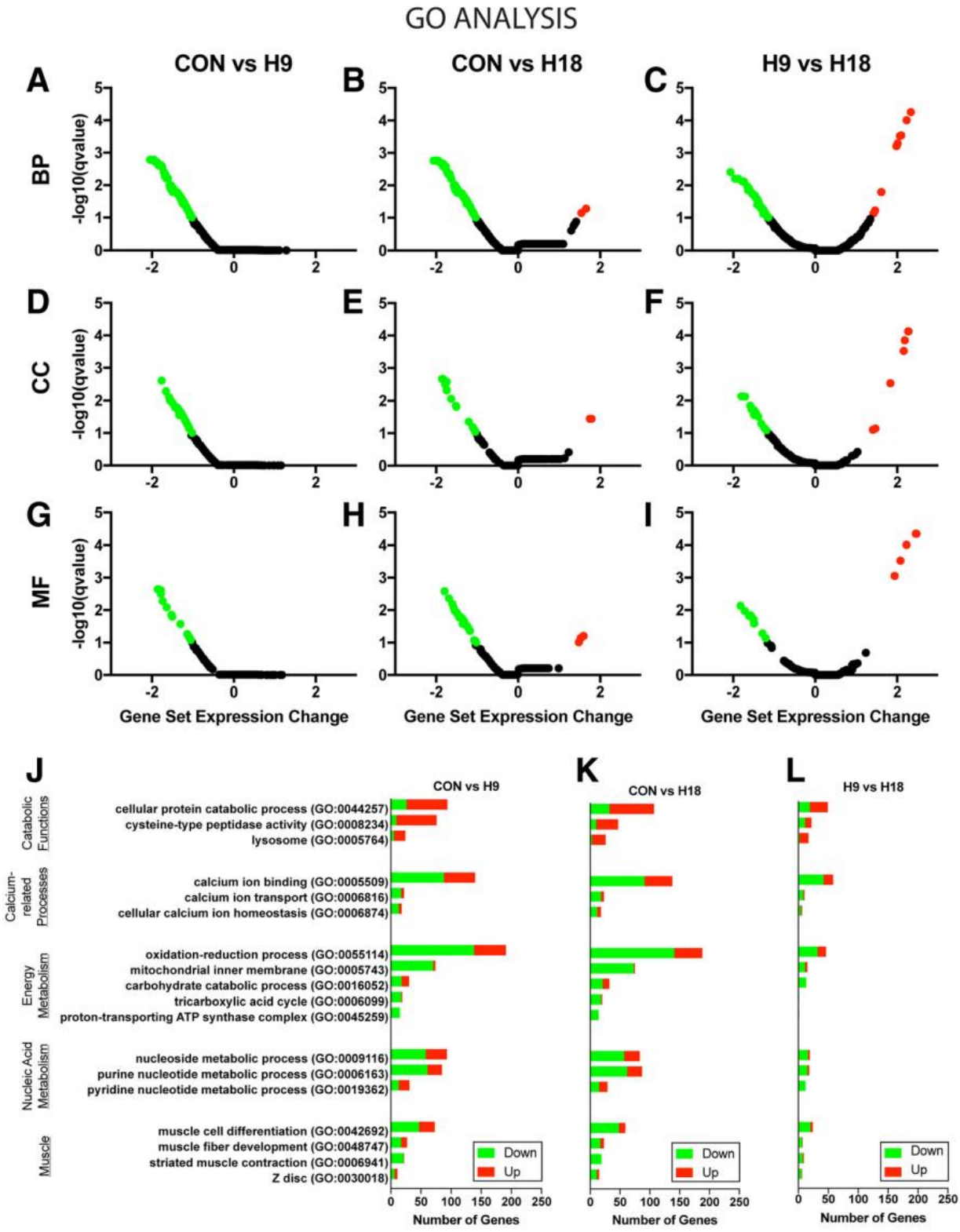

Figure 2.3: GO enrichment analysis of differentially expressed genes.
Volcano plots of significantly perturbed GO terms of biological process (BP; A, B, C), cellular component (CC; D, E, F) and molecular function (MF; G, H, I) in CON vs H9 (A, D, G), CON vs H18 (B, E, H), and H9 vs. H18 (C, F, I) comparisons. Gene set expression change (x-axis) of DEG mapped to GO term is a normalized enrichment score based on comparisons between different time points and relative to the entire DEG gene set. Significantly downregulated terms are shown in green and significantly upregulated terms are shown in red. Cutoff for significance was $q < 0.1$ according to default values and parameters of the R package "gage" v2.22.0. Distribution of DEG of the terms in the CON vs H9 (J), CON vs H18 (K), and H9 vs. H18 (L) comparisons.

2.3.3 Gene Expression Profiles

K-means clustering of DEG identified 18 clusters that were further arranged by expression patterns into 4 major profiles composed of multiple gene clusters and 6 minor profiles composed of a single gene cluster (Figure 2.4). The first major profile, "A: Progressive Downregulation", was composed of 994 genes (clusters 1, 3, and 7, Figure 2.4 A) and showed progressive and significant downregulation at 9 hpi and 18 hpi. This profile groups together genes such as myogenic factor 6 (*myf6*); collagen, type XV, alpha 1a (*col15a1a*); obscurin, cytoskeletal calmodulin and titin-interacting RhoGEF a (*obscna*); popeye domain containing 2 (*popdc2*); acetylcholinesterase (*ache*); matrix metallopeptidase 23bb (*mmp23bb*); serine peptidase inhibitor, Kunitz type 1 b (*spint1b*); Indian hedgehog homolog a (*ihha*); lefty2 (*lft2*); titin, tandem duplicate 1 (*ttnb*); periostin, osteoblast specific factor b (*postnb*); sarcoglycan, delta, dystrophinassociated glycoprotein (*sgcd*); SIX homeobox 1b (*six1b*); SET and MYND domain containing 1a (*smyda1*); and SWI/SNF related, matrix associated, actin dependent regulator of chromatin, subfamily a, member 1 (*smarca1*).

The second major profile, "B: Persistent Downregulation", was composed of 1723 genes (clusters 4, 10, and 11, Figure 2.4 B) and showed downregulation at 9 hpi that was maintained at similar levels through 18 hpi. Representative genes of this profile include laminin alpha 2 (lama2);

myogenin (myog); collagen, type VI, alpha 1 (col6a1); caveolae associated protein 4a (murca); myogenic differentiation 1 (myod1); myocyte enhancer factor 2d (mef2d); insulin-like growth factor 1a receptor (igf1ra); sarcoglycan beta, dystrophin-associated glycoprotein (sgcb); myosin, heavy polypeptide 2, fast muscle specific (myhz2); laminin beta 2, laminin S (lamb2); dystropin (dmd); tropomodulin 4, muscle (tmod4); tropomodulin 1 (tmod1); NDRG family member 4 (ndrg4); insulin-like growth factor binding protein 3 (igfbp3); LIM domain binding 3a (ldb3a); and RNA binding motif protein 24b (rbm24b).

The third major profile, "C: Persistent Upregulation", was composed of 2172 genes (clusters 2, 5, 13, and 14, Figure 2.4 C) that were upregulated at 9 hpi and maintained their expression levels through 18 hpi. Representative examples from this profile include DNA (cytosine-5-)-methyltransferase 3 alpha a (dnmt3aa); SWI/SNF related, matrix associated, actin dependent regulator of chromatin, subfamily a, member 5 (smarca5); ATPase, H+ transporting, lysosomal, V1 subunit E1b (atp6v1e1b); RNA binding protein, fox-1 homolog (C. elegans) 2 (rbfox2); selenoprotein N, 1 (sepn1); protein arginine methyltransferase 1 (prmt1); metastasis associated 1 family, member 2 (mta2); histone deacetylase 1 (hdac1); proteasome 26S subunit, non-ATPase 11b (psmd11b); ubiquitin-like modifier activating enzyme 1 (uba1); mesoderm posterior aa (mespaa); cardiotrophin-like cytokine factor 1 (clcf1); minichromosome maintenance 10 replication initiation factor (mcm10); integrin, alpha 6a (itga6a); myelocytomatosis oncogene homolog (myc h); SWI/SNF related, matrix associated, actin dependent regulator of chromatin, subfamily a, member 4a (smarca4a); matrix metallopeptidase 9 (mmp9); and regulator of chromosome condensation 2 (rcc2).

The fourth major profile, "D: Delayed Downregulation", was composed of 477 genes (clusters 6 and 17, Figure 2.4 D) that were unchanged through 9 hpi but were significantly

downregulated at 18 hpi. The following are representative examples of the genes included in this profile: autophagy/beclin-1 regulator 1a (ambra1); unc- 45 myosin chaperone B (unc45b); cadherin 5 (cdh5); insulin-like growth factor 1b receptor (igf1rb); actin, alpha 2, smooth muscle, aorta (acta2); methionine adenosyltransferase II, alpha a (mat2aa); and troponin I type 1a, skeletal, slow (tnn1ai).

The remaining single cluster profiles represented more dynamic "switch-like" expression patterns (Figure 2.4 E-J) and, as such, were of particular interest. Of those, "E: Transient Activation" (cluster 8, Figure 2.4 E) contained 129 genes (such as mesoderm posterior bb, mespbb; nanor, nnr; hemoglobin beta embryonic-2, hbbe2; tetraspanin 34, tspan34; and claudin 1, cldn1) that were only expressed at 9 hpi, while "F: Transient Upregulation" (cluster 9, Figure 2.4 F) contained 648 genes (e.g., enhancer of zeste 2 polycomb repressive complex 2 subunit, ezh2; coactivator-associated arginine methyltransferase 1, carm1; SWI/SNF related, matrix associated, actin dependent regulator of chromatin, subfamily d, member 1, smarcd1; protein arginine methyltransferase 5 and 7, prmt5 and prmt7; MYC proto-oncogene, bHLH transcription factor b, mycb) that were present in uninjured muscles (CON), peaked at 9 hpi, and returned to control levels at 18 hpi. Such rapid yet transient changes in expression suggest involvement of these gene clusters in the initiation of cell reprogramming. Profile "G: Late Upregulation" (cluster 12, Figure 2.4 G) contained genes upregulated at 18 hpi such as fibronectin 1a (fn1a); DNA (cytosine-5-)-methyltransferase 1 (dnmt1); midkine a (mdka); DNA primase subunit 2 (prim2); or DNA topoisomerase II alpha (top2a). Profile "H: Transient Repression" (cluster 15, Figure 2.4 H) contained 42 genes present in uninjured (CON) muscles and at 18 hpi but not expressed at 9 hpi. Representative examples are histone H2A, sperm-like; claudin d (cldnd); period circadian clock 1a (per1a); and glutathione peroxidase 7 (gpx7). Profile "I: Persistent Repression" (cluster 16,

Figure 2.4 I) contained 85 genes that were only expressed in uninjured (CON) muscles (e.g., chymotrypsinogen B1, ctrb1; cysteine three histidine 1, cth1; cyclin A1, ccna1) while the 67 genes of profile "J: Late Activation" (cluster 18, Figure 2.4 J) displayed the opposite trend and were only expressed at 18 hpi (although this was the cluster with the highest content of non-coding transcripts, see below, some representative coding genes are aspartic peptidase, retroviral-like 1, asprv1; chemokine (C-C motif) ligand 27b, ccl27b; and heparan sulfate 6-O-sulfotransferase 3a, hs6st3a).

Panther GO term analysis of the four major profiles revealed GO terms consistent with the previous analysis conferring reliability to the results (Figure 2.4 K, L). Analysis of "A: Progressive Downregulation" genes showed enrichment in categories of muscle organ development (GO:0007517), small molecule metabolic process (GO:0044281), and single-organism cellular process (GO:0044763) (Figure 2.4 K). Panther analysis identified 15 different enriched categories in "B: Persistent Downregulation" (Figure 2.4 K), including skeletal muscle organ development (GO:0060538), myofibril assembly (GO:0030239), heart development (GO:0007507), and organ morphogenesis (GO:0009887). "C: Persistent Upregulation" had 31 overrepresented categories (Figure 2.4 L), the highest number of any Panther analysis. Several RNA processing [such as mRNA splicing, via spliceosome (GO:0000398), RNA secondary structure unwinding (GO:0010501), RNA export from nucleus (GO:0006405), mRNA transport (GO:0051028)] and protein translation [protein folding (GO:0006457), translational initiation (GO:0006413), ribosomal large subunit biogenesis (GO:0042273), cytoplasmic translation (GO:0002181)] or modification [protein folding (GO:0006457) and protein N-linked glycosylation (GO:0006487)] categories were identified. At the same time, protein degradation [ubiquitin-dependent protein catabolic process (GO:0006511) and lysosome organization (GO:0007040)] and fin regeneration

(GO:0031101) categories were also enriched. Enriched categories in "D: Delayed Downregulation" (Figure 2.4 K) were related to developmental and differentiation processes such as cell differentiation (GO:0030154) or tissue development (GO:0009888).

Interestingly, the Panther GO analysis of single cluster profiles revealed relevant terms not noted in other profiles or the GAGE analysis. Enriched terms in "F: Transient Upregulation" were related to the categories of gene transcription and ribosome formation and included: regulation of gene expression, epigenetic (GO:0040029), transcription, DNAtemplated (GO:0006351), and maturation of SSU-rRNA from tricistronic rRNA transcript (SSU-rRNA, 5.8S rRNA, LSU-rRNA) (GO:0000462). Enriched categories in "G: Late Upregulation" were related to DNA replication and repair [DNA replication initiation (GO:0006270), mismatch repair (GO:0006298), and mitotic chromosome condensation (GO:0007076)]. Profiles "E: Transient Activation", "H: Transient Repression", "I: Persistent Repression", and "J: Late Activation" did not have enriched GO terms or categories because of the low percentage of GO annotations for genes in these clusters (Table 2.2). Interestingly, the gene clusters with lowest percentage of GO annotated terms had both a higher percentage of lncRNAs (Table 2.3), which remain to be functionally annotated, and the most dynamic "switch-like" expression patterns (Figure 2.4).

Table 2.2: GO term annotations for gene expression profiles.

Profile (cluster)	Gene number	Annotated genes	%
A (1/3/7)	994	671	67.51
B (4/10/11)	1723	1296	75.22
C (2/5/13/14)	2172	1682	77.44
D (6/17)	477	309	64.78
E (8)	129	23	17.83
F (9)	648	476	73.46
G (12)	259	32	12.36
H (15)	42	14	33.33
I (16)	85	24	28.24
J (18)	67	11	16.42

Table 2.3: Distribution of coding (cRNA) and long non-coding (lncRNA) RNA by cluster

Cluster	Total	cRNA (%)	lncRNA (%)
1	301	97.67	2.33
2	738	99.86	0.14
3	98	83.67	16.33
4	813	98.65	1.35
5	810	99.38	0.62
6	389	98.71	1.29
7	595	98.32	1.68
8	129	71.32	28.68
9	648	99.23	0.77
10	472	99.36	0.64
11	438	98.86	1.14
12	259	100.00	0.00
13	96	82.29	17.71
14	528	99.43	0.57
15	42	73.81	26.19
16	85	77.65	22.35
17	88	73.86	26.14
18	67	62.69	37.31

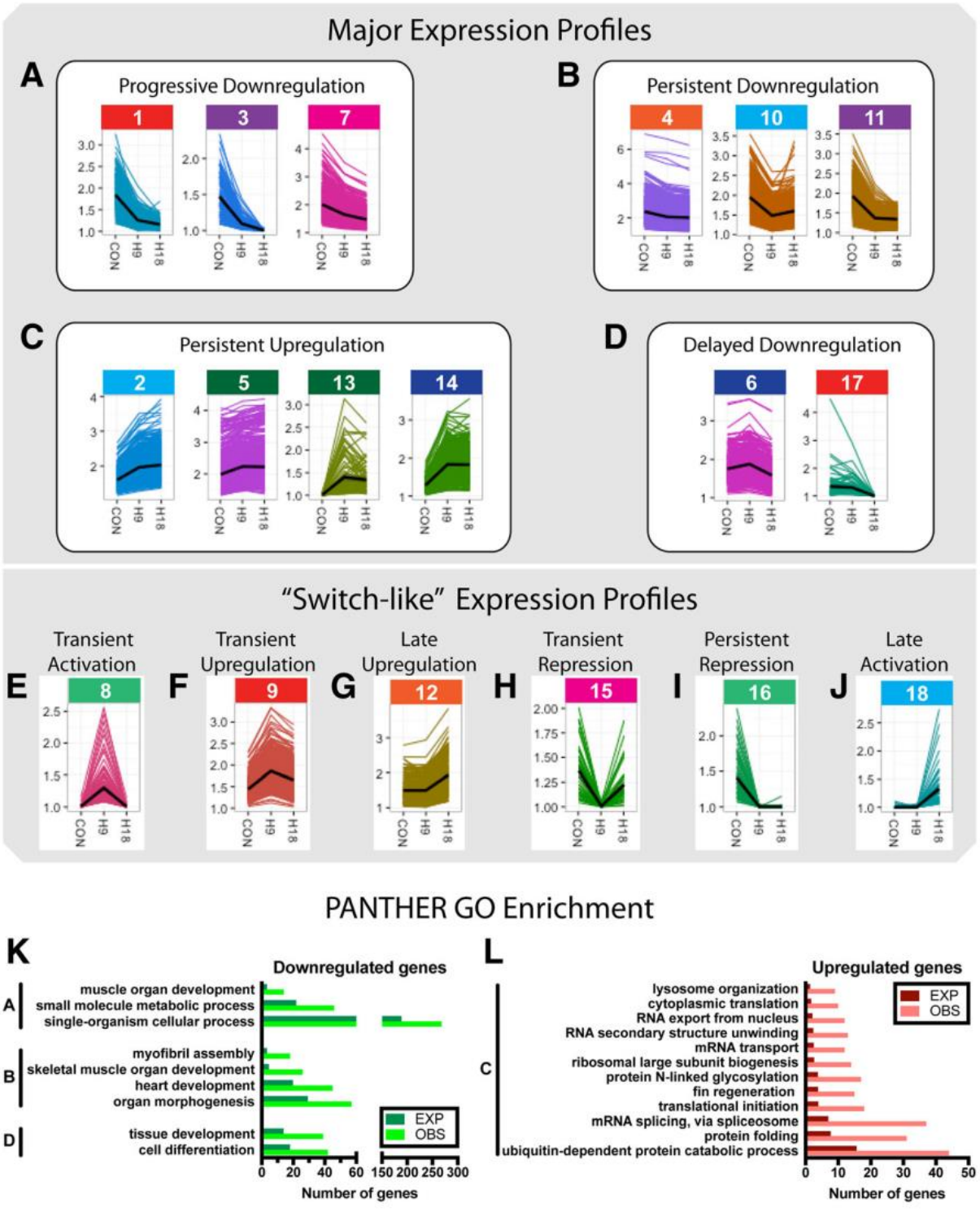

Figure 2.4: Expression profiles of gene clusters.
K-means method was used to divide DEG into 18 clusters that were grouped, according to their expression profiles, into 4 major profiles (A-D) and 6 profiles composed of single gene clusters (E-J). A The first major profile, "Progressive Downregulation" (clusters 1, 3, and 7) showed

progressive and significant downregulation at 9 hpi and 18 hpi. B The second major profile, "Persistent Downregulation" (clusters 4, 10, and 11) grouped downregulated genes at 9 hpi that maintained similar expression levels through 18 hpi. C Genes of the third major profile, "Persistent Upregulation" (clusters 2, 5, 13, and 14), were upregulated at 9 hpi and maintained through 18 hpi. D The fourth major profile, "Delayed Downregulation" (clusters 6 and 17) included genes whose expression was significantly downregulated only at 18 hpi. The remaining single cluster profiles (E-J) presented more dynamic time changes. E "Transient Activation" (cluster 8) contains genes that were only expressed at 9 hpi. F "Transient Upregulation" (cluster 9) represents genes present in control that were significantly upregulated at 9 hpi and returned to control levels at 18 hpi. G "Late Upregulation" (cluster 12) contains genes whose expression was upregulated at 18 hpi. H "Transient Repression" (cluster 15) is composed of genes expressed in control muscles and at 18 hpi but not expressed at 9 hpi. I "Persistent Repression" (cluster 16) contains genes that were only expressed in control muscles. J "Late Activation" (cluster 18) displayed the opposite trend with genes only expressed at 18 hpi. The color behind the cluster number is related to the color bar in Figure 2.1 B. (K-L) GO enrichment analysis of the major gene expression profiles A-D. (K) Significantly overrepresented GO categories in profiles with genes downregulated over time (profiles A, B and D). (L) Significantly overrepresented GO categories in profile C which had persistently upregulated genes. Categories with $P < 0.05$ were considered as significantly overrepresented

2.3.4 Expression Timing Correlates with Temporal Roles During Muscle Regeneration

As anticipated, a large subset of epigenetic regulators and transcription factors were induced early in the reprogramming process (profile "F: Transient Upregulation"; Figure 2.4 F). In fact, the GO term "regulation of gene expression, epigenetic" (GO:0040029) was significantly enriched in profile F. All this suggested that at least a subset of these factors might be mechanistically involved in allowing post-mitotic myocytes to dedifferentiate into proliferative myoblasts and we thus decided to focus on transcription factors and epigenetic regulators. We further hypothesized that early-activated genes would play a particularly important role in the reprogramming and dedifferentiation of injured myocytes, and tested the hypothesis using gene knockdown experiments using antisense morpholino oligonucleotide (MO), a technique widely used to perform tissue-specific knockdown experiments in adult zebrafish [31–33] and other model organisms such as adult axolotls [39], xenopus larvae [40] or chick [41] and mouse [42] embryos.

Briefly, lissamine-tagged MOs are injected and then electroporated into the LR muscle 3 h prior to myectomy injury (Figures 2.5 A and 2.6 A). LR-specific MO uptake is detected via lissamine fluorescence within muscle fibers, persisting through 8 dpi, and without affecting the adjoining EOM (Figure 2.6 B). Proliferation at 48 hpi is assayed via EdU uptake as a surrogate for myocyte reprogramming, since proliferation of dedifferentiated myoblasts represents the final step of the reprogramming process (Figure 2.5 E). Additionally, we physically measure the length of the regenerating LR muscle in order to assess anatomic regeneration (Figure 2.6 B).

Because of their rapid induction (Figure 2.5 B), gene induction in a "switch-like" fashion (i.e., expression profile "F: Transient Upregulation"), and known roles as epigenetic regulators of cell identity [43], we assessed the role of Polycomb group factors in myocyte reprogramming. Knockdown of the Polycomb Repressive Complex 2 (PRC2) factors Ezh2 and Suz12a revealed a significant reduction in the number of proliferating dedifferentiated myoblasts during what is normally peak proliferation [9], between 44 and 48 hpi (Figure 2.5 E), supporting a key role in the reprogramming process. Furthermore, physical measurement of LR muscle length following Polycomb group factor knockdown revealed a significant delay in muscle regeneration (Figure 2.6 C) that was consistent with the inhibition of reprogramming and subsequent proliferation. These findings reveal a key role for PRC2 factors in regulating myocyte reprogramming.

Next, we hypothesized that since myocyte dedifferentiation to myoblasts represents the first step of the muscleto-mesenchymal transition (MMT) observed during EOM regeneration [9], later activated (i.e., 18 hpi) genes would not be related to myocyte reprogramming and cell cycle reentry but rather play important roles in muscle tissue anatomic regeneration. Among genes in the single cluster profile "G: Late Upregulation", fn1a, encoding fibronectin –an extracellular matrix (ECM) glycoprotein whose expression is activated during mesenchymal transitions and

promotes cell migration [44] – was notable due to its magnitude of induction between 9 and 18 hpi (Figure 2.5 C). As hypothesized, knockdown of Fn1a had no effect on cell proliferation (Figure 2.5 E). However, it resulted in a large reduction in anatomic LR muscle tissue regeneration (Figure 2.6 B and C). This is consistent with the hypothesis that genes activated later in the response were: (1) not significant for the cellular reprogramming process, and (2) more important for later events of the regenerative process that include muscle growth through myoblast migration and/or myofiber fusion.

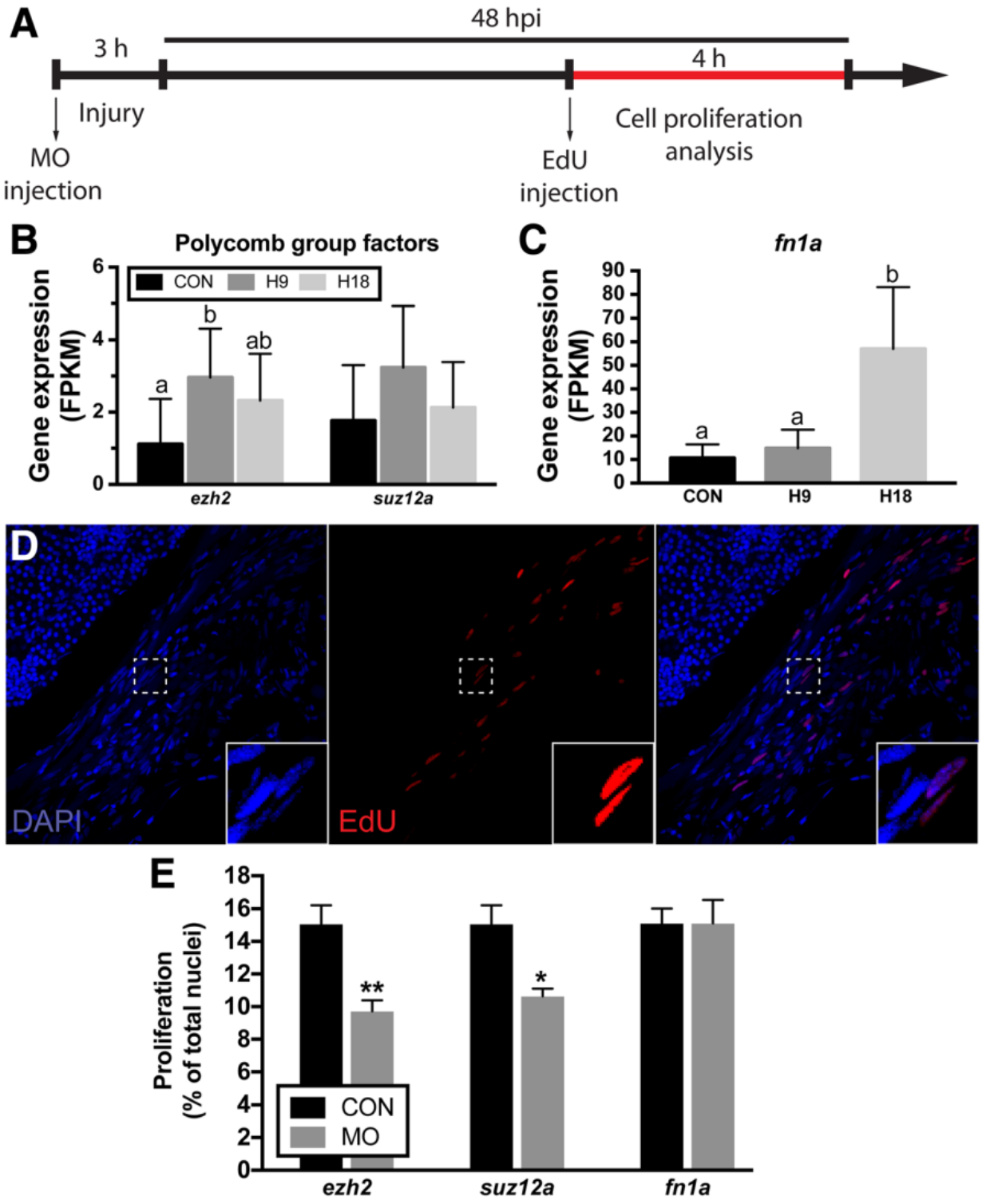

Figure 2.5: Proliferation following knockdown of select differentially expressed genes. A. LR regeneration involves a proliferative burst that generates enough cells to replace lost tissue. EdU assays were performed according to the schematic. B. Gene expression (FPKM) of epigenetics selected genes, ezh2 and suz12a. C. Fibronectin 1a gene expression (FPKM). D.

Confocal microscopy of cell proliferation in the regenerating muscle. Inset shows higher resolution detail of the box in the panel. DAPI staining (blue) shows the total number of nuclei in the muscle (left) and EdU staining (red) shows proliferating nuclei (middle). Merged panel (right). E. Quantification of cell proliferation in injured LR at 48 hpi. Values are averages ± SEM ($n \geq 5$) in control MO or target gene MO injected fish. Different letters (a, b, ab) in (b) and (c) indicate significant differences among time points. * $P < 0.05$; ** $P < 0.01$; Student's t-test.

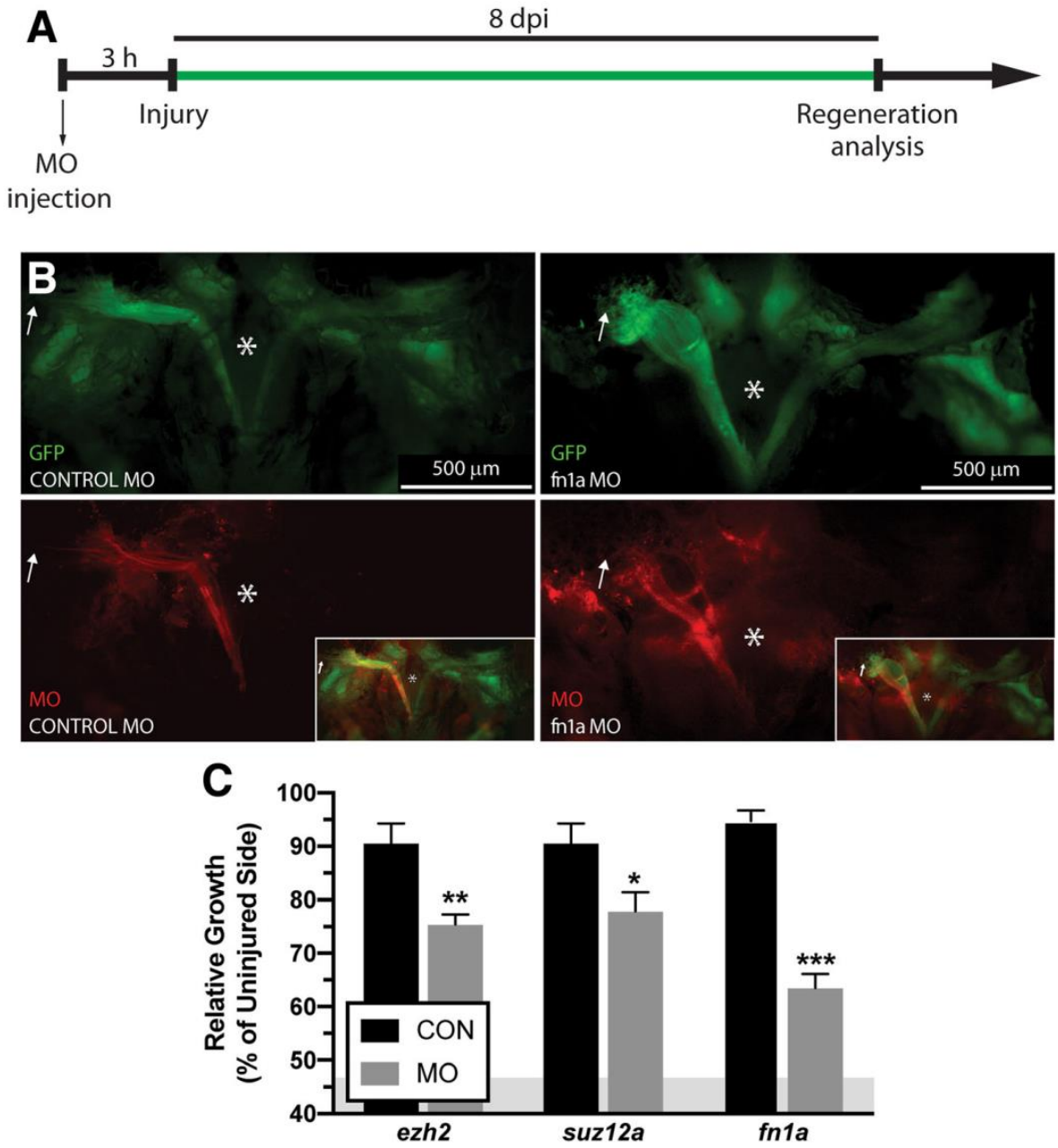

Figure 2.6: Regeneration following knockdown of select differentially expressed genes. A. LR regeneration assays were performed according to the schematic. B. Craniectomy was performed to visualize EGFP-labeled muscle at 8 dpi. Brain was removed to allow visualization

of the skull base (*) Microinjected MOs are detected throughout the entire regenerating muscle, including the distal ends (white arrow). Control MO (left) and fn1a MO (right) injected fish are pictured. C. Quantification of LR regeneration at 8 dpi, all MOs targeting specific mRNA decreased muscle regeneration at 8 dpi compared to control MO injected fish. Values are averages ± SEM (n = 5–7) in control MO or target gene MO injected fish. *P < 0.05; **P < 0.01; *** P < 0.001; Student's t-test. The residual muscle left following myectomy surgery (46.77 ± 4.8%, average ± SD) is represented as a grey area in C.

2.4 Discussion

Differentiated cells are marked by an epigenetic program that determines which genes are to be expressed or repressed in a genome-wide fashion [45–47]. The myocyte program involves expression of genes encoding sarcomeric proteins and repression of cell cycle genes and those associated with different, non-muscle tissue types (e.g., liver). Reprogramming a differentiated cell into a different identity, whether or not of similar cell lineage, would involve reprogramming every aspect of that cell's biology – its transcriptome, metabolome, and proteome. Myocytes are among the most specialized of cells and are considered "post-mitotic." Yet, in zebrafish EOMs, catastrophic muscle injury triggers rapid myocyte reprogramming (within 20 hpi) resulting in a large population of proliferating dedifferentiated myoblasts that repopulate and de novo regenerate the absent muscle [9,48,49]. This surprising discovery has provided a unique opportunity to study limited cellular reprogramming that maintains lineage restriction yet is capable of regenerating skeletal muscle de novo.

In order to understand the mechanism of myocyte reprogramming, we utilized a deep sequencing approach to characterize the early transcriptional changes that occur as post-mitotic myocytes reprogram into dedifferentiated myoblasts capable of proliferation. Two parallel strategies, GAGE analysis (KEGG pathways and GO terms) or K-means clustering followed by Panther GO term enrichment analysis, were used to functionally annotate all 6596 DEGsadd. Broadly speaking, both strategies gave similar results, conferring reliability to our analyses. Our

results reveal that myocyte dedifferentiation is marked by downregulation of muscle-specific programs, such as the sarcomeric apparatus and calcium homeostasis. Additionally, both parallel GO term analyses (GAGE and Panther enrichment analysis) revealed a downregulation of terms more broadly related to cellular differentiation and tissue or organ morphogenesis. The downregulation of pyruvate metabolism, oxidative phosphorylation, TCA cycle pathways, pyruvate metabolic processes, proton-transporting ATP synthase complexes, and mitochondrial ATP synthesis reflects a decrease in the need for mitochondrial oxidative capacity in dedifferentiating cells. This is similar to the processes of somatic and oncogenic cellular reprogramming to a pluripotent state in which reprogrammed cells undergo metabolic "rewiring" that reduces both mitochondrial content and oxidative phosphorylation capacity [50–54]. Interestingly, autophagy activation reduces mitochondrial content early in reprogramming [55] and, although our analysis did not find any significant autophagy-specific KEGG pathways or GO terms, we have previously shown that autophagy plays a key role in zebrafish muscle regeneration [48]. The absence of significant autophagy-specific KEGG pathways or GO terms is not surprising since, in this model, autophagy is regulated mainly at the protein level [48]. Notably, we found a consistent upregulation of terms related to lysosomal protein degradation – the last step of the autophagy process – including the lysosome KEGG pathway and the GO terms cysteine-type peptidase activity and lysosome organization.

In addition to the already discussed pathways and terms, enrichment analysis of unbiased k-means clustering expression profiles revealed several interesting GO terms. Enriched GO terms within "G: Late Upregulation" genes included DNA replication, chromosome condensation, and DNA biosynthesis, all of which are consistent with reprogramming cells preparing to reenter the cell cycle. The timing of upregulation within this profile (i.e., 18 hpi) correlates well with our

published results showing that cell proliferation (EdU incorporation into DNA) begins by 20–24 hpi [9]. A recent bioinformatic analysis of zebrafish heart regeneration identified similar changes in energy metabolism, amino-acid biosynthesis and DNA replication linked to the initial proliferative response [56], indicating shared molecular mechanisms between these regenerative processes. The reacquisition of proliferative potential, importantly, represents the most fundamental aspect of the reprogramming process. Supporting this finding, pharmacological inhibition of the cell cycle with either bortozemid or 5-fluorouracil blocks the muscle-tomesenchymal transition that drives EOM regeneration [8].

Terms related to mRNA processing, mRNA transport, and protein translation and modification were enriched in “C: Persistent Upregulation” genes (Figure 2.4 C) which were upregulated at 9 and 18 hpi. Additionally, genes only upregulated at 9 hpi (“F: Transient Upregulation”, Figure 2.4 F) were related to transcription, rRNA maturation, tRNA processing, and epigenetic regulation of transcription. These findings indicate that the cells are preparing to synthesize a new set of proteins that, in conjunction with broad protein degradation, would allow the cell to perform the drastic cellular proteome changes that reprogramming requires [57]. Interestingly, the GO term “fin regeneration,” enriched in “C: Persistent Upregulation” genes (Figure 2.4 C), was upregulated at 9 and 18 hpi, and included hdac1 (histone deacetylase 1) and smarca4a (SWI/SNF related, matrix associated, actin dependent regulator of chromatin, subfamily a, member 4a). These genes, along with GO terms related to epigenetic regulation of transcription, confirm the importance of chromatin-dependent gene expression changes during the reprogramming process.

Based upon functional annotations, we hypothesized that important initiators of dedifferentiation would belong to expression profile “F: Transient Upregulation”, which peak at 9

hpi and return to control levels at 18 hpi, and that morpholino knockdown of these genes would both interfere with cell cycle reentry and impair the anatomic EOM regeneration. Profile "F: Transient Upregulation" candidates were ezh2, encoder of Polycomb group protein that broadly regulate epigenetic states [43]. Although delayed anatomic regeneration following Ezh2 knockdown supported the regulatory importance of profile "F: Transient Upregulation" genes, the true test remained the ability to affect cell cycle reentry within dedifferentiated myoblasts. Knockdowns of Ezh2 reduced the proportion of proliferating myoblasts, thus bolstering the importance of these and other dynamically expressed profile "F: Transient Upregulation" genes as "switch"-like regulators of EOM dedifferentiation leading to regeneration. In line with our results, mammalian EZH2 promotes proliferation by modifying chromatin conformation in models of pancreas [58], liver [59], and dental pulp regeneration [60]. Importantly, knockdown of the Ezh2 Polycomb partner Suz12a replicated Ezh2 knockdown results, thus confirming the relevance of epigenetic regulation in myocyte reprogramming. In addition to the discussed role in promoting cell cycle reentry, PCR2 factors may play an additional transient role repressing muscle identity since PRC2 factors maintain the chromatin state of muscle genes in a repressive conformation and must be degraded to allow myogenic differentiation [61].

We further hypothesized that genes with later activation (18 hpi) would affect post-reprogramming processes. Profile "G: Late Upregulation" included the ECM factor fn1a (fibronectin) whose knockdown, unlike those in profile "F: Transient Upregulation", resulted in a robust defect in anatomic regeneration with no effect on proliferation. Our results are supported by reports showing that fn1a was required for zebrafish heart regeneration but not for cardiomyocyte dedifferentiation and subsequent proliferation [62]. It was also found to be upregulated in microarray analyses of zebrafish heart [56,63] and fin [64] regeneration, validating

this transcriptomic assessment and suggesting the existence of common features among tissue regeneration models. Interestingly, fn1a was also identified in a correlation of fin regeneration genes with melanoma markers [65], highlighting again the similarities between regeneration and cancer. The data supports the hypothesis that while the regeneration process may take days, the transcriptional template for the entire process is determined at the outset of the regeneration process: early activated genes regulate initial reprogramming events, while late response genes regulate tissue growth. These findings reveal the temporal relationship that correlates transcriptional regulation with biological function.

2.5 Conclusion

We describe a transcriptome analysis of an in vivo dedifferentiation process during which myocytes reprogram to become myoblasts that regain the capacity to proliferate. Our analysis reveals a complex and coordinated process (Figure 2.7) that begins with downregulated expression of genes that confer muscle identity, significant changes in metabolic programs, coordinated activation of protein degradation that clears the sarcomere and other muscle-specific protein complexes, and the synthesis of new proteins that reshape the proteomic cellular profile. Simultaneously, activation of programs related to DNA replication, repair, and chromosome condensation, as well as of genes required for the G-to-S transition, ultimately leads to cell cycle reentry by reprogrammed myocytes and the formation of dedifferentiated myoblasts. The early and temporally regulated activation of genes related to epigenetic regulation of transcription likely drives the broad programmatic genomic changes required for myocyte dedifferentiation. We propose a mechanistic overview of the temporal orchestration of pathways involved in cellular reprogramming. We also assess the importance of early-activated chromatin remodeling factors

(Ezh2 and Suz12a) during the dedifferentiation and cell cycle reentry of “post-mitotic” myocytes. On the other hand, late activated genes, like fn1a (encoding an extracellular matrix interacting protein), would regulate the anatomic growth of regenerating muscle tissue following cellular reprogramming.

Understanding the molecular mechanism of cellular reprogramming that leads to lineage-restricted proliferating progenitor cells carries particular importance to the field of de novo tissue regeneration. Furthermore, the similarities between tissue regeneration and cancer (for example, cell reprogramming and dedifferentiation, proliferation and migration) may suggest a similar relationship between genes that control “stemness” and those that regulate metastasis. Future research will aim to uncover greater details of these similarities and relationships.

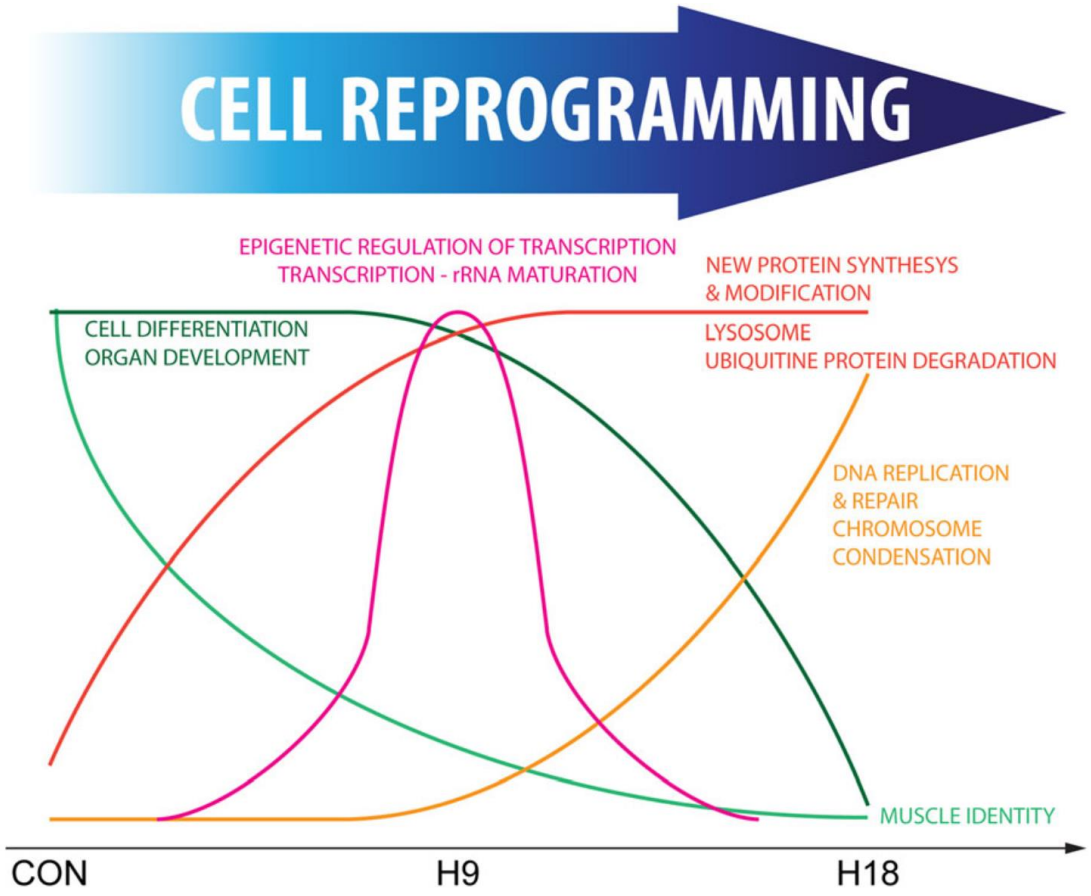

Figure 2.7: Proposed coordinated process of myocyte reprogramming
Reprogramming "post-mitotic" myocytes into dedifferentiated myoblasts would require a complex, temporally sensitive, orchestration of genes and pathways involved in the regulation of chromatin modifications, protein degradation, RNA processing, and DNA and protein synthesis

2.6 References

1. Garg K, Ward CL, Hurtgen BJ, Wilken JM, Stinner DJ, Wenke JC, et al. Volumetric muscle loss: Persistent functional deficits beyond frank loss of tissue. J Orthop Res 2015;33:40–6. doi:10.1002/jor.22730.
2. Corona BT, Rivera JC, Owens JG, Wenke JC, Rathbone CR. Volumetric muscle loss leads to permanent disability following extremity trauma. J Rehabil Res Dev 2015;52:785–92.
3. Rowlerson A, Radaelli G, Mascarello F, Veggetti A. Regeneration of skeletal muscle in two teleost fish: Sparus aurata and Brachydanio rerio. Cell Tissue Res 1997;289:311–22. doi:10.1007/s004410050878.
4. Poss KD, Wilson LG, Keating MT. Heart regeneration in zebrafish. Science (80-) 2002;298:2188–90. doi:10.1126/science.1077857.
5. Sandoval-Guzman T, Wang H, Khattak S, Schuez M, Roensch K, Nacu E, et al. Fundamental differences in dedifferentiation and stem cell recruitment during skeletal muscle regeneration in two salamander species. Cell Stem Cell 2014;14:174–87.
6. Mauro A. Satellite cell of skeletal muscle fibers. J Biophys Biochem Cytol 1961;9:493–5. doi:10.1083/jcb.9.2.493.
7. Moss FP, Leblond CP. Satellite cells as the source of nuclei in muscles of growing rats. Anat Rec 1971;170:421–35.
8. Jopling C, Sleep E, Raya M, Martí M, Raya A, Belmonte JCI. Zebrafish heart regeneration occurs by cardiomyocyte dedifferentiation and proliferation. Nature 2010;464:606–9. doi:10.1038/nature08899.
9. Saera-Vila A, Kasprick DS, Junttila TL, Grzegorski SJ, Louie KW, Chiari EF, et al. Myocyte Dedifferentiation Drives Extraocular Muscle Regeneration in Adult Zebrafish. Invest Ophthalmol Vis Sci 2015;56:4977–93. doi:10.1167/iovs.14-16103.
10. Brockes JP. Amphibian limb regeneration: rebuilding a complex structure. Science (80-) 1997;276:81–7.
11. Sousa S, Afonso N, Bensimon-Brito A, Fonseca M, Simoes M, Leon J, et al. Differentiated skeletal cells contribute to blastema formation during zebrafish fin regeneration. Development 2011;138:3897–905.
12. Hitchcock PF, Raymond PA. Retinal regeneration. Trends Neurosci 1992;15:103–8.
13. Knopf F, Hammond C, Chekuru A, Kurth T, Hans S, Weber CW, et al. Bone regenerates via dedifferentiation of osteoblasts in the zebrafish fin. Dev Cell 2011;20:713–24.
14. Singh SP, Holdway JE, Poss KD. Regeneration of Amputated Zebrafish Fin Rays from De Novo Osteoblasts. Dev Cell 2012;22:879–86. doi:10.1016/j.devcel.2012.03.006.
15. Choi TY, Ninov N, Stainier DY, Shin D. Extensive conversion of hepatic biliary epithelial cells to hepatocytes after near total loss of hepatocytes in zebrafish. Gastroenterology 2012;146:776–88.
16. Xu X, Wilschut KJ, Kouklis G, Tian H, Hesse R, Garland C, et al. Human Satellite Cell Transplantation and Regeneration from Diverse Skeletal Muscles. Stem Cell Reports 2015;5:419–34. doi:10.1016/j.stemcr.2015.07.016.
17. Pajcini K V, Corbel SY, Sage J, Pomerantz JH, Blau HM. Transient inactivation of Rb and ARF yields regenerative cells from postmitotic mammalian muscle. Cell Stem Cell

2010;7:198–213.
18. Hesse RG, Kouklis GK, Ahituv N, Pomerantz JH. The human ARF tumor suppressor senses blastema activity and suppresses epimorphic tissue regeneration. Elife 2015;4:1–23. doi:10.7554/eLife.07702.
19. Belluoccio D, Rowley L, Little CB, Bateman JF. Maintaining mRNA integrity during decalcification of mineralized tissues. PLoS One 2013;8:e58154.
20. Langmead B, Trapnell C, Pop M, Salzberg S. Ultrafast and memory-efficient alignment of short DNA sequences to the human genome. Genome Biol 2009;10:R25. doi:10.1186/gb-2009-10-3-r25.
21. Trapnell C, Pachter L, Salzberg SL. TopHat: Discovering splice junctions with RNA-Seq. Bioinformatics 2009;25:1105–11. doi:10.1093/bioinformatics/btp120.
22. Trapnell C, Hendrickson DG, Sauvageau M, Goff L, Rinn JL, Pachter L. Differential analysis of gene regulation at transcript resolution with RNA-seq. Nat Biotechnol 2013;31:46–53.
23. Hu P, Liu M, Zhang D, Wang J, Niu H, Liu Y, et al. Global identification of the genetic networks and cis-regulatory elements of the cold response in zebrafish. Nucleic Acids Res 2015;43:9198–213. doi:10.1093/nar/gkv780.
24. Trapnell C, Roberts A, Goff L, Pertea G, Kim D, Kelley DR, et al. Differential gene and transcript expression analysis of RNA-seq experiments with TopHat and Cufflinks. Nat Protoc 2012;7:562–78. doi:10.1038/nprot.2012.016.
25. Luo W, Friedman MS, Shedden K, Hankenson KD, Woolf PJ. GAGE: generally applicable gene set enrichment for pathway analysis. BMC Bioinformatics 2009;10:161. doi:10.1186/1471-2105-10-161.
26. Luo W, Friedman MS, Hankenson KD, Woolf PJ. Time series gene expression profiling and temporal regulatory pathway analysis of BMP6 induced osteoblast differentiation and mineralization. BMC Syst Biol 2011;5:82. doi:10.1186/1752-0509-5-82.
27. Luo W, Brouwer C. Pathview: an R/Bioconductor package for pathway-based data integration and visualization. Bioinformatics 2013;29:1830–1.
28. Zhang JD, Wiemann S. KEGGgraph: a graph approach to KEGG PATHWAY in R and bioconductor. Bioinformatics 2009;25:1470–1.
29. Mi HY, Muruganujan A, Casagrande JT, Thomas PD. Large-scale gene function analysis with the PANTHER classification system. Nat Protoc 2013;8:1551–66.
30. Mi HY, Poudel S, Muruganujan A, Casagrande JT, PDPANTHER T. Version 10: expanded protein families and functions, and analysis tools. Nucleic Acids Res 2016;44:D336–D4.
31. Thummel R, Bai S, Sarras MP, Song P, McDermott J, Brewer J, et al. Inhibition of zebrafish fin regeneration using in vivo electroporation of morpholinos against fgfr1 and msxb. Dev Dyn 2006;235:336–46. doi:10.1002/dvdy.20630.
32. Craig SEL, Thummel R, Ahmed H, Vasta GR, Hyde DR, Hitchcock PF. The zebrafish galectin drgal1-L2 is expressed by proliferating m??ller glia and photoreceptor progenitors and regulates the regeneration of rod photoreceptors. Investig Ophthalmol Vis Sci 2010;51:3244–52. doi:10.1167/iovs.09-4879.
33. Ramachandran R, Fausett B V, Goldman D. Ascl1a regulates Muller glia dedifferentiation and retinal regeneration through a Lin-28-dependent, let-7 microRNA signalling pathway. Nat Cell Biol 2010;12:1101–7.
34. Huang HT, Kathrein KL, Barton A, Gitlin Z, Huang YH, Ward TP, et al. A network of

epigenetic regulators guides developmental haematopoiesis in vivo. Nat Cell Biol 2013;15:1516–25.
35. Trinh LA, Stainier DY. Fibronectin regulates epithelial organization during myocardial migration in zebrafish. Dev Cell 2004;6:371–82.
36. Eckfeldt CE, Mendenhall EM, Flynn CM, Wang TF, Pickart MA, Grindle SM, et al. Functional analysis of human hematopoietic stem cell gene expression using zebrafish. PLoS Biol 2005;3:e254.
37. Eisen JS, Smith JC. Controlling morpholino experiments: don't stop making antisense. Development 2008;135:1735–43. doi:10.1242/dev.001115.
38. Salic A, Mitchison TJ. A chemical method for fast and sensitive detection of DNA synthesis in vivo. Proc Natl Acad Sci U S A 2008;105:2415–20. doi:10.1073/pnas.0712168105.
39. Bryant DM, Johnson K, DiTommaso T, Tickle T, Couger MB, Payzin-Dogru D, et al. A tissue-mapped axolotl de novo transcriptome enables identification of limb regeneration factors. Cell Rep 2017;18:762–76.
40. Edwards-Faret G, Munoz R, Mendez-Olivos EE, Lee-Liu D, Tapia VS, Larrain J. Spinal cord regeneration in Xenopus Laevis. Nat Protoc 2017;12:372–89.
41. Luz-Madrigal A, Rio-Tsonis G-EED, K. Electroporation of embryonic Chick eyes. Bio Protoc 2015;5.
42. Karunakaran DK, Kanadia R. Vivo and explant electroporation of Morpholinos in the developing mouse retina. Methods Mol Biol 2017;1565:215–27.
43. Schuettengruber B, Cavalli G. Recruitment of polycomb group complexes and their role in the dynamic regulation of cell fate choice. Development 2009;136:3531–42.
44. Lamouille S, Xu J, Derynck R. Molecular mechanisms of epithelialmesenchymal transition. Nat Rev Mol Cell Biol n.d.;15:178–96.
45. Geurtzen K, Knopf F, Wehner D, Huitema LF a, Schulte-Merker S, Weidinger G. Mature osteoblasts dedifferentiate in response to traumatic bone injury in the zebrafish fin and skull. Development 2014;141:2225–34. doi:10.1242/dev.105817.
46. Jopling C, Boue S, Izpisua Belmonte JC. Dedifferentiation, transdifferentiation and reprogramming: three routes to regeneration. Nat Rev Mol Cell Biol 2011;12:79–89.
47. Semi K, Matsuda Y, Ohnishi K, Yamada Y. Cellular reprogramming and cancer development. Int J Cancer 2013;132:1240–8.
48. Saera-Vila A, Kish PE, Louie KW, Grzegorski SJ, Klionsky DJ, Kahana A. Autophagy Regulates Cytoplasmic Remodeling During Cell Reprogramming in a Zebrafish Model of Muscle Regeneration. Autophagy 2016;8627:00–00. doi:10.1080/15548627.2016.1207015.
49. Saera-Vila A, Kish PE, Kahana A. Fgf regulates dedifferentiation during skeletal muscle regeneration in adult zebrafish. Cell Signal 2016;28:1196–204.
50. Folmes CD, Nelson TJ, Martinez-Fernandez A, Arrell DK, Lindor JZ, Dzeja PP, et al. Somatic oxidative bioenergetics transitions into pluripotency-dependent glycolysis to facilitate nuclear reprogramming.Cell Metab 2011;14:264–71.
51. Panopoulos AD, Yanes O, Ruiz S, Kida YS, Diep D, Tautenhahn R, et al. The metabolome of induced pluripotent stem cells reveals metabolic changes occurring in somatic cell reprogramming. Cell Res 2012;22:168–77.
52. Xu X, Duan S, Yi F, Ocampo A, Liu GH, Izpisua Belmonte JC. Mitochondrial regulation in pluripotent stem cells. Cell Metab 2013;18:325–32.

53. Rossignol R, Gilkerson R, Aggeler R, Yamagata K, Remington SJ, Capaldi RA. Energy substrate modulates mitochondrial structure and oxidative capacity in cancer cells. Cancer Res 2004;64:985–93.
54. Ye XQ, Li Q, Wang GH, Sun FF, Huang GJ, Bian XW, et al. Mitochondrial and energy metabolism-related properties as novel indicators of lung cancer stem cells. Int J Cancer 2011;129:820–31.
55. Wang S, Xia P, Ye B, Huang G, Liu J, Fan Z. Transient activation of autophagy via Sox2-mediated suppression of mTOR is an important early step in reprogramming to pluripotency. Cell Stem Cell 2013;13:617–25.
56. Rodius S, Androsova G, Gotz L, Liechti R, Crespo I, Merz S, et al. Analysis of the dynamic coexpression network of heart regeneration in the zebrafish. Sci Rep 2016;6.
57. Mizushima N, Klionsky DJ. Protein turnover via autophagy: implications for metabolism. Annu Rev Nutr 2007;27:19–40.
58. Mallen-St. Clair J, Soydaner-Azeloglu R, Lee KE, Taylor L, Livanos A, Pylayeva-Gupta Y, et al. EZH2 couples pancreatic regeneration to neoplastic progression. Genes Dev 2012;26:439–44. doi:10.1101/gad.181800.111.
59. Bae WK, Kang K, JH Y, Yoo KH, Factor VM, Kaji K, et al. The methyltransferases enhancer of zeste homolog (EZH) 1 and EZH2 control hepatocyte homeostasis and regeneration. FASEB J 2015;29:1653–62.
60. Hui T, P A, Zhao Y, Wang C, Gao B, Zhang P, et al. EZH2, a potential regulator of dental pulp inflammation and regeneration. J Endod 2014;40:1132–8.
61. Consalvi S, Brancaccio A, Dall'Agnese A, Puri PL, Palacios D. Praja1 E3 ubiquitin ligase promotes skeletal myogenesis through degradation of EZH2 upon p38alpha activation. Nat Commun 2017;8.
62. Wang J, Karra R, Dickson AL, Poss KD. Fibronectin is deposited by injuryactivated epicardial cells and is necessary for zebrafish heart regeneration. Dev Biol 2013;382:427–35.
63. Lien CL, Schebesta M, Makino S, Weber GJ, Keating MT. Gene expression analysis of zebrafish heart regeneration. PLoS Biol 2006;4:e260.
64. Schebesta M, Lien CL, Engel FB, Keating MT. Transcriptional profiling of caudal fin regeneration in zebrafish. Sci World J 2006;6:38–54.
65. Hagedorn M, Siegfried G, Hooks KB, Khatib AM. Integration of zebrafish fin regeneration genes with expression data of human tumors in silico uncovers potential novel melanoma markers. Oncotarget 2016.

Chapter 3: Role of *twist3* in Craniofacial Muscle Regeneration[3]

3.1 Introduction

Skeletal muscle injuries and degenerative conditions are common, debilitating, and significant causes of morbidity and mortality worldwide [1, 2]. Despite the pervasiveness of injury, mammalian muscle repair is limited by the extent of tissue damage and restricted by the amount of resident stem cells (*i.e.* satellite cells) available for tissue replacement [3]. This differs from non-mammalian vertebrates such as zebrafish which robustly regenerate both skeletal and cardiac muscle as well as other tissues including retina, spinal cord, liver, and fin [4-8]. Such extensive repair, or rather whole tissue regeneration, relies less on the activation of resident stem cells and more on cell reprogramming and dedifferentiation [9, 10]. Understanding the mechanisms underlying adult *de novo* muscle regeneration in model vertebrates thus represents a topic with widespread clinical therapeutic implications [2, 11]. Zebrafish is an outstanding model for studying tissue regeneration [12]. Our lab has developed a novel zebrafish-based system to study regeneration of extraocular muscles (EOMs) - a form of skeletal muscle whose regeneration is driven by myocyte dedifferentiation with no significant contribution from satellite cells [10].

The twist family of basic helix-loop-helix (bHLH) transcription factors (TFs) represent an evolutionarily conserved family of proteins that regulate stem cells during both embryonic development [13-15] and adult progenitor cell maintenance [16]. Twist orthologs are also known

[3] Published as Zhao Y, Louie KW, Tingle CF, Sha C, Heisel CJ, Unsworth SP, Kish PE, Kahana A. 2020. *Twist3* is required for dedifferentiation during extraocular muscle regeneration in adult zebrafish. *PLoS ONE* 15(4): e0231963. https://doi.org/10.1371/journal.pone.0231963

regulators of muscle formation and regeneration in *Drosophila* [17, 18], muscle stem cells during mouse development [19], and skeletal muscle repair in adult mice [20, 21]. Zebrafish have 4 twist homologs - twist1a, twist1b, twist2, and twist3 - which are orthologs of mammalian twist1 and twist2 [22] and are necessary for proper craniofacial development [23]. The prevailing belief that regeneration is a recapitulation of embryonic development led us to hypothesize that twist TFs are involved in adult extraocular muscle (EOM) regeneration. We therefore sought to identify which zebrafish twist homologs participate in the regeneration process and at what timepoint.

Utilizing our established regeneration model, we report that twist3 is the sole twist TF required for EOM regeneration in adult zebrafish. Knockdown of twist3 significantly impairs muscle regeneration by decreasing myofiber dedifferentiation and cell proliferation post-injury. These findings suggest that twist3 plays an early role during the myocyte dedifferentiation process that precedes cell cycle re-entry. Additionally, knockdown of other zebrafish twist homologs (*i.e.* twist1a, twist1b, and twist2) did not affect regeneration parameters, thereby suggesting fundamental differences between embryonic development and adult muscle regeneration in zebrafish.

3.2 Materials and Methods

3.2.1 Zebrafish (*Danio rerio*) Rearing and Surgeries

All animal work was performed in compliance with the ARVO Statement for the Use of Animals in Ophthalmic and Vision Research and approved by the University of Michigan Committee on the Use and Care of Animals, protocol 06034. Sexually mature adult (4–18 month-old) zebrafish were spawned in our fish facility and raised per standard protocol [24] at 28 °C with a 14-h light/10-h dark alternating cycle.

Adult zebrafish were anesthetized using 0.05% tricaine methanosulfate (Tricaine-S; Western Chemical, Ferndale, WA) with 0.05% sodium bicarbonate buffer and about 50% of the lateral rectus (LR) muscle was surgically excised, i.e. myectomy. The length of the regenerating muscle was quantified by craniectomy as described previously [25]. Regeneration is represented as the relative size of the injured LR muscle normalized to the length of the uninjured LR muscle (representing 100%). All experiments were performed using 5 fish per experimental group and/or time point, unless stated otherwise in the text and/or figure legend.

3.2.2 Twist TFs Customized Antibody

Polyclonal rabbit antibodies to twist proteins (twist1a, twist1b, twist2, and twist3) were custom produced by Hitag Biotechnology, Lda, Cantanhede Portugal. Briefly, codon optimized 6x-His tagged proteins were expressed in bacteria, the protein was purified using multiple steps and the His-tag removed with tobacco etch virus (TEV) protease. Rabbits were immunized with the purified proteins and the resulting sera purified by Protein A affinity chromatography. Twist 3 antibodies were further affinity purified using His-tagged zebrafish twist3 over-expressed protein (expressed in HEK293 cells) and affinity purified using cobalt-IMAC chromatography. The purified tagged twist 3 protein was coupled to a MicroLink™ Protein Coupling Kit column (Pierce, Rockford, IL) and the antibodies purified according to the manufacturer's instructions. Antibodies were validated for Western blot specificity utilizing mammalian over-expression plasmids transiently transfected into HEK293 cells with Lipofectamine 2000 (Invitrogen, Carlsbad CA).

3.2.3 Protein Extraction, Immunoprecipitation, and Western Blots

For embryo protein extraction, dechorionated and deyolked zebrafish embryos were pooled and homogenized in RIPA lysis buffer (Cell Signaling Technology, Danvers, MA) in a ratio of

100 µL RIPA/30 embryos. For adult LR muscle protein extraction, transgenic Tg(α-actin::EGFP) fish were used to visualize the muscles. Muscle tissue were collected as previously described [26]. Injured or uninjured LR were pooled in denaturing buffer (1% SDA, 5mM EDTA, 10mM beta-mercaptoethanol, Protease inhibitors, 15 U/ml DNase1) in a ratio of 30 muscle/100 µL buffer and homogenized by passing lysis through a 27-gauge needle attached to a 1 mL syringe. Heat samples to 95 °C for 5 min to denature and centrifuge to collect supernatant. Protein concentrations were determined by BCA assay (Thermo Scientific, 23227).

Same amount of protein (~100 uL) were diluted by non-denaturing buffer (20 mM Tris HCl, 137 mM NaCl, 10% glyceral, 1% NP-40, 2mM EDTA) to make a total volume of 1mL and proceed with the immunoprecipitation.

Protein samples were incubated with customized twist antibodies 1:100 at 4°C with continuous mixing overnight. The following day, 200 µL washed PureProteome™ Protein A Magnetic Beads (Cat. No. LSKMAGA02, Lot 2674904A, Germany) were added per 1 mL of sample, and this was allowed to incubate for 45-60 minutes at 4°C with continuous mixing. The supernatant was removed, and the beads were washed 3x5min with 0.1% PBS-Tween20. After the last wash, the buffer was removed, and Laemmli Sample buffer was added proportional to number of muscles collected. This was boiled at 90°C for 10 minutes before removing the solution for use in Western blots.

Anti-Tubg1 (1:1000, Sigma, T5326), anti-beta actin (1:30,000, Santa Cruz, sc-47778 HRP), anti-p-histone H3 (1:1000, Cell Signaling Technology, 9701), and customized twist TFs antibodies were used to detect protein.

3.2.4 Drug Treatments

SU5402 (Selleckchem, Houston, TX) was dissolved in DMSO as a 17 mM stock and added to fish water at a final concentration of 17 μM as described [27], tanks were kept in the dark. Up to 5 fish were treated in 250 mL of water, tanks were maintained at 28.5°C, and drug solutions were replaced every 24 h. Drug treatments were performed 24 h before surgery and no significant mortality was noted.

3.2.5 Morpholino Oligonucleotide Injection and Electroporation

Microinjection of morpholino oligonucleotides (MOs; Gene-Tools, LLC, Philomath, OR) - a widely used technique to perform knockdown experiments in zebrafish [29–31] - was used. To knockdown genes in adult EOMs, lissamine-tagged MOs were directly microinjected into the right LR muscle of Tg(α-actin::EGFP) adult fish, followed by square-wave electroporation (6 to 10 pulses at 48 V/cm, BTX ECM830 electroporator; Harvard Apparatus, Holliston, MA). Microinjections were performed 4 h prior to LR injury, and MO uptake was confirmed via lissamine fluorescence prior to myectomy. No mortality was detected during the experimental process. MO sequences are listed in Table 1; a standard control MO targeting a mutated splice site of human β-globin mRNA was injected for each experiment as negative control.

Table 3.1: Sequences for Morpholino Oligonucleotides

Name	Sequence
Standard control	5’-CCTCTTACCTCAGTTACAATTTATA-3’
***Twist1a*-MO**	5’-GTGCATCGCCTCTTCCTCAAACATC-3’
***Twist1b*-MO**	5’-CGGGCTCTTCGGGCATCTCGCTTAA-3’
***Twist2*-MO**	5’-AATACGATCTCCACTTTTGGTTCCG-3’
***Twist3*-MO**	5’-TCCACAAGTCTGTTCCTCTCGCATG-3’

3.2.6 EdU Incorporation Assay

Cellular proliferation was assessed by intra-peritoneal (IP) injections of 5-ethynyl-2’-deoxyuridine (EdU) and standard detection methods [10]. Fish were anesthetized and injected with EdU (20 μL, 10 mM EdU in PBS) at 20 hpi or 44 hpi and sacrificed 4 h later (24 hpi or 48 hpi). For each experiment, 3 fish per group were analyzed. The injured muscle of each fish was analyzed with both EdU-positive and total (DAPI-positive) nuclei counted from 3 nonconsecutive sections per muscle. Representative sections had approximately 1800 total nuclei (range 812–3016) per muscle. Cell proliferation is represented as the percentage of EdU-positive nuclei in the injured muscle.

3.2.7 Specimen Processing

Zebrafish heads were excised and decalcified using Magic-EDTA (10% EDTA, saturated ammonium sulfate in PBS, Ph7.4) for 3 days. Decalcified tissues were fixed in 4% paraformaldehyde (PFA) overnight at 4°C. Decalcified and fixed tissues were cryoprotecteded with 20% sucrose in PBS, embedded in OCT (Fisher Scientific), frozen, and evaluated microscopically using coronal frozen sections (12 μm) as described previously [10].

3.2.8 Statistics

Comparisons between 2 groups were analyzed by Student t-test (*$p < 0.05$; **$p < 0.01$; ***$p < 0.001$). When more than 2 groups were compared, one-way analysis of variance (ANOVA, $P < 0.05$) followed by Newman-Keuls multiple comparisons test ($p < 0.05$) was performed. Thus, in the time course experiments, differences between fish groups for each time point were analyzed by Student t-test and differences among time points for each fish group were analyzed by ANOVA. All tests were performed using the statistical software Prism 6.03 (GraphPad, LaJolla, CA, USA).

3.3 Results

3.3.1 Inhibition of twist3 Impairs Adult Zebrafish EOM Regeneration

Twist TFs are expressed during zebrafish embryogenesis and regulate craniofacial skeletal development [23, 28]. They are also known to be master regulators of stem cells [29, 30]. Given the need to generate dedifferentiated myoblasts in order to regenerate EOMs, we hypothesized that knock-down of Twist TFs would impair EOM regeneration. Translation blocking MOs significantly decreased protein levels of all Twist TF proteins in embryos (twist1a/b and twist2) and adult EOM (twist3) (Figure 3.1 H-K). To test the effect of twist TF knockdown on EOM regeneration, we performed MO injections and electroporation 4 hours prior to myectomy of the right LR muscle. At 8 days post injury (dpi), control MO injected muscles were fully regrown as expected (Figure 3.1 A-A") [10]. The twist1a, twist1b, and twist2 MO injection groups also displayed full regeneration at 8 dpi (Figure 3.1 B-D"). In contrast, twist3 injected muscles at 8 dpi were significantly shorter than other groups (Figure 3.1 E-E", F).

To determine if this effect was inhibition or just delay of regeneration, we observed the twist3 MO injected group at 21 dpi, approximately three times longer than the typical regeneration time for zebrafish LR post myectomy [10]. At 21 dpi, the length of the regenerated muscle in the

twist3 knockdown group remained significantly shorter than the control group (Figure 3.1 G), suggesting true inhibition of regeneration. Co-injection of twist1a/b, twist2, and twist3 MOs did not enhance this phenotype, suggesting that only twist3 is required for complete LR regeneration.

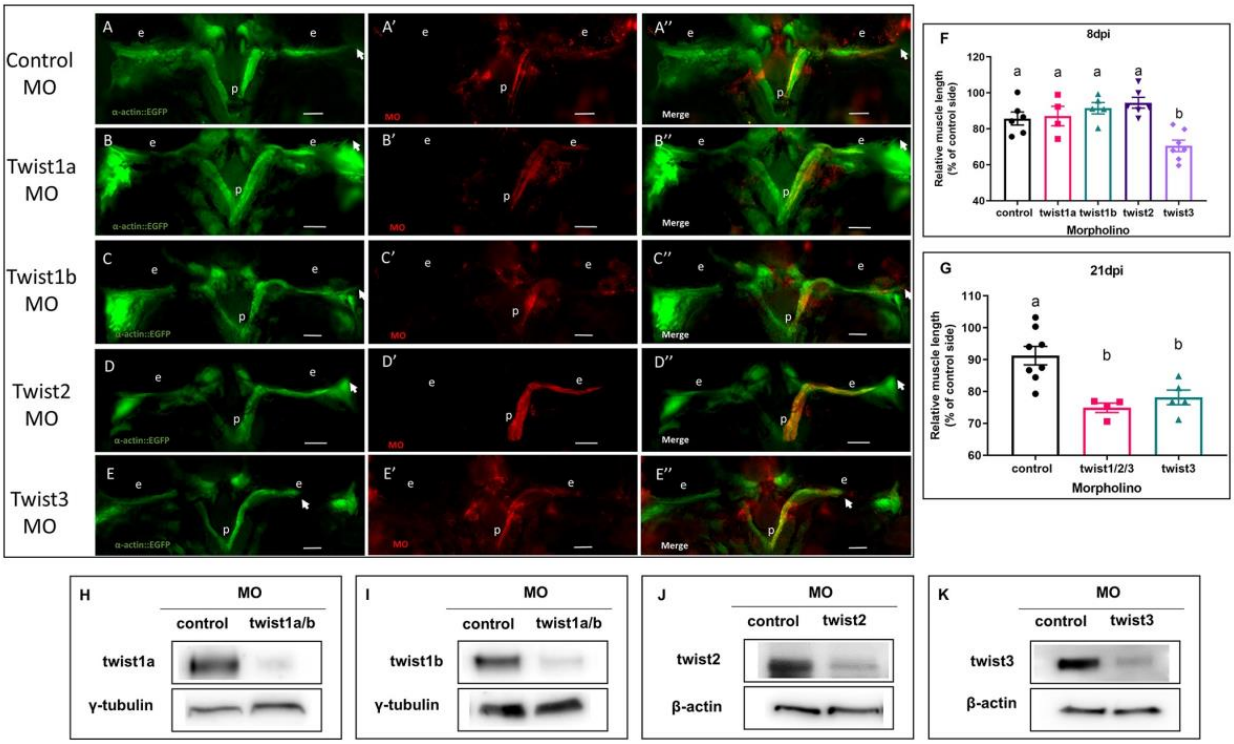

Figure 3.1: Inhibition of Twist3, but not other Twist TFs, impairs muscle regeneration. To knock down Twist TFs, lissamine-tagged MOs (red) against twist 1a, 1b, 2, and 3 were microinjected into Tg(*α-actin::EGFP*) (green) fish muscles 4 h prior to myectomy. (A-E") MO injected fish were shown. (H-J) Knockdown effect of twist 1a/b, and twist2 MO was validated in embryos by Western blot. (K) Knockdown effect of twist3 MO was validated in EOM by Western blot. (F) The length of regenerating muscle was measured as described; values are averages ±SEM (one-way ANOVA, $p<0.05$ between group a and b, control:n=6, twist1a: n=4, twist1b: n=5, twist2: n=6, twist3: n=7). (G) Twist3 MO inhibits but does not delay EOM regeneration; mixture of all 4 Twist TFs MOs or single control and twist3 MO were microinjected into α-actin-EGFP fish muscles 4 h prior to myectomy. The length of regenerating muscle was measured as described; values are averages ±SEM (one-way ANOVA, $p<0.05$ between group a and b, control: n=8, twist1/2/3: n=4, twist3: n=5). White arrows marked the growing end of the regenerating muscle. p, pituitary; e, eye; scale bar: 250μm.

3.3.2 Electroporation of EOMs Alone Does Not Stimulate Proliferation

Electroporation of MOs to modify protein expression has been widely utilized in both *in vitro* and *in vivo* studies in multiple tissues [31-35]. Skeletal muscle is a favored target tissue for this technique and electroporation significantly improves the transgene efficiency [35]. However, there remains concern about muscle damage and subsequent repair associated with electroporation process [35, 36]. In order to exclude electroporation-induced damage and cellular reprogramming as a confounding variable, we assessed levels of proliferation between either electroporation or myectomy alone or in combination. We found that electroporation alone did not significantly induce cell proliferation; only ~2.5% of total myocytes were proliferating cells (EdU-positive vs DAPI-positive; Figure 3.2). In contrast, both cut muscle (*i.e.* injury only) combined treatment muscle (*i.e.* cut and electroporated) showed 3 times greater induction of cell proliferation compared to electroporation alone (~7.5%; Figure 3.2). We therefore concluded that, although electroporation does cause muscle damage and induce cellular proliferation, its extent is insignificant compared to our standard injury procedure (*i.e.* 50% myectomy of the lateral rectus) and does not confound the results of this study.

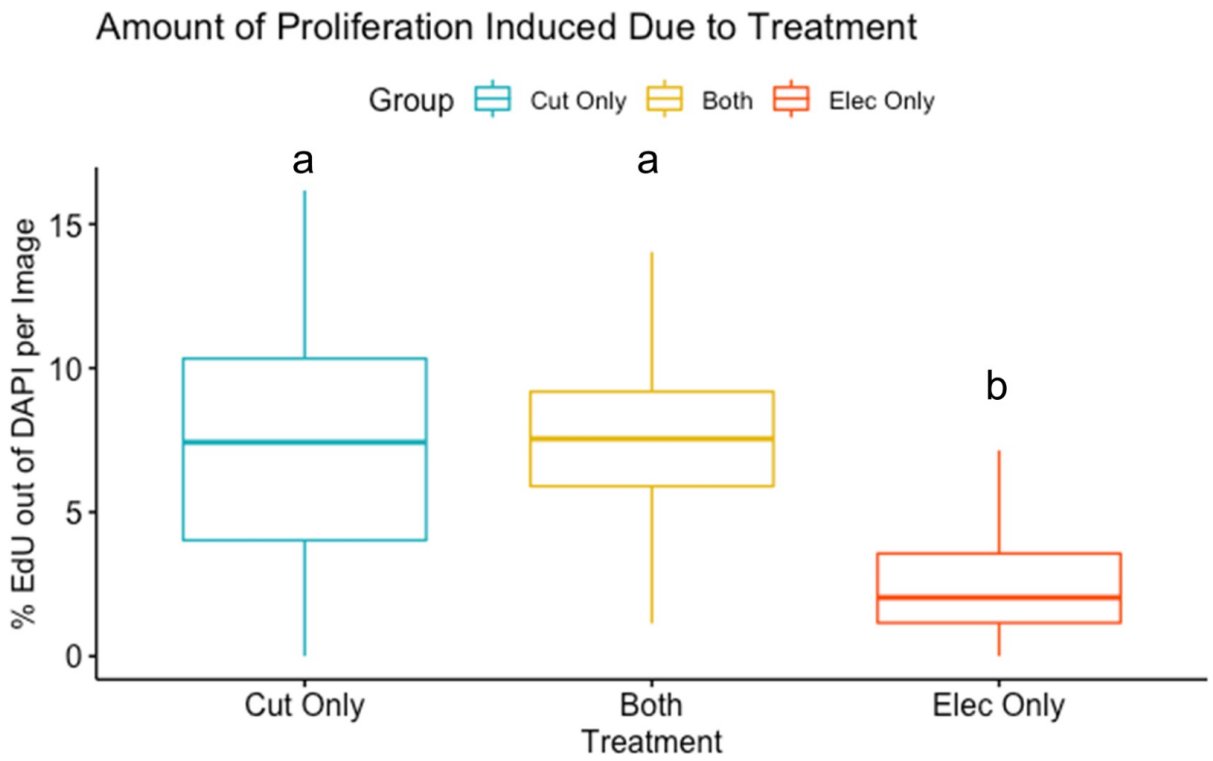

Figure 3.2: Electroporation does not cause significant damage of EOM.
Boxplot of the percentage of proliferating nuclei (EdU) out of all nuclei (DAPI), in three different treatment groups: cut only (blue), both cut and electroporation (yellow), and electroporation only (red). The boxplot displays the minimum, 25th percentile, median, 75th percentile, and maximum for the groups. $p<0.001$ between two statistic groups a and b by ANOVA.

3.3.3 Inhibition of twist3 Reduces Cell Proliferation During Muscle Regeneration

Adult zebrafish EOM regeneration requires myocyte dedifferentiation, followed by a proliferative burst at 24-48 hpi [10]. After generating a sufficient number of myoblasts, cells then migrate, re-differentiate into myocytes and fuse into myotubes [10]. Based on the observed inhibition of regeneration in twist3 MO-injected fish, and the known roles of Twist TFs in stem cell biology, we hypothesized that twist3 would be important in early dedifferentiation steps leading to proliferation.

First, we determined the timing of twist3 gene expression level by Western blot and found a 1.5-fold induction of twist3 as early as 3 hpi (Figure 3.3 I, J). Next, we utilized an EdU incorporation assay to test the number of proliferating myoblasts post-injury, since proliferation

of dedifferentiated myoblasts represents the final step of the reprogramming process [25, 37]. We found that the percentage of proliferating myoblasts (EdU-positive nuclei) in twist3 MO-injected fish was significantly reduced at both 24 and 48 hpi compared to control MO-injected fish (Figure 3.3 B, D, F, H). In contrast, twist3 MO did not inhibit proliferation during embryonic development, since the phosphorylation of histone H3 (proliferation marker) was increased instead of decreased by twist3 MO (Figure 3.6), suggesting that the role of twist3 in EOM myocyte dedifferentiation was not reflective of a general role in cell proliferation. The induction of phosphorylation of histone H3 may due to the delay of development caused by twist3 MO injection (Figure 3.7 D'").

During regeneration of control MO-injected muscles, myofibers in the control group lost Z-band architecture and became mesenchyme-like in appearance at 24 hpi (Figure 3.3 A', A"). It was difficult to distinguish individual myofibers and the morphology became increasingly more mesenchymal at 48 hpi (Figure 3.3 E', E") [10]. In contrast, in twist3 MO-injected muscles, myocytes maintained a differentiated myofiber morphology and Z-band architecture was clearly shown at 24 hpi (Figure 3.3 C', C"). Some myofiber structure remained and Z-bands could be seen in some myofibers at 48 hpi (Figure 3.3 G', G"). Taken together, these data suggest that twist3 plays a role in the control of early myocyte reprogramming and cell cycle reentry after injury.

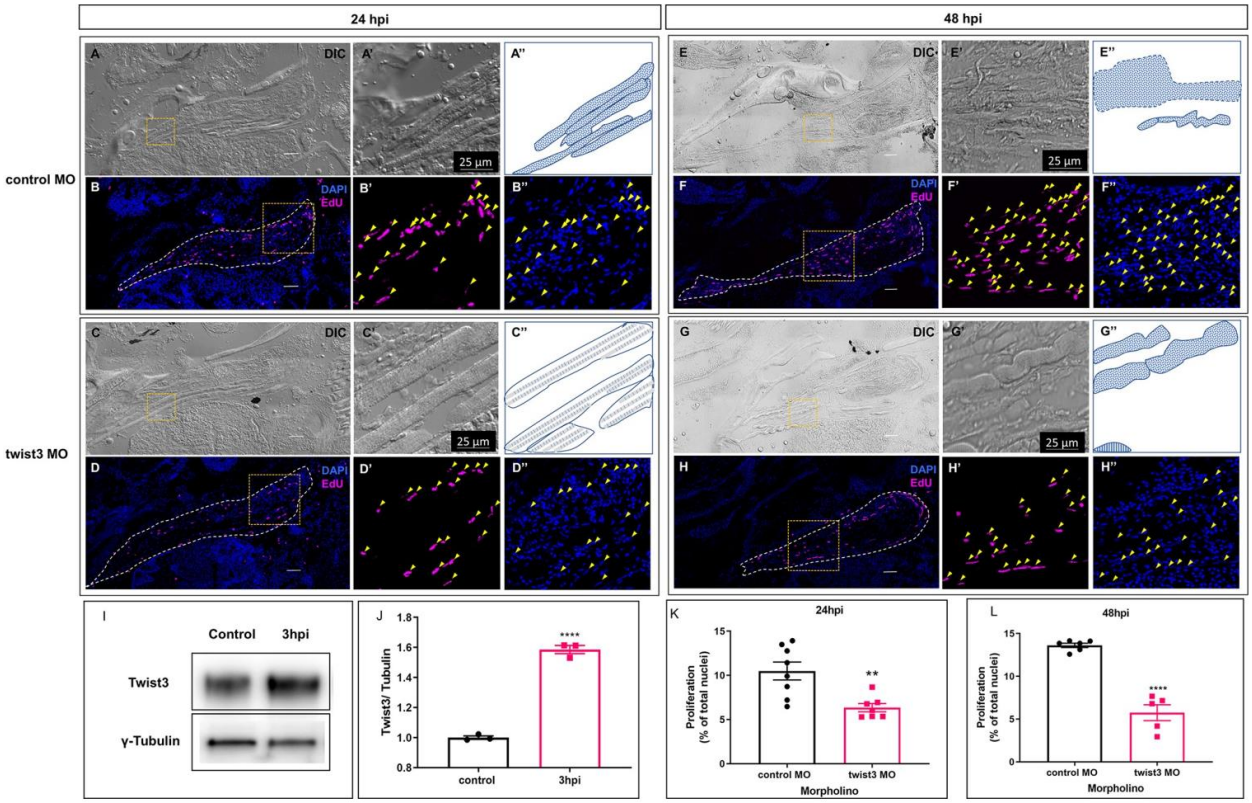

Figure 3.3: Inhibition of Twist3 impairs myocyte reprogramming and proliferation.
The role of Twist3 in myocyte reprogramming and proliferation at 24 and 48 hpi was assessed by injecting Tg(*α-actin::EGFP*) fish with twist3 MO. Morphology of myocytes was shown using DIC images (A, C, E, G),highlighted in higher magnification (A', C', E', G') and illustrated in schematic diagram (A", C", E", G"; solid line: outline of muscle; dash line: approximate outline of muscle; dotted pattern: mesenchyme-like myocytes; long light blue line: myofiber; short vertical strips: Z-band architecture). (B, D, F, H) Proliferating myoblasts were stained by EdU incorporation. EdU: magenta; DAPI: blue; Yellow arrows: positive Edu staining nuclei and corresponding DAPI channel. (I, J) Western blot analysis for Twist3 protein expression during EOM regeneration; values were averages ±SEM (t-test, $p<0.0001$ between control and 3hpi, n=3). (K, L) Cell proliferation in injured muscle was significantly less in Twist3 MO injection group compared with control group at both 24 and 48 hpi. (24 hpi, control: n=8, twist3 MO: n=7; 48 hpi, control: n=6, twist3 MO: n=5) Scale bar: 50 μm, **p<0.01, ****p<0.0001.

3.3.4 Twist3 is Involved in EOM Regeneration Via A Shared Pathway with Fgf

We next investigated the mechanism through which twist3 promotes EOM regeneration. Twist is required for the proper function of the Fgf-signaling pathway [38]. Our previously published study highlighted the important role of Fgf signaling in zebrafish EOM regeneration [25]. Hence, we tested the hypothesis that twist3 promotes regeneration via Fgf signaling. In order

to test this hypothesis, we combined twist3 MO injection with pharmacological inhibition of Fgf using su5402, an Fgf-receptor inhibitor [25]. Both su5402 and twist3 MO injection alone significantly decreased regenerated muscle length as expected (Figure 3.4 D-I). Combining su5402 treatment and twist3 MO injection inhibited regeneration, but no additive/synergistic effect was observed compared to MO injection or su5402 alone (Figure 3.4 J-M) Twist3 protein level was higher in the su5402 group compared with the control group at 3 hpi (Figure 3.4 N), suggesting a negative feedback loop existing between twist3 and Fgf pathways. That is, inhibition of Fgf induced the expression of twist3. In addition, the induction of twist3 could not overcome the effect of Fgf inhibition (Figure 3.4 J-L). Taken together, these data suggest that Fgf is an upstream – but not direct - regulator of twist3, and that Fgf has other downstream targets involved in muscle regeneration in addition of twist3 (Figure 3.5).

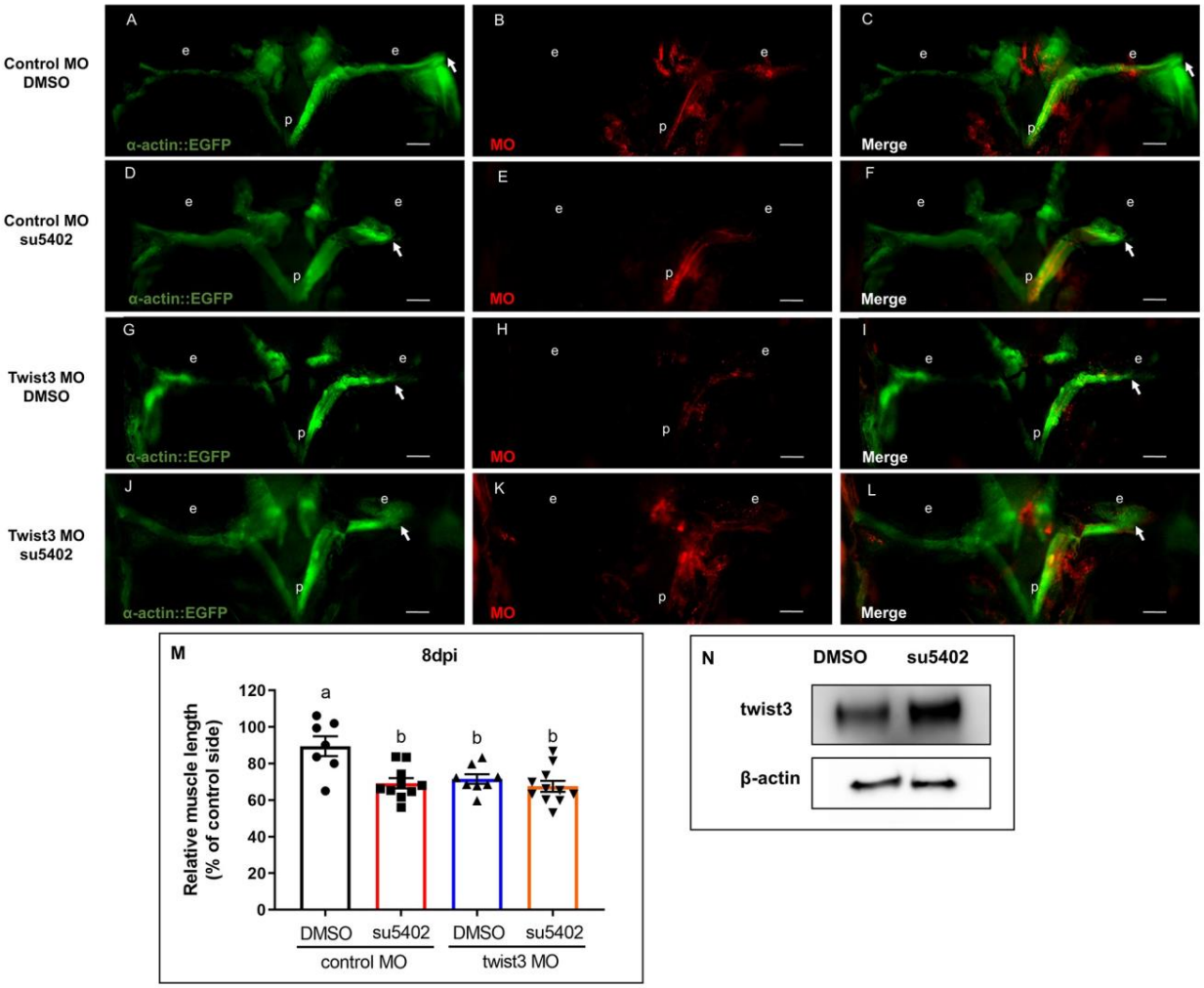

Figure 3.4: Inhibition of Fgfr and twist3 do not have an additive effect on EOM regeneration.

Myectomized Tg(*α-actin::EGFP*) fish were treated with su5402 (D-F), or injected with twist3 MO (G-I), or treated with su5402 and injected with twist3 MO (J-L) compared with DMSO treatment and control MO injection (A-C). (M) All the experiment groups demonstrated significantly inhibited muscle regeneration, with no additive effect detected by combination of two treatments at 8 dpi. (p, pituitary; e, eye; Scale bar: 250μm, $p<0.05$ between two statistic groups a and b by ANOVA, control MO/DMSO: n=7, control MO/su5402: n=10, twist3 MO/DMSO: n=8, twist3 MO/su5402: n=11)

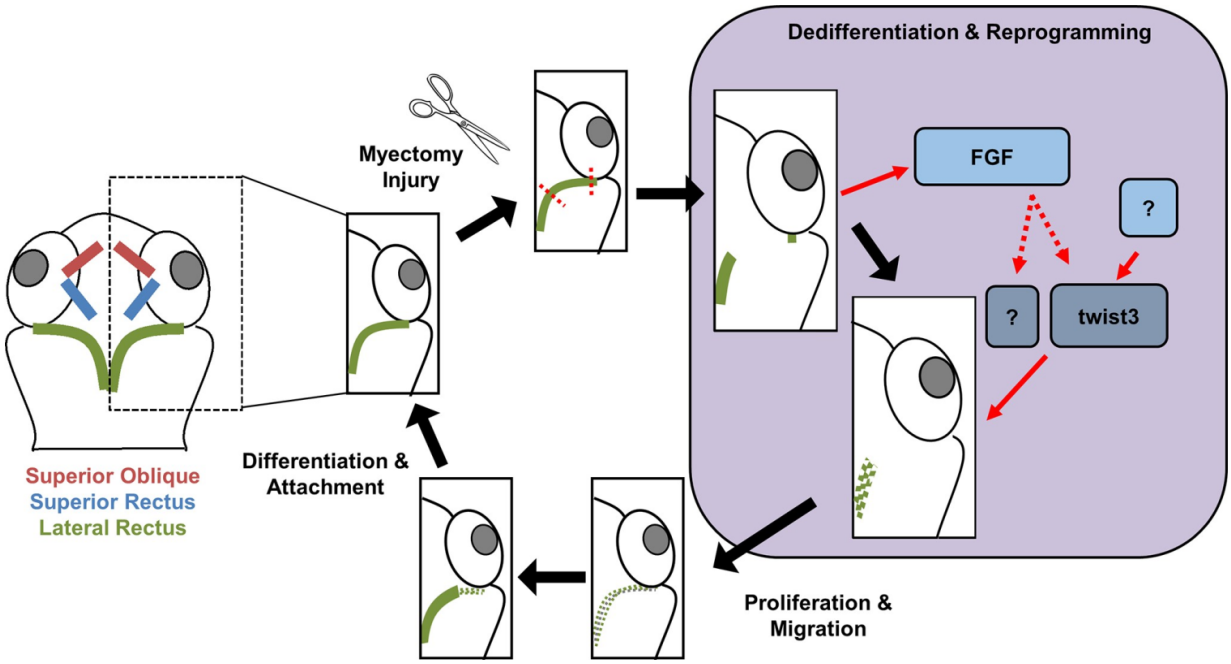

Figure 3.5: Twist3 role during EOM regeneration.
Following myectomy injury, twist3 expression is elevated and promotes myocytes cell reprogramming and dedifferentiation. The known role of Fgf combined with our results (Figure 3.4) suggest that twist3 shares the same pathway with Fgf.

3.4 Discussion

Cellular reprogramming from a more- to less-differentiated state requires coordinated changes in chromatin, gene expression and cellular architecture, driven by altered functionality of key transcription factors [39, 40]. Because of their role as master regulators of stem cells and in embryonic craniofacial development, we decided to use our unique zebrafish EOM regeneration model to test whether twist TFs play a role in EOM myocyte dedifferentiation.

In adult zebrafish, EOM regeneration begins with myocyte reprogramming - an EMT process - followed by cell cycle reentry, proliferation, and migration of the dedifferentiated myoblasts, and eventually re-differentiation into myocytes that fuse to form myofibers [10]. Our long-term goal is to understand regulations of cell identity and fate, by understanding the early steps of EOM myocytes reprogramming dedifferentiation.

Twist TFs belong to the basic helix-loop-helix (bHLH) family that is important for the regulation of cell fate decision and differentiation [41] and EMTs [42]. Twist TFs are also considered master regulators of stem cells in that they are important to maintaining the stem cell state [21, 29, 30]. In our regeneration model, twist TF knockdown impaired muscle regeneration by inhibiting myocyte reprogramming, revealing an early role for Twist that is consistent with the early induction of expression following injury and with Twist TF's role in EMT. Interestingly, this effect was specific to twist3 (homolog of mammalian twist2) and none of the other paralogs, revealing evolutionary sub-functionalization in the context of adult tissue regeneration.

It has been reported that Twist is involved in adult muscle regeneration in both *Drosophila* and mice. In *Drosophila*, persistent twist expression is a marker of embryonic precursors for adult muscle [43]. Twist is also required for adult *Drosophila* myogenesis [18]. In mouse skeletal muscle, twist expression is quickly elevated after injury [20]. In addition, murine *Twist2* (an orthologue of Zebrafish *twist3*)-dependent progenitor cells contribute to muscle regeneration [21]. In adult zebrafish, twist1a and twist1b are involved in heart regeneration [44, 45]. Our study represents the first investigation of twist within adult zebrafish skeletal muscle regeneration, and our results suggest that promoting muscle regeneration may be an evolutionarily-conserved function of twist TFs.

The role of twist1 in zebrafish development has been extensively studied. As EMT transcription factors, twist1 are involved in neural crest migration, which undergo an EMT to give rise to many different derivatives [46]. Regulated by thyroid hormone [47], retinoic acid (RA)[48], Wnt [49], Bmps and Id2a [28] signaling pathways, Twist 1a/b is required for proper development of craniofacial cartilage and skeleton [50], with Runx2 a known downstream target [13, 14]. Twist1 is also involved in blood vessel sprouting in zebrafish embryos [51]. Like twist1, twist2 is

also involved in bone formation regulated by RA [48]. Despite their significant peptide similarity, expression locations of four twist TFs differ significantly from each other, suggesting a considerable divergence of regulatory controls [52, 53]. This is supported by our findings that different twist TFs are involved in EOM regeneration and development. Twist3 is involved in zebrafish EOM regeneration but not development. In embryos with twist3 knockdown, EOM development appeared normal, although the muscle appeared longer and thinner, possibly due to a severe bulging eye phenotype (Figure 3.7 D-D'"). EOMs also developed normally after twist1a/b knock-down (Figure 3.7 B-B"). In contrast, while muscle fibers could be identified following twist2 knockdown (highlighted by actin-GFP), they failed to form a normal EOM pattern. It was difficult to differentiate the 6 pairs of EOMs based on insertion position (Figure 3.7 C-C') compared with control fish (Figure 3.7 A-A'). Instead of normal insertion patterns, muscles seemed to "wrap around" the globe (Figure 3.7 C"). In embryos, twist2 knockdown impaired EOM formation as early as 48 hpf (Figure 3.8 B-B"). This finding reveals a key difference between zebrafish embryonic development and regeneration, suggesting that regeneration is not a simple recapitulation of developmental programs but rather a distinct program, albeit one that utilizes many of the same building blocks.

An important limitation of this study is the use of MOs to knockdown gene expression. MOs have been used widely in a variety of experimental models, such as Xenopus, zebrafish and other organisms [54]. However, in embryo research, their use has been largely supplanted by CRISPR/Cas9 genetic engineering because of concerns about MO knockdown efficiency and off-target effects [55]. It should be noted that the phenotypic differences between mutants (CRISPR/Cas9) and morphants (MO knockdown) may due to the natural activation of genetic compensation induced in mutants [56]. Nevertheless, for knocking down gene expression in select

adult tissue, direct electroporation of MOs has no proper experimental substitute, and this technique has been used extensively in the adult zebrafish regeneration model [57, 58]. In this study, we followed the guidelines for use of MOs in zebrafish [55], most importantly validating multiple MOs and assessing reduction in protein level using Twist antibodies (Figure 3.1). Furthermore, since knockdown of different Twist family members resulted in specific phenotypic differences, our results are most consistent with a specific phenotypic effect rather than off-target effects. Ultimately, there are no alternative techniques for knocking down gene expression of a specific gene in a specific extraocular muscle, and hence electroporation of MOs represents the state of the art for these experiments.

Twist TFs are critically important to both embryonic development and cancer. The involvement of Twist in cancer includes EMT during metastasis [42, 59-61], as well as maintenance of cancer stem cells [42, 62-65]. In our study, injured EOMs in the twist3 knock-down group do not de-differentiate properly, consistent with an early role for Twist in reprogramming and EMT (i.e. muscle-to-mesenchymal transition). The similarities between cellular dedifferentiation and cancer have been previously noted [66-69], and our data provide additional supportive evidence.

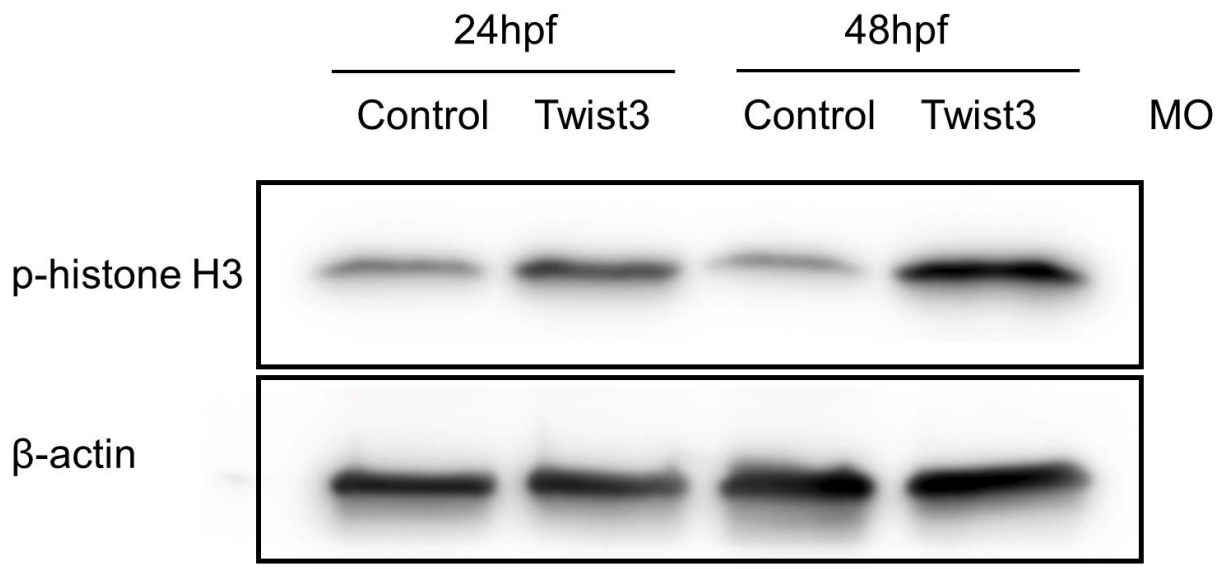

Figure 3.6: Twist3 MO does not inhibit cell proliferation during embryo development. Western blot of phospho-histone H3 shows twist3 MO injection induced p-histone H3 at 24 and 48 hpf.

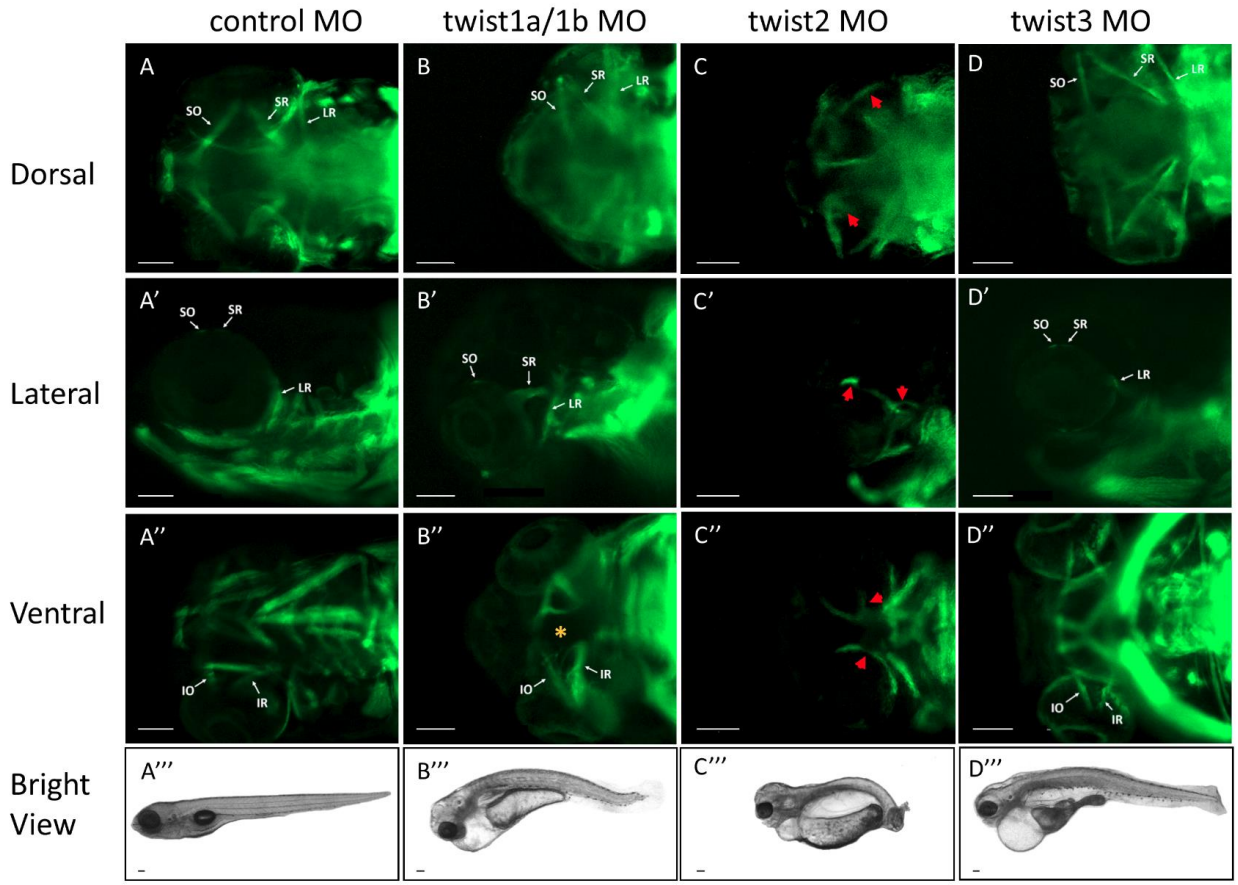

Figure 3.7: Twist2 regulates EOM development in zebrafish.
Tg(*α-actin::EGFP*) embryos that were injected with twist 1a/b, 2, or 3 MO at the one- to four-cell state demonstrated EOM formation at 5 dpf from dorsal (B-D), lateral (B'-D'), Ventral (B"-D"), and phenotype (B"'-D"') compared with control embryos (A-A"'). SO: Superior Oblique, SR: Superior Rectus, LR: Lateral Rectus, IO: Inferior Oblique, IR: Inferior Rectus. Asterisk: undeveloped jaw muscle, red arrow: incorrectly inserted EOM, scale bar: 100µm.

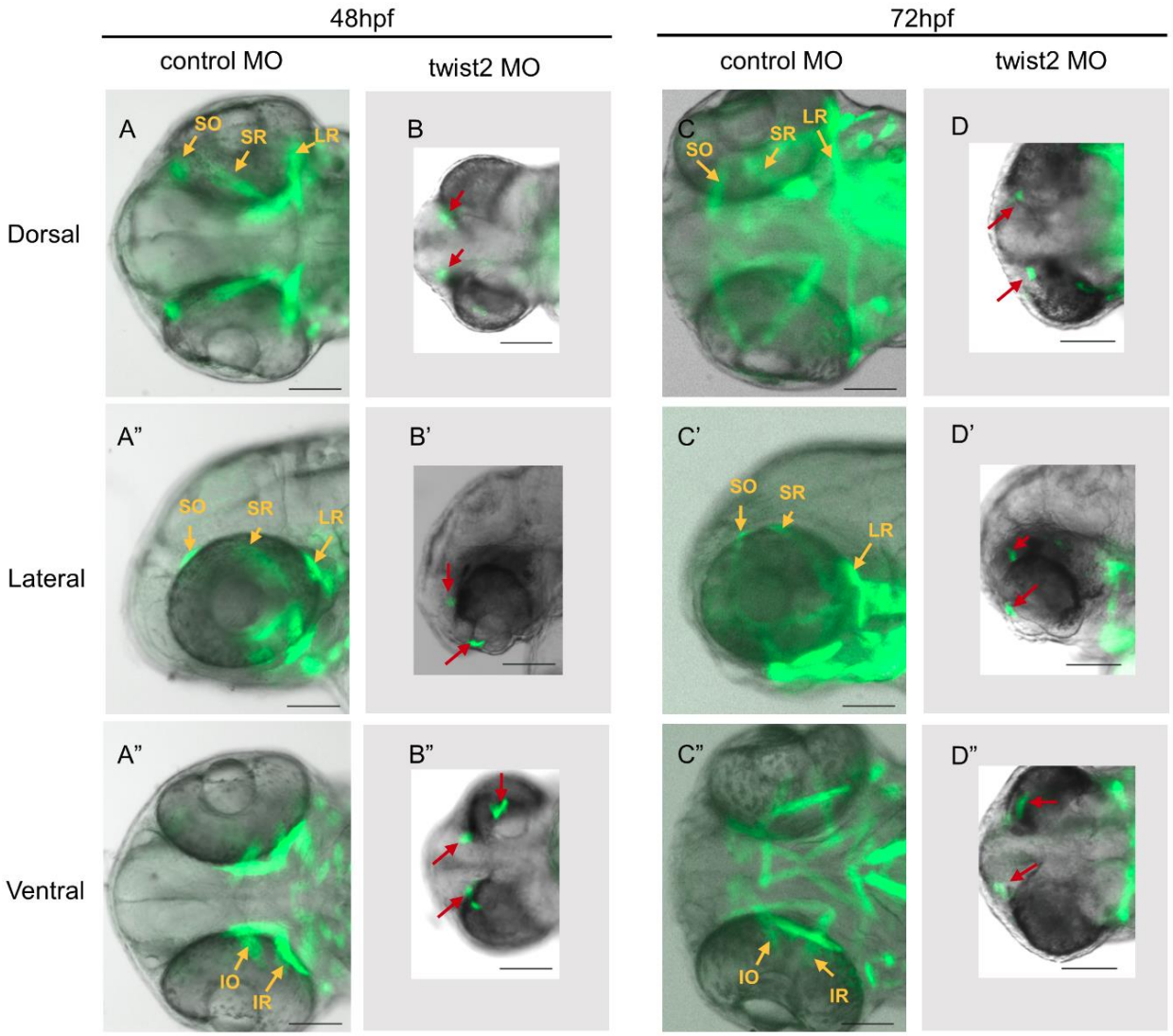

Figure 3.8: Twist2 delays EOM development in zebrafish.
Tg(*α-actin::EGFP*) embryos that were injected with twist2 MO at the one- to four-cell state demonstrated EOM formation at 48 or 72 hpf from dorsal (B, D), lateral (B'-D'), and ventral (B"-D") compared with control embryos (A-A", C-C"). SO: Superior Oblique, SR: Superior Rectus, LR: Lateral Rectus, IO: Inferior Oblique, IR: Inferior Rectus. Red arrow: incorrectly inserted EOM, scale bar: 100µm.

3.5 References

1. Laumonier T, Menetrey J. Muscle injuries and strategies for improving their repair. *Journal of experimental orthopaedics*. 2016;3(1):15. Epub 2016/07/23. doi: 10.1186/s40634-016-0051-7. PubMed PMID: 27447481; PubMed Central PMCID: PMCPMC4958098.
2. Garg K, Ward CL, Hurtgen BJ, Wilken JM, Stinner DJ, Wenke JC, et al. Volumetric muscle loss: persistent functional deficits beyond frank loss of tissue. *Journal of orthopaedic research: official publication of the Orthopaedic Research Society*. 2015;33(1):40-6. Epub 2014/09/19. doi: 10.1002/jor.22730. PubMed PMID: 25231205.
3. Carlson BM. Muscle regeneration in amphibians and mammals: Passing the torch. *Developmental Dynamics*. 2003;226(2):167-81. doi: 10.1002/dvdy.10223.
4. Jopling C, Sleep E, Raya M, Martí M, Raya A, Belmonte JCI. Zebrafish heart regeneration occurs by cardiomyocyte dedifferentiation and proliferation. *Nature*. 2010;464(7288):606.
5. Singh SP, Holdway JE, Poss KD. Regeneration of amputated zebrafish fin rays from de novo osteoblasts. *Dev Cell.* 2012;22(4):879-86. Epub 2012/04/21. doi: 10.1016/j.devcel.2012.03.006. PubMed PMID: 22516203; PubMed Central PMCID: PMCPMC3341140.
6. Lee Y, Nachtrab G, Klinsawat PW, Hami D, Poss KD. Ras controls melanocyte expansion during zebrafish fin stripe regeneration. *Disease models & mechanisms.* 2010;3(7-8):496-503.
7. Stewart S, Stankunas K. Limited dedifferentiation provides replacement tissue during zebrafish fin regeneration. *Developmental Biology.* 2012;365(2):339-49. doi: https://doi.org/10.1016/j.ydbio.2012.02.031.
8. Ramachandran R, Fausett BV, Goldman D. Ascl1a regulates Muller glia dedifferentiation and retinal regeneration through a Lin-28-dependent, let-7 microRNA signalling pathway. *Nat Cell Biol*. 2010;12(11):1101-7. Epub 2010/10/12. doi: 10.1038/ncb2115. PubMed PMID: 20935637; PubMed Central PMCID: PMCPMC2972404.
9. Simon HG, Nelson C, Goff D, Laufer E, Morgan BA, Tabin C. Differential expression of myogenic regulatory genes and Msx‐1 during dedifferentiation and redifferentiation of regenerating amphibian limbs. *Developmental Dynamics.* 1995;202(1):1-12.
10. Saera-Vila A, Kasprick DS, Junttila TL, Grzegorski SJ, Louie KW, Chiari EF, et al. Myocyte Dedifferentiation Drives Extraocular Muscle Regeneration in Adult Zebrafish. *Investigative ophthalmology & visual science*. 2015;56(8):4977-93. Epub 2015/08/01. doi: 10.1167/iovs.14-16103. PubMed PMID: 26230763; PubMed Central PMCID: PMCPMC4525682.
11. Moyer AL, Wagner KR. Regeneration versus fibrosis in skeletal muscle. *Current opinion in rheumatology*. 2011;23(6):568-73. Epub 2011/09/22. doi: 10.1097/BOR.0b013e32834bac92. PubMed PMID: 21934499.
12. Gemberling M, Bailey TJ, Hyde DR, Poss KD. The zebrafish as a model for complex tissue regeneration. *Trends in Genetics*. 2013;29(11):611-20. doi: https://doi.org/10.1016/j.tig.2013.07.003.

13. Yang D-C, Tsai C-C, Liao Y-F, Fu H-C, Tsay H-J, Huang T-F, et al. Twist Controls Skeletal Development and Dorsoventral Patterning by Regulating Runx2 in Zebrafish. *PLOS ONE*. 2011;6(11):e27324. doi: 10.1371/journal.pone.0027324.
14. Kronenberg HM. Twist genes regulate Runx2 and bone formation. *Dev Cell*. 2004;6(3):317-8. Epub 2004/03/20. PubMed PMID: 15030754.
15. Gong XQ, Li L. Dermo-1, a Multifunctional Basic Helix-Loop-Helix Protein, Represses MyoD Transactivation via the HLH Domain, MEF2 Interaction, and Chromatin Deacetylation. *Journal of Biological Chemistry*. 2002;277(14):12310-7. doi: 10.1074/jbc.M110228200.
16. Mastroyiannopoulos Nikolaos P, Antoniou Antonis A, Koutsoulidou A, Uney James B, Phylactou Leonidas A. Twist reverses muscle cell differentiation through transcriptional down-regulation of myogenin. *Bioscience Reports*. 2013;33(6):e00083. doi: 10.1042/BSR20130068. PubMed PMID: PMC3848576.
17. Castanon I, Von Stetina S, Kass J, Baylies MK. Dimerization partners determine the activity of the Twist bHLH protein during Drosophila mesoderm development. *Development*. 2001;128(16):3145-59.
18. Cripps RM, Olson EN. Twist Is Required for Muscle Template Splitting during Adult Drosophila Myogenesis. *Developmental biology*. 1998;203(1):106-15.
19. Soo K, O'Rourke MP, Khoo P-L, Steiner KA, Wong N, Behringer RR, et al. Twist Function Is Required for the Morphogenesis of the Cephalic Neural Tube and the Differentiation of the Cranial Neural Crest Cells in the Mouse Embryo. *Developmental Biology*. 2002;247(2):251-70. doi: http://dx.doi.org/10.1006/dbio.2002.0699.
20. Po Z, P. HE. Embryonic myogenesis pathways in muscle regeneration. *Developmental Dynamics*. 2004;229(2):380-92. doi: doi:10.1002/dvdy.10457.
21. Liu N, Garry GA, Li S, Bezprozvannaya S, Sanchez-Ortiz E, Chen B, et al. A Twist2-dependent progenitor cell contributes to adult skeletal muscle. *Nature cell biology*. 2017;19(3):202.
22. Gitelman I. Evolution of the vertebrate twist family and synfunctionalization: a mechanism for differential gene loss through merging of expression domains. *Molecular Biology and Evolution*. 2007;24(9):1912-25. doi: 10.1093/molbev/msm120.
23. Germanguz I, Gitelman I. All four twist genes of zebrafish have partially redundant, but essential, roles in patterning the craniofacial skeleton. *Journal of Applied Ichthyology*. 2012;28(3):364-71. doi: doi:10.1111/j.1439-0426.2012.02016.x.
24. Dahm R, Nüsslein-Volhard C. Zebrafish: a practical approach: Oxford University Press New York; 2002.
25. Saera-Vila A, Kish PE, Kahana A. Fgf regulates dedifferentiation during skeletal muscle regeneration in adult zebrafish. *Cellular Signalling*. 2016;28(9):1196-204. doi: https://doi.org/10.1016/j.cellsig.2016.06.001.
26. Tingle CF, Magnuson B, Zhao Y, Heisel CJ, Kish PE, Kahana A. Paradoxical Changes Underscore Epigenetic Reprogramming During Adult Zebrafish Extraocular Muscle Regeneration. *Investigative ophthalmology & visual science*. 2019;60(15):4991-9. doi: 10.1167/iovs.19-27556.
27. Poss KD, Shen J, Nechiporuk A, McMahon G, Thisse B, Thisse C, et al. Roles for Fgf Signaling during Zebrafish Fin Regeneration. *Developmental Biology*. 2000;222(2):347-58. doi: https://doi.org/10.1006/dbio.2000.9722.

28. Das A, Crump JG. Bmps and Id2a Act Upstream of Twist1 To Restrict Ectomesenchyme Potential of the Cranial Neural Crest. *PLoS Genetics*. 2012;8(5):e1002710. doi: 10.1371/journal.pgen.1002710. PubMed PMID: PMC3349740.
29. Isenmann S, Arthur A, Zannettino AC, Turner JL, Shi S, Glackin CA, et al. TWIST family of basic helix-loop-helix transcription factors mediate human mesenchymal stem cell growth and commitment. *Stem Cells*. 2009;27(10):2457-68. Epub 2009/07/18. doi: 10.1002/stem.181. PubMed PMID: 19609939.
30. Gronthos S. Chapter 2 - Features of Mesenchymal Stem Cells. In: Chen X-D, editor. A Roadmap to Non-Hematopoietic Stem Cell-based Therapeutics: Academic Press; 2019. p. 15-38.
31. Au - Hyde DR, Au - Godwin AR, Au - Thummel R. In vivo Electroporation of Morpholinos into the Regenerating Adult Zebrafish Tail Fin. *JoVE*. 2012;(61):e3632. doi: doi:10.3791/3632.
32. Aihara H, Miyazaki J-i. Gene transfer into muscle by electroporation in vivo. Nature *Biotechnology*. 1998;16(9):867-70. doi: 10.1038/nbt0998-867.
33. Saera-Vila A, Kish PE, Louie KaW, Grzegorski SJ, Klionsky DJ, Kahana A. Autophagy regulates cytoplasmic remodeling during cell reprogramming in a zebrafish model of muscle regeneration. *Autophagy*. 2016;12(10):1864-75. doi: 10.1080/15548627.2016.1207015. PubMed PMID: PMC5066936.
34. Weaver JC. Electroporation of cells and tissues. *IEEE Transactions on Plasma Science*. 2000;28(1):24-33. doi: 10.1109/27.842820.
35. McMahon JM, Wells DJ. Electroporation for Gene Transfer to Skeletal Muscles. *BioDrugs*. 2004;18(3):155-65. doi: 10.2165/00063030-200418030-00002.
36. Peng B, Zhao Y, Lu H, Pang W, Xu Y. In vivo plasmid DNA electroporation resulted in transfection of satellite cells and lasting transgene expression in regenerated muscle fibers. *Biochemical and Biophysical Research Communications*. 2005;338(3):1490-8. doi: https://doi.org/10.1016/j.bbrc.2005.10.111.
37. Saera-Vila A, Louie KaW, Sha C, Kelly RM, Kish PE, Kahana A. Extraocular muscle regeneration in zebrafish requires late signals from Insulin-like growth factors. *PLOS ONE*. 2018;13(2):e0192214. doi: 10.1371/journal.pone.0192214.
38. O'Rourke MP, Soo K, Behringer RR, Hui CC, Tam PP. Twist plays an essential role in FGF and SHH signal transduction during mouse limb development. *Dev Biol.* 2002;248(1):143-56. Epub 2002/07/27. PubMed PMID: 12142027.
39. Takahashi K, Tanabe K, Ohnuki M, Narita M, Ichisaka T, Tomoda K, et al. Induction of pluripotent stem cells from adult human fibroblasts by defined factors. *Cell*. 2007;131(5):861-72.
40. Skrypek N, Goossens S, De Smedt E, Vandamme N, Berx G. Epithelial-to-Mesenchymal Transition: *Epigenetic Reprogramming Driving Cellular Plasticity. Trends in Genetics*. 2017;33(12):943-59. doi: https://doi.org/10.1016/j.tig.2017.08.004.
41. Murre C, Bain G, van Dijk MA, Engel I, Furnari BA, Massari ME, et al. Structure and function of helix-loop-helix proteins. *Biochim Biophys Acta*. 1994;1218(2):129-35. Epub 1994/06/21. PubMed PMID: 8018712.
42. Kang Y, Massagué J. Epithelial-Mesenchymal Transitions: Twist in Development and Metastasis. Cell. 2004;118(3):277-9. doi: https://doi.org/10.1016/j.cell.2004.07.011.
43. Bate M, Rushton E, Currie DA. Cells with persistent twist expression are the embryonic precursors of adult muscles in Drosophila. *Development*. 1991;113(1):79-89.

44. Kim J, Wu Q, Zhang Y, Wiens KM, Huang Y, Rubin N, et al. PDGF signaling is required for epicardial function and blood vessel formation in regenerating zebrafish hearts. *Proceedings of the National Academy of Sciences*. 2010;107(40):17206-10. doi: 10.1073/pnas.0915016107.
45. Missinato MA, Tobita K, Romano N, Carroll JA, Tsang M. Extracellular component hyaluronic acid and its receptor Hmmr are required for epicardial EMT during heart regeneration. *Cardiovascular Research*. 2015;107(4):487-98. doi: 10.1093/cvr/cvv190.
46. Le Douarin NM, Creuzet S, Couly G, Dupin E. Neural crest cell plasticity and its limits. *Development*. 2004;131(19):4637-50. Epub 2004/09/11. doi: 10.1242/dev.01350. PubMed PMID: 15358668.
47. Bohnsack BL, Kahana A. Thyroid hormone and retinoic acid interact to regulate zebrafish craniofacial neural crest development. *Developmental Biology*. 2013;373(2):300-9. doi: https://doi.org/10.1016/j.ydbio.2012.11.005.
48. Li N, Kelsh RN, Croucher P, Roehl HH. Regulation of neural crest cell fate by the retinoic acid and Pparg signalling pathways. *Development*. 2010;137(3):389-94. doi: 10.1242/dev.044164.
49. Tuttle AM, Hoffman TL, Schilling TF. Rabconnectin-3a Regulates Vesicle Endocytosis and Canonical Wnt Signaling in Zebrafish Neural Crest Migration. *PLOS Biology*. 2014;12(5):e1001852. doi: 10.1371/journal.pbio.1001852.
50. Teng CS, Ting M-c, Farmer DJT, Brockop M, Maxson RE, Crump JG. Altered bone growth dynamics prefigure craniosynostosis in a zebrafish model of Saethre-Chotzen syndrome. *eLife*. 2018;7:e37024. doi: 10.7554/eLife.37024.
51. Mahmoud MM, Kim HR, Xing R, Hsiao S, Mammoto A, Chen J, et al. TWIST1 Integrates Endothelial Responses to Flow in Vascular Dysfunction and Atherosclerosis. *Circulation Research*. 2016;119(3):450-62. doi: doi:10.1161/CIRCRESAHA.116.308870.
52. Yeo GH, Cheah FSH, Winkler C, Jabs EW, Venkatesh B, Chong SS. Phylogenetic and evolutionary relationships and developmental expression patterns of the zebrafish twist gene family. *Development Genes and Evolution*. 2009;219(6):289-300. doi: 10.1007/s00427-009-0290-z.
53. Germanguz I, Lev D, Waisman T, Kim C-H, Gitelman I. Four twist genes in zebrafish, four expression patterns. *Developmental Dynamics.* 2007;236(9):2615-26. doi: doi:10.1002/dvdy.21267.
54. Eisen JS, Smith JC. Controlling morpholino experiments: don't stop making antisense. *Development*. 2008;135(10):1735-43. doi: 10.1242/dev.001115.
55. Stainier DYR, Raz E, Lawson ND, Ekker SC, Burdine RD, Eisen JS, et al. Guidelines for morpholino use in zebrafish. *PLoS genetics*. 2017;13(10):e1007000-e. doi: 10.1371/journal.pgen.1007000. PubMed PMID: 29049395.
56. Rossi A, Kontarakis Z, Gerri C, Nolte H, Hölper S, Krüger M, et al. Genetic compensation induced by deleterious mutations but not gene knockdowns. *Nature*. 2015;524(7564):230-3. doi: 10.1038/nature14580.
57. Thummel R, Kathryn Iovine M. Using Morpholinos to Examine Gene Function During Fin Regeneration. In: Moulton HM, Moulton JD, editors. Morpholino Oligomers: Methods and Protocols. New York, NY: Springer New York; 2017. p. 79-85.

58. Thummel R, Bailey TJ, Hyde DR. In vivo electroporation of morpholinos into the adult zebrafish retina. *J Vis Exp*. 2011;(58):e3603-e. doi: 10.3791/3603. PubMed PMID: 22231802.
59. Puisieux A, Brabletz T, Caramel J. Oncogenic roles of EMT-inducing transcription factors. *Nature cell biology*. 2014;16(6):488.
60. Puisieux A, Valsesia-Wittmann S, Ansieau S. A twist for survival and cancer progression. *British Journal of Cancer*. 2006;94(1):13-7. doi: 10.1038/sj.bjc.6602876.
61. Kim MS, Lee HS, Kim YJ, Lee DY, Kang SG, Jin W. MEST induces Twist-1-mediated EMT through STAT3 activation in breast cancers. *Cell Death & Differentiation*. 2019. doi: 10.1038/s41418-019-0322-9.
62. Li J, Zhou BP. Activation of β-catenin and Akt pathways by Twist are critical for the maintenance of EMT associated cancer stem cell-like characters. *BMC Cancer*. 2011;11(1):49. doi: 10.1186/1471-2407-11-49.
63. Jung H-Y, Yang J. Unraveling the TWIST between EMT and cancer stemness. *Cell Stem Cell.* 2015;16(1):1-2.
64. Glackin CA. Nanoparticle Delivery of TWIST Small Interfering RNA and Anticancer Drugs: A Therapeutic Approach for Combating Cancer. *The Enzymes.* 2018;44:83-101.
65. Su J, Wu S, Wu H, Li L, Guo T. CD44 is functionally crucial for driving lung cancer stem cells metastasis through Wnt/ β ‐catenin‐FoxM1‐Twist signaling. *Molecular carcinogenesis.* 2016;55(12):1962-73.
66. Kumar SM, Liu S, Lu H, Zhang H, Zhang PJ, Gimotty PA, et al. Acquired cancer stem cell phenotypes through Oct4-mediated dedifferentiation. *Oncogene*. 2012;31(47):4898.
67. Herreros-Villanueva M, Zhang J, Koenig A, Abel E, Smyrk TC, Bamlet W, et al. SOX2 promotes dedifferentiation and imparts stem cell-like features to pancreatic cancer cells. *Oncogenesis*. 2013;2(8):e61.
68. Friedmann‐Morvinski D, Verma IM. Dedifferentiation and reprogramming: origins of cancer stem cells. *EMBO reports.* 2014;15(3):244-53.
69. Saito S, Lin Y-C, Nakamura Y, Eckner R, Wuputra K, Kuo K-K, et al. Potential application of cell reprogramming techniques for cancer research. *Cellular and Molecular Life Sciences.* 2019;76(1):45-65. doi: 10.1007/s00018-018-2924-7.

Chapter 4: Role of *Evc2/Limbin* in midfacial development[4]

4.1 Introduction

Ellis-van Creveld (EvC) syndrome is an autosomal recessive chondroectodermal dysplasia [1]. Affected individuals display a wide spectrum of symptoms including dwarfism, postaxial polydactyly, nail dysplasia, atrial septal or atrioventricular septal cardiovascular defects, and dental anomalies [1, 2]. Genetic studies have allowed identification of two causative genes for EvC syndrome, *EVC* and *EVC2*, and homozygous mutations in either have been linked to two-thirds of EvC patients [3]. Additionally, EvC syndrome [4] has been characterized as a ciliopathy because the EVC and EVC2 proteins are intracellularly localized at the bottom of the primary cilium, where they form a heterotrimeric protein complex with SMO and transduce Hedgehog signaling [5, 6]. Our previous studies interestingly identified the bovine ortholog *LIMBIN*/*EVC2* as a causative gene for chondrodysplasia in Japanese brown cattle [7]. Recent studies also identify *LIMBIN*/*EVC2* mutations in dwarf Tyrolean Grey cattle [8]. These two studies suggest an evolutionarily conserved function of *EVC2* among different species.

Multiple studies have linked EvC syndrome with a wide range of craniofacial abnormalities including an enlarged skull, depressed nasal bridge, class II skeletal pattern with or without mandibular prognathism, and a skeletal open bite. Patients less frequently exhibit normocephaly with minimal facial defects and instances of class I skeletal patterns [9-13]. The variation of mid-

[4] Published as Kulkarni A, Louie KW, Yatabe M, de Olivera Ruellas AC, Mochida Y, Cevidanes LHS, Mishina Y, Zhang H. 2018. A cilliary protein EVC2/LIMBIN plays a critical role in the skull base for mid-facial development. *Frontiers in Physiology* 9: 1484.

facial defects reported in EvC patients prompted the generation of mouse models for EvC syndrome that facilitate characterization of affected mid-facial development and associated pathological mechanisms.

We and others have used both *Evc* and *Evc2* mutant mice to characterize different aspects of abnormal development [5, 14, 15]. Generating our own *Evc2* mutant mice enabled us to characterize the pathological mechanisms leading to abnormal appendicular bone and hypomorphic enamel development [15-17]. Our subsequent studies further demonstrated the expression of *Evc2* in the mid-facial regions [18] and mid-facial defects in *Evc2* global mutant mice [19]. We most recently employed a conditional, *Cre*-mediated approach towards deleting *Evc2* in a neural crest-specific manner. In a comparison between global and *P0-Cre*-mediated *Evc2* mutants, we reported that at postnatal day 8 (P8): (1) *Evc2 P0* mutants somewhat recapitulate craniofacial and tooth phenotypes exhibited by *Evc2* global mutant mice and that (2) many mid-facial defects identified in the *Evc2* global mutants are not present in the *Evc2 P0* mutants [20]. This latter finding was surprising and warranted further study since *P0-Cre* predominantly targets the mid-facial region where *Evc2* is, similarly, expressed.

To identify a pathological mechanism leading to the mid-facial defects in *Evc2* mutant mice and EvC patients, we compared outcomes of *Evc2* deletion within the neural crest-derived tissues of two similar, but not identical, neural crest-specific *Cre* lines: *P0-Cre* and *Wnt1-Cre*. Recombination efficiency and craniofacial deficiencies varied between mouse lines and facial region. Specifically, although both *Cre* lines showed indistinguishable recombination efficiency within the mid-facial bones, *Wnt1-Cre*-mediated excision of *Evc2* resulted in a more robust mid-facial hypoplasia. Conversely, those two Cre lines showed differential recombination efficiencies within the anterior portion of the skull base. Analyses of these two mutant mice lines highlights

the critical function of the skull base during postnatal mid-facial development and uncovers the pathological mechanisms whereby the shortened skull base, due to *Evc2* loss of function within those bones, leads to characteristic EvC mid-facial defects.

4.2 Materials and Methods

4.2.1 Animal Model

Animals were maintained and used in compliance with the Institutional Animal Care and Use Committee (IACUC) of the University of Michigan in accordance with the National Institutes of Health Guidelines for Care and Use of Animals in research, and all experimental procedures were approved by the IACUC of the University of Michigan. *Evc2* floxed mice used in this study were generated by our group and reported previously [15]. Neural crest-specific *Evc2* mutant mice were generated by crossing *Evc2* floxed mice either with *Wnt1-Cre* mice [21] or with *P0*-Cre mice, *C57BL/6J-Tg(P0-Cre)94Imeg* (ID 148), which was provided by Dr. Kenichi Yamamura [22]. All mice were maintained in a mixed background of C57BL6/J and 129S6 and were crossed and maintained in our semi-closed mouse colony for at least 5 years.

4.2.2 Micro-CT (µCT)

Micro-CT scanning of fixed heads was performed at the University of Michigan using a Micro-CT Core (µCT100 Scanco Medical, Bassersdorf, Switzerland). Scan settings were as following: voxel size 12 µm, 55 kVp, 109 µA, 0.5 mm AL filter, and integration time 500 ms.

4.2.3 Cephalometric Analysis

Lateral radiographic films were taken according to previously published methods. The linear and angular cephalometric analyses followed the parameters outlined in a previous report [23] with certain modifications (Table 4.1). An additional landmark (Br) was placed on the bregma, the point of intersection between the sagittal and coronal sutures. The distance from the

bregma (Br) to the most posterior point of the skull (Po) was measured, denoted by the abbreviation Po-Br. The angle ABrL/PoBrL was also measured between the Po-Br segment described above and the A-Br segment, which stretches the combined length of the nasal and frontal bones. This angle was used to emulate the concavity of the skull superficial to the cranial vault. Overall, 15 landmarks (Table 4.1) were placed in each sample and a total of 20 linear measurements and 15 angular measurements were taken (Table 4.1).

Table 4.1: Description of landmarks and landmark-associated linear and angular measurements.

Landmark	Description
A	The most anterior point on the nasal bone.
Bl	The intersection between the lingual surface of the lower incisors and the most anterior part of the lingual alveolar bone.
Br	The bregma, the point of intersection between the sagittal and coronal sutures.
Bu	A point on the premaxilla between jaw bone and the lingual surface of the upper lingual incisors.
E	The intersection between the frontal bone and the most superior-anterior point of the posterior limit of the ethmoid bone.
Id	The most inferior and anterior point on the alveolar process of the mandible.
Ii	The most prominent point between the incisal edges of the lower incisors.
Iu	The most prominent point between the incisal edges of the upper incisors.
Ml	The intersection between the mandibular alveolar bone and the mesial surface on the first molar.
Mn	A point in the deepest part of the antegonial notch curvature.
Mu	The intersection between the maxillary bone and the mesial surface of the upper first molar.
N	A point on the nasofrontal suture.
Po	The most posterior point on the cranial vault.
Pr	The most inferior and anterior point on the alveolar process of the premaxilla.
So	The intersection between the posterior border of the basisphenoid and the tympanic bulla.

Landmarks	Segment	Landmarks	Angle
A-N	Nasal bone length	PoEL/SoEL	Cranial vault to cranial base
A-Pr	Nasal bone height	ANL/SoEL	Nasal bone to cranial base
E-Mu	Viscerocranial height	ANL/PoEL	Nasal bone to cranial vault
E-Iu	Growth axis of upper face	ANL/PrNL	Nasal bone to premaxilla
E-Bu	Viscerocranial length (posterior to anterior incisors)	MuBuL/SoEL	Maxilla-premaxilla to cranial base
E-Pr	Viscerocranial length (anterior to anterior incisors)	MuBuL/PoEL	Maxilla-premaxilla to cranial vault
N-Pr	Relative position of pre-maxilla to cranium	PrEL/SoEL	Premaxilla to cranial base
Mu-Pr	Distance between molar and incisor in maxilla	BuEL/PoEL	Premaxilla to cranial vault
Mu-Bu	Palatal length	BuEL/SoEL	Upper incisors to cranial base
Mn-Id	Mandibular corpus length	IuEL/PoEL	Upper incisors to cranial vault
Ml-Bl	Mandibular lingual alveolar bone length	MuBuL/PrIuL	Upper incisor inclination
Pr-Iu	Erupted upper incisor length	MIliL/IdLiL	Lower incisor inclination
Id-Ii	Erupted lower incisor length	ABrL/PoBrL	Angle of cranial vault
Ml-Ii	Distance between molar and incisor in mandible	PrEL/PoEL	Premaxilla to cranial vault
So-E	Length of anterior cranial base		
Po-E	Neurocranial length		
Po-Br	Length of posterior cranium		
Po-Mu	The distance between the first molar to the most posterior point		
Po-A	Total skull length		

4.2.4 Image Acquisition, Segmentation, and Surface Model Analysis

We performed shape comparisons of the nasal, frontal and parietal bones between controls and mutants (*Evc2* $^{fl/fl}$; *Wnt1-Cre*). The surface model for each bone was generated based on the micro-CT data, using ITK-SNAP (open-source software developed by grants and contracts from the U.S. National Institutes of Health, www.itksnap.org). For shape comparisons, landmarks were placed on the individual bone surfaces by using "modules" developed in 3D Slicer (open-source software, www.slicer.org). There 3D Slicer modules were then used to both superimpose the two bones based on the landmarks (CMF Registration) and to visualize shape differences (Shape

Population Viewer). Model superimpositions for the mid-line region of the skulls were carried out using 3D Slicer with the following landmarks on the interparietal bones and basioccipital bones: right and left anterolateral tips of the interparietal bone, cross point between the median line and the line which connects left and right anterolateral tip of the interparietal bone, and posterior tip of the interparietal bone. Model superimpositions for nasal, frontal and parietal bones were carried out using 3D Slicer with landmarks on the right and left of anterolateral and posterior tips of each bone. Superimpositions were achieved by posterior registration of the two models. The length of the skull base and each indicated segment of the skull base were determined by assessing the linear distance between the most anterior midline point of and the most posterior point on the midline region of the skull base or the indicated segment of the skull base using a module program, Q3DC, in 3D Slicer.

4.2.5 Statistical Analysis

The Mann-Whitney U test was done by using SPSS21.0 to evaluate the linear and angular measurements between controls and mutants.

4.3 Results

4.3.1 *Evc2* Mutation Within Neural Crest Cells Leads to Craniofacial Abnormalities

Our previous studies indicated that global *Evc2* mutation led to retarded growth and significantly affected both body and head size [15, 19]. To better characterize the function of *Evc2* in craniofacial development, we generated mutant mice with *Evc2* deleted in the neural crest-derived cells. Both *P0-Cre* and *Wnt1-Cre* mediate nearly identical recombination efficiencies within the mid-facial region [21, 22] (our own comparisons, data not shown). However, *Evc2* deletion mediated by the *P0-Cre* (*Evc2* $^{fl/fl}$*; P0-Cre*, abbreviated as *Evc2 P0* mutants) leads to an overall shortened head and delayed mandibular incisor eruption at postnatal day 8 (P8) (Figure 4.1

A). In *Evc2 P0* mutants at P28, we observed less pronounced reductions in head and incisor lengths (Figure 4.1 B). *Evc2* deletions mediated by *Wnt1-Cre* (*Evc2* $^{fl/fl}$*; Wnt1-Cre,* abbreviated as *Evc2 Wnt1* mutants) did not affect head length at P8 but did lead to shortened head and hypomorphic incisor dimensions at P28 (Figure 4.1 A and B). Unlike *Evc2* global mutant mice, there was no apparent neonatal or postnatal death observed in either *Evc2 P0* or *Evc2 Wnt1* mutant groups at the above time points. Furthermore, in both types of *Evc2* cKO, at P8 and P28, we observed insignificant gender-specific differences, particularly in the parameters characterizing mid-facial defects. Lack of gender-specific observations is consistent with previous studies and we, therefore, did not match genders in our comparative analyses [24, 25]. Therefore we combined both genders for the rest of our comparisons.

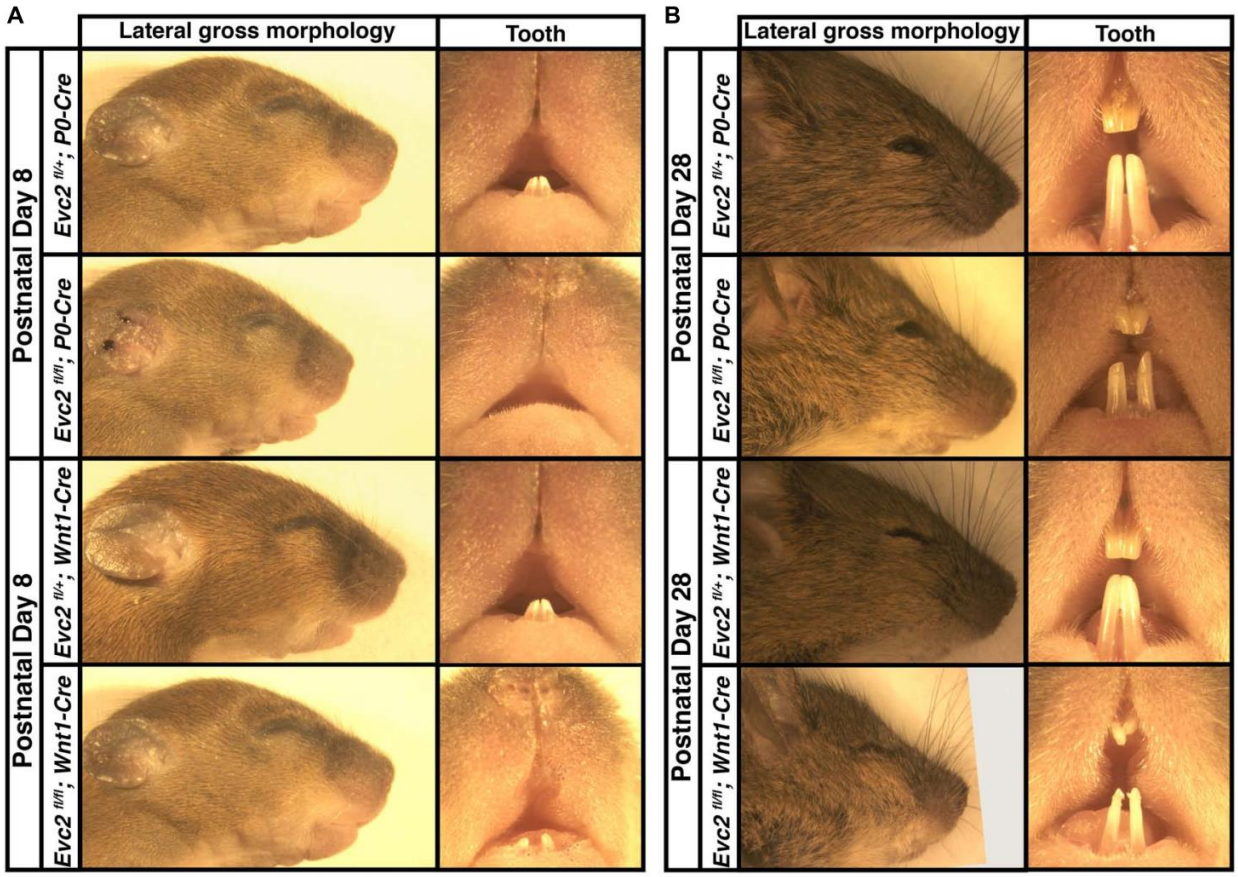

Figure 4.1: Gross morphologies of heads from *Evc2 P0* mutants and *Evc2 Wnt1* mutants. Images represent P8 (A) and P28 (B).

4.3.2 *Evc2 P0* Mutants Showed More Aspects of Mid-Facial Defects than *Evc2 Wnt1* Mutants at P8

To characterize the abnormal craniofacial development observed in both *Evc2 P0* mutants and *Evc2 Wnt1* mutants, we examined the linear and angular dimensions from lateral cephalometric radiographs. In *Evc2 P0* mutants at P8, the lateral cephalometric analysis indicated abnormalities in the incisors, skull base, and mid-facial regions. We specifically found decreases in growth axes of the upper face (E-Iu), viscerocranial length (E-Bu), erupted upper incisor length (Pr-Iu), erupted lower incisor length (Id-Ii), distance between the first molar and incisor in mandible (Ml-Ii), length of anterior cranial base (So-E), neurocranial length (Po-E), the distance between the first molar to the most posterior point (Po-Mu), and total skull length (Po-A), respectively (Figure 4.2 A, Table 4.2). These phenotypic observations recapitulate many of the mid-facial defects of the *Evc2* global mutants that we previously reported (Badri et al. 2016a). Additionally, we found a shallow mid-facial region in the *Evc2 P0* mutants, as evidenced by decreased angle measures in nasal bone to cranial base (ANL/SoEL), maxilla-premaxilla to cranial base (MuBuL/SoEL), maxilla-premaxilla to cranial vault (MuBuL/PoEL), upper incisors to cranial base (BuEL/SoEL), and angle of cranial vault (ABrL/PoBrL), respectively (Figure 4.2 B, Table 4.2).

Similar analyses of the *Evc2 Wnt1* mutants revealed abnormalities limited to the incisors and the skull base. We detected decreases in erupted upper incisor (Pr-Iu), erupted lower incisor (Id-Ii), and distance between the first molar and incisor in the mandible (Ml-Ii), respectively (Figure 4.2 C, Table 4.2). Similar to *Evc2 P0* mutants, these phenotypic observations recapitulate

some characteristics of *Evc2* global mutants [18, 19]. Additionally, we also found a shortened skull base in the *Evc2 Wnt1* mutants, as evidenced by decreased length in the anterior skull base (So-E) (Figure 4.2 C). Although most of the linear measurements showed no significant differences between control and *Evc2 Wnt1* mutants, we observed a slanted mid-facial region in the *Evc2 Wnt1* mutants, supported by the following decreased angle measures: the nasal bone to the skull base (ANL/SoEL), the maxilla-premaxilla to the skull base (MuBuL/SoEL), the premaxilla to the cranial base (PrEL/SoEL), the premaxilla to the cranial vault (BuEL/PoEL), and the angle of the cranial vault (ABrL/PoBrL) (Figure 4.2D). In summary (Table 4.2), at P8 both *Evc2 P0* mutants and *Evc2 Wnt1* mutants showed fewer aspects of mid-facial defects compared to *Evc2* global mutants. Of the two types of conditional mutants, *Evc2 P0* mutants showed more severe and widespread abnormalities compared to *Evc2 Wnt1* mutants at P8 (Table 4.2).

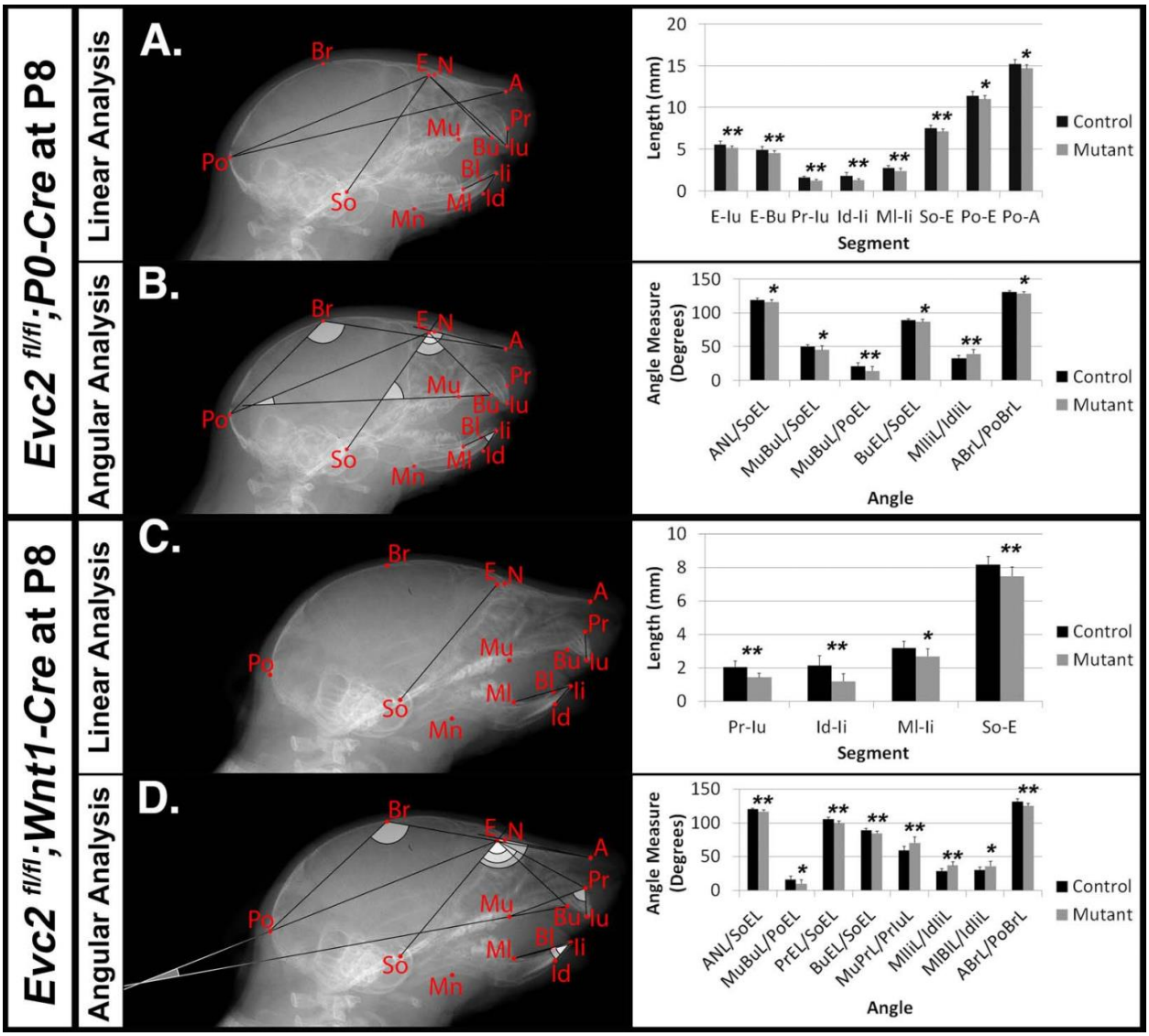

Figure 4.2: Differential mid-facial defects between *Evc2 P0* mutants and *Evc2 Wnt1* mutants at P8.

Lateral x-ray cephalogram indicates the linear (A) and angular (B) measurements with significant differences between controls and *Evc2 P0* mutants. Lateral x-ray cephalogram indicates the linear (C) and angular (D) measurements with significant differences between controls and *Evc2 Wnt1* mutants. Graphs indicate the linear and angular values of the measurement with significant differences. (N=7; *, $p<0.05$; and **, $p<0.01$)

Table 4.2: Summary of phenotypic spectrums of *Evc2* global mutants, *P0* mutants and *Wnt1* mutants.

Orange box, significant differences detected in *Evc2 P0* mutants. Blue box, significant difference detected in *Evc2 Wnt1* mutants. Green box, significant differences detected in *Evc2* global mutants. Black box, not examined.

4.3.3 *Evc2 Wnt1* Mutants Showed More Aspects of Mid-Facial Defects than *Evc2 P0* Mutants at P28

Mouse cranial growth rate peaks and reaches 80% of its adult length within the first month [24, 25]. We therefore performed similar lateral cephalometric analyses at P28 but, unlike analyses at P8, observed more widespread craniofacial deficiencies in *Evc2 Wnt1* mutants compared to *Evc2 P0* mutants. In *Evc2 P0* mutants we found significant decreases in: viscerocranial length (E-Bu and E-Pr), distance between molar and incisor in maxilla (Mu-Pr), erupted upper incisor length (Pr-Iu), erupted lower incisor length (Id-Ii), length of anterior skull base (So-E), neurocranial length (Po-E), distance between the first molar to the most posterior point (Po-Mu), and total skull length (Po-A) (Figure 4.3A). The only significant angle difference was a decreased angle of cranial vault (ABrL/PoBrL) in the *Evc2 P0* mutants (Figure 4.3 B).

In contrast to the *Evc2 P0* mutants, *Evc2 Wnt1* mutants at P28 displayed a more severe and widespread decreases in their craniofacial linear measurements. We found significant decreases in nasal bone length (A-N), nasal bone height (E-Mu), viscerocranial length (E-Bu) and (E-Pr), relative position of pre-maxilla to cranium (N-Pr), distance between molar and incisor in maxilla (Mu-Pr), palatal length (Mu-Bu), length of anterior cranial base (So-E), neurocranial length (Po-E), length of posterior cranium (Po-Br), and total skull length (Po-A). Similar to *Evc2 Wnt1* mutants at P8, we also observed shortened erupted upper (Pr-Iu) and lower (Id-Ii) incisors, and decreased distance between molar and incisor in mandible (Ml-Ii) (Figure 4.3 C). Consistent with the slanted mid-facial region in the gross morphologic observations, we also detected decreased angle measures of nasal bone to cranial base (ANL/SoEL), premaxilla to cranial base (PrEL/SoEL), premaxilla to cranial vault (BuEL/PoEL), and the angle of the cranial vault (ABrL/PoBrL), respectively (Figure 4.3 D). Overall, *Evc2 Wnt1* mutants showed severely affected

mid-facial bones and a more slanted mid-facial region at P28 when compared to both control and *Evc2 P0* mutant counterparts.

In Table 4.2, a series of linear and angular defects detected in *Evc2 P0* mutants and *Evc2 Wnt1* mutants (present study) are compared with those found in *Evc2* global mutants [18, 19]. At P7/P8, comparisons in linear measurements revealed that all tooth-associated abnormalities detected in *Evc2 P0* mutants and *Evc2 Wnt1* mutants were also detected in the *Evc2* global mutants. Additionally, nasal bone length (A-N), viscerocranial height (E-Mu), and mandibular lingual alveolar bone length (Ml-Bl) were significantly shorter in the *Evc2* global mutants than in controls, whereas these characteristics were normal in both *Evc2 Wnt1* mutants and *Evc2 P0* mutants. In the angular measurements, we found that lower incisor inclination (MlIiL/IdIiL) and upper incisor inclination (MuPrL/PrIuL) were increased in the *Evc2 P0* mutants and *Evc2 Wnt1* mutants but not in the *Evc2* global mutants. At P21/P28, all linear measurement differences detected in *Evc2 Wnt1* mutants were detected in *Evc2* global mutants. Of these, decreased palatal length (Mu-Bu) and length of posterior cranium (Po-Br) were not detected in the *Evc2 P0* mutants. These results reflect subtle phenotypic dissimilarities between mutants at P28 that are not apparent at P8. In the P28 angular measurements, we found that defective nasal bone to cranial vault (ANL/PoEL), maxilla-premaxilla to cranial base (MuBuL/PoEL), and upper incisor to cranial vault in *Evc2 P0* mutants, but not in the *Evc2 Wnt1* mutants, whereas defective upper incisor inclination (MuPrL/PrIuL) and lower incisor inclination (MlIiL/IdIiL) was observed in the *Evc2 Wnt1* mutants but not in the *Evc2* global mutants. Except for the decreased angle of cranial vault (ABrL/PoBrL), there were no other angular differences detected in the *Evc2 P0* mutants.

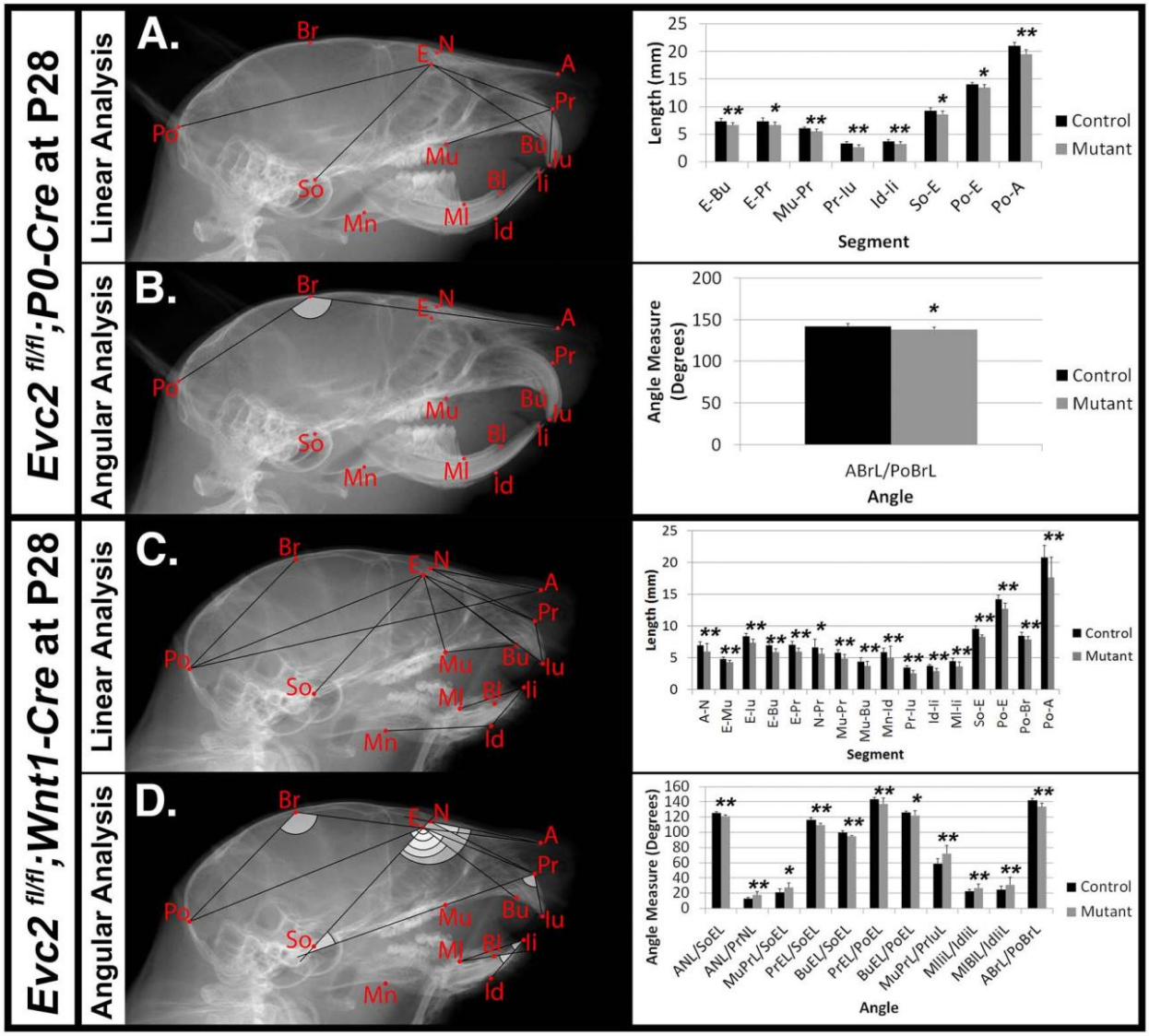

Figure 4.3: Differential mid-facial defects between *Evc2 P0* mutants and *Evc2 Wnt1* mutants at P28.

Lateral X-ray cephalogram indicates the linear (A) and angular (B) measurements with significant differences between controls and *Evc2 P0* mutants. Lateral x-ray cephalogram indicates the linear (C) and angular (D) measurements with significant differences between controls and *Evc2 Wnt1* mutants. Graphs indicate the linear and angular values of the measurement with significant differences. (N=7; *, $p<0.05$; and **, $p<0.01$)

4.3.4 Loss of *Evc2* Expression in Neural Crest-Derived Cells Severely Affects Head Shape and Mid-Facial Bone Shapes

Particularly at P28, *Evc2 P0* mutants showed very limited angular defects. To better appreciate the impacts of *Evc2* mutation on the overall skull shape at P28, we: 1) generated 3D

surface models from micro-CT data for the midline portion of the controls, *Evc2 P0* mutants, and *Evc2 Wnt1* mutants at P28 and 2) registered the skulls at the most posterior region (Figure 4.4 A). Registration of each pair of skulls revealed nearly no shape differences in the interparietal and basioccipital bones (*i.e.* tissues negative for neither *P0-Cre* nor *Wnt1-Cre* expression). When we individually superimposed nasal, frontal and parietal, respectively, bones, respectively, using *Evc2 P0* mutants and *Evc2 Wnt1* mutants with corresponding controls, we did not see noticeable size differences (Figure 4.4 B). This suggests that there was no overt overall growth retardation since general growth retardation would affect all bones. Morphometric comparison, however, revealed mutant-specific structural differences. *Evc2 Wnt1* mutants had a more shortened and downward-angled facial region than *Evc2 P0* mutants (Figure 4.4 A). Since the skull base connects the facial region with the posterior part of the skull, the extent of skull base linear differences may directly result in angular measurement differences in *Evc2 Wnt1* and *Evc2 P0* mutants, respectively. To visualize the potential shape or scaling differences within each individual bone, we digitally extracted nasal, frontal, and parietal bones separately and superimposed control surface models with corresponding mutant samples (Figure 4.4 B). Superimpositions of individual bones revealed shape differences in all nasal, frontal, and parietal bones (Figure 4.4 B). Most strikingly, in the parietal bones (non-neural crest derived), we detected deviations in the anterior regions, in which the mutant surfaces "stuck out" of the control surfaces (red color in Figure 4.4 B). *Evc2 Wnt1* mutants have more severely affected parietal bones than *Evc2 P0* mutants. Three other mutant skulls from each mutant group showed similar patterns when compared with littermate controls (Figure 4.7). When we compared four littermate controls within the *Evc2 P0* mutant group or four littermate controls within the *Evc2 Wnt1* mutant group using the same standard, almost all areas showed green color indicating that surface structures of those bones are highly consistent among

controls (Figure 4.7, one pair of comparison for each group is shown). The defective skull bones in *Evc2* mutants likely reflect the shortened skull base and resultant shortened and downward-angled mid-facial region. Therefore, the more severely affected parietal bones in the *Evc2 Wnt1* mutants (compared to *Evc2 P0* mutants) are likely due to the more severely affected skull base in these mutants, as previously discussed (Table 4.2).

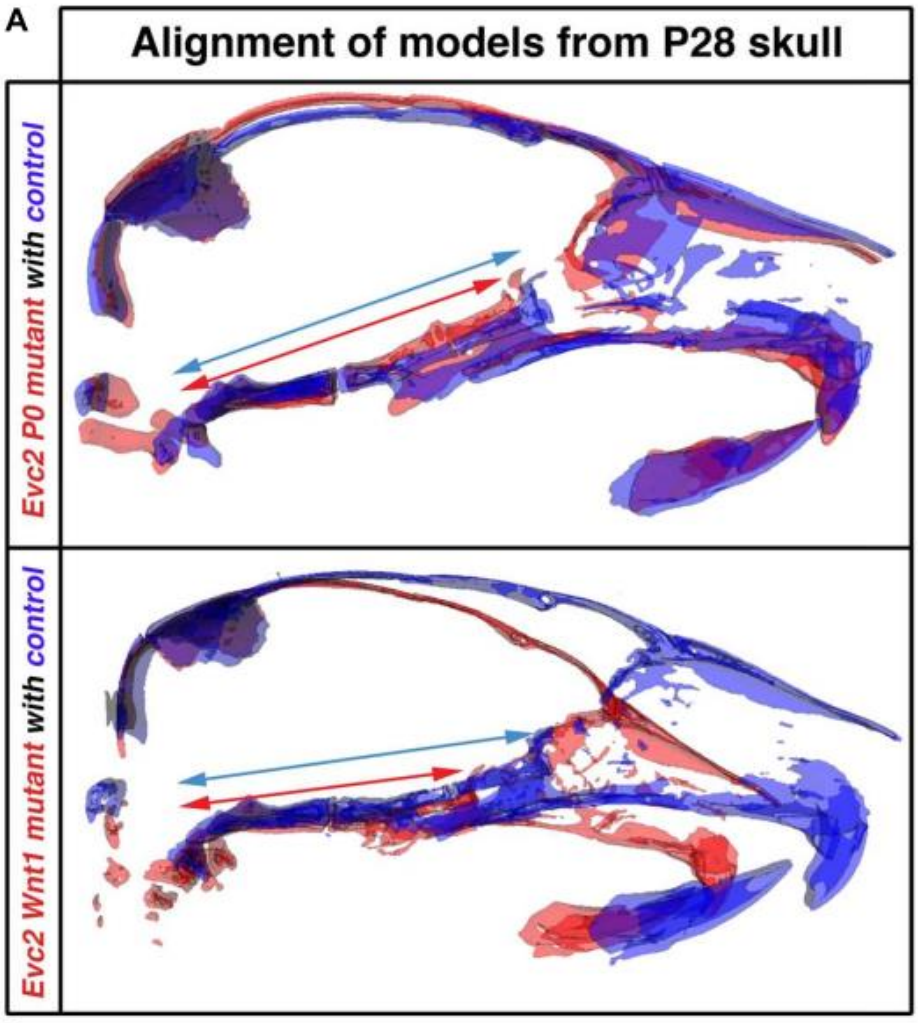
A
Alignment of models from P28 skull
Evc2 P0 mutant with control
Evc2 Wnt1 mutant with control

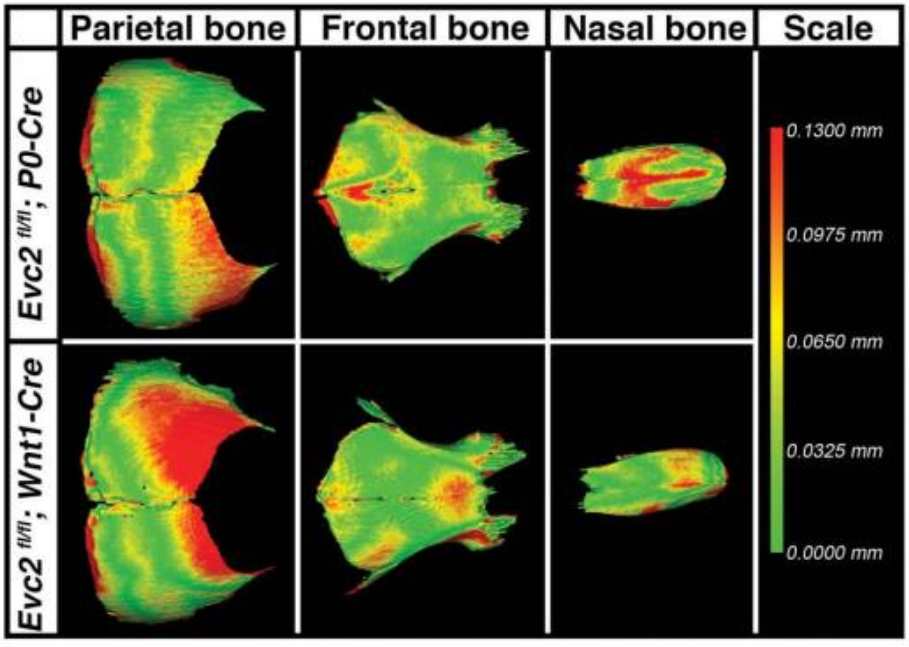
B
Parietal bone
Frontal bone
Nasal bone
Scale
Evc2 fl/fl; P0-Cre
Evc2 fl/fl; Wnt1-Cre
0.1300 mm
0.0975 mm
0.0650 mm
0.0325 mm
0.0000 mm

Figure 4.4: *Evc2 cKO* mutants demonstrate skull shape and mid-facial shape differences. A. Mid-sagittal planes were generated based on the micro-CT scans of the controls (Blue), *Evc2 P0* mutants (red) and *Evc2 Wnt1* mutants (red). Models of skulls from mutants and corresponding controls were then superimposed at the occipital bones of the skull. Blue and red arrows are spanning the entire regions of the skull bases in controls and mutants respectively. B. Nasal, frontal and parietal bones from P28 *Evc2* P0 mutants and *Evc2 Wnt1* mutants were superimposed with corresponding skull bones from P28 controls. Pictures shown represent comparisons within indicated mutants with corresponding controls. Color indicates the distances the mutants bone surface protruding out of the control surface at the indicated region.

4.3.5 The Differential Early Fusion of the Presphenoidal Synchondrosis Leads to the Differentially Shortened Skull Base in *Evc2 P0* and *Evc2 Wnt1* Mutants

The skull base is a unique structure that connects multiple bones in the skull and has a significant influence on facial growth, particularly in the mid-facial region [26]. Our studies demonstrated that *Evc2* is expressed in both intersphenoidal synchondrosis (ISS) and the spheno-occipital synchondrosis (SOS) (Figure 4.8). Quantification of the skull base length revealed that, compared to controls, skull bases from *Evc2 Wnt1* mutants are 20% shorter while skull bases from *Evc2 P0* mutants are only 10% shorter at P28 (Figure 4.5 B, C, D and E, $n=5$, $p<0.01$). Elongation of the skull base is supported by the endochondral ossification within the ISS and the SOS. To investigate whether the abnormal ISS or SOS is the cause of the affected skull base elongation in either *Evc2 P0* or *Evc2 Wnt1* mutants, we generated surface models from the skull bases of *Evc2 P0* and *Evc2 Wnt1* mutants respectively. At P28, we observed premature fusion of ISS in both *Evc2 P0* and *Evc2 Wnt1* mutants (Figure 4.5 B and C). However, at P8, we observed premature fusion of ISS in *Evc2 Wnt1* mutants and partial fusion of ISS in the *Evc2 P0* mutants (Figure 4.5 B and C). These results suggest that the premature fusion of the ISS in *Evc2 P0* mutants happens between P8 and P28, while the premature fusion of ISS in *Evc2 Wnt1* happens before P8 (Figure 4.5 C).

The anterior regions of the skull base are derived from neural crest cells and are the active sites for postnatal skull base elongation [26]. To examine if differential skull base lengths in *Evc2 P0* mutants and *Evc2 Wnt1* mutants result from differential Cre recombination efficiency in the anterior part of the skull base, we examined the Cre recombined cells in the anterior region of the skull base. At E18.5, while *P0-Cre* leads to sporadic recombination within the chondrocytes in the anterior part of the skull base, *Wnt1-Cre* leads to nearly 100% recombination in the chondrocytes in the same region (Figure 4.6). These results suggest that 1) *Evc2* function within the ISS is critical for maintaining the ISS and supporting the elongation of skull base; and that 2) differential *Evc2* deletion efficiency mediated by *P0-Cre* and *Wnt1-Cre* leads to differential impacts upon skull base elongation, which secondarily affects differential outcomes in mid-facial abnormalities between *P0-Cre* and *Wnt1-Cre* mutants.

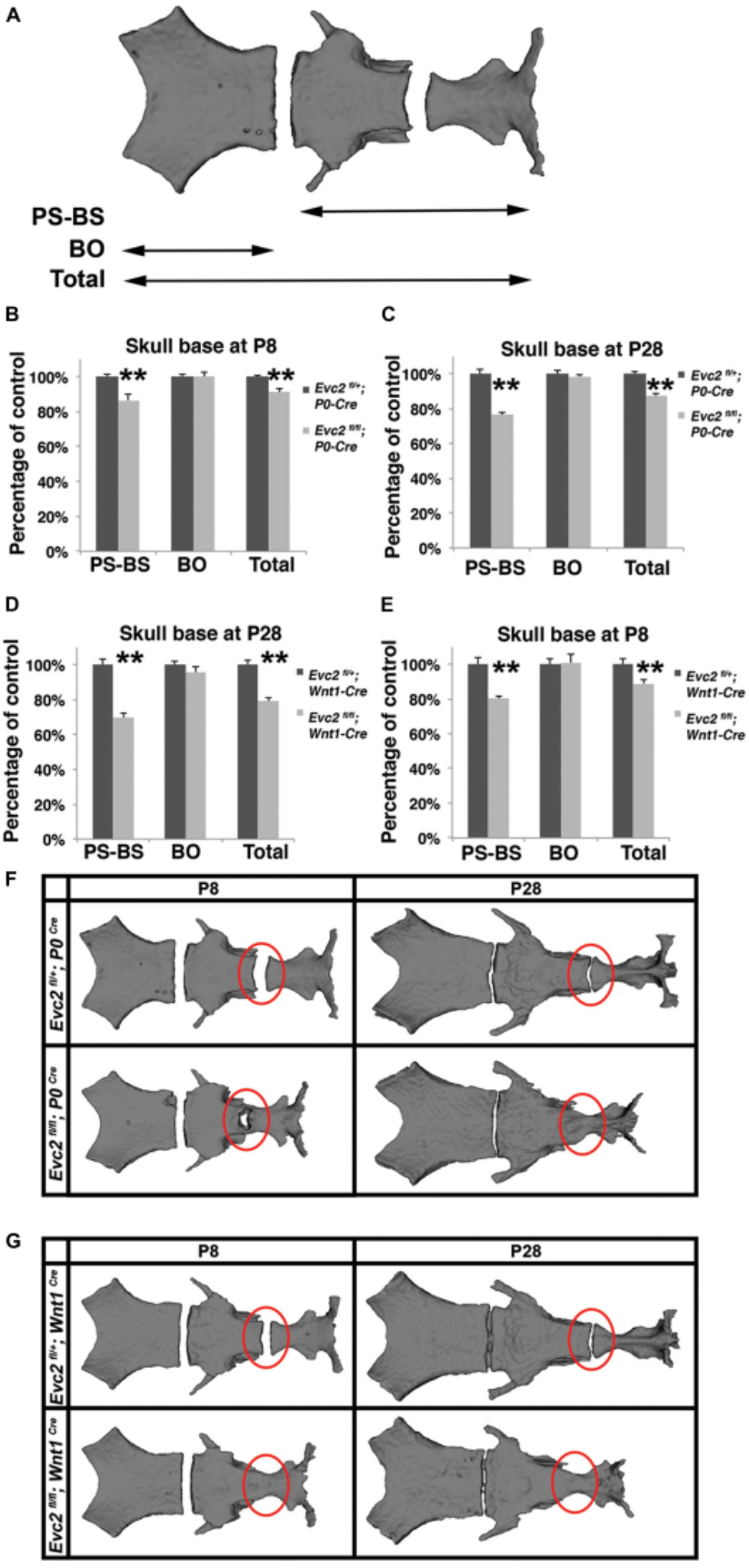
A
PS-BS
BO
Total
B
Skull base at P8
Percentage of control
100%
80%
60%
40%
20%
0%
PS-BS
BO
Total
**
Evc2 fl/+; P0-Cre
Evc2 fl/fl; P0-Cre
C
Skull base at P28
Evc2 fl/+; P0-Cre
Evc2 fl/fl; P0-Cre
D
Skull base at P28
Evc2 fl/+; Wnt1-Cre
Evc2 fl/fl; Wnt1-Cre
E
Skull base at P8
Evc2 fl/+; Wnt1-Cre
Evc2 fl/fl; Wnt1-Cre
F
P8
P28
Evc2 fl/+; P0 Cre
Evc2 fl/fl; P0 Cre
G
P8
P28
Evc2 fl/+; Wnt1 Cre
Evc2 fl/fl; Wnt1 Cre

Figure 4.5: Evc2 mutants have defective skull bases.
A. Diagram of measurements in B, C, D and E. Quantification of skull base length at P8 (B and D) and P28 (C and E). The length of the skull base was determined by assessing the linear distance shown in A. (N=5; **, $p<0.01$ comparing to controls). Surface models of skull bases were generated based on micro-CT scans of P28 (F) and P8 samples (G). Red cycles indicating the ISS or fused ISS.

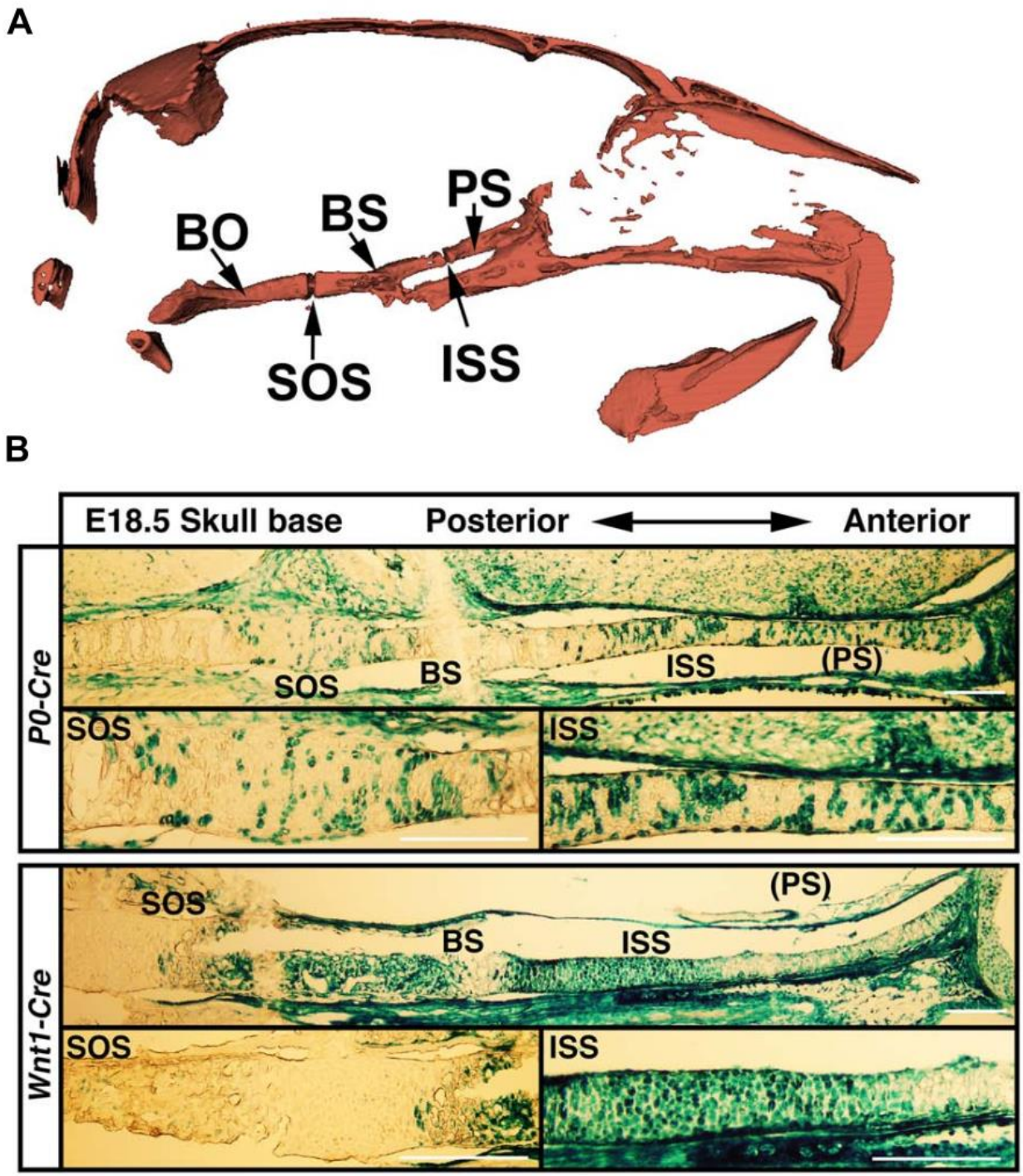

Figure 4.6: Evc2 mutant skull base structure.
A. Diagram to skull base structure. B. Differential Cre-dependent recombination in the skull bases of *P0* and *Wnt1* Cre lines. Indicated Cre mice were crossed with Rosa26-LacZ Cre reporter mice, followed by beta-galactosidase activity staining to visualize the Cre recombinant cells in the skull base. PS, Presphenoid bone; ISS, intersphenoidal synchondrosis; BS, Basiosphenoid bone; SOS, Spheno-occipital synchondrosis. Scale bar = 100 μm.

4.4 Discussion

Craniofacial abnormalities have been reported in EvC patients [1, 9, 12, 13]. Despite our recent studies describing mouse models that recapitulate the craniofacial abnormalities of EvC patients [19], the underlying pathophysiological mechanisms of these abnormalities remain largely unknown. In this study, we deleted *Evc2* in the neural crest derived cells using *P0-Cre* and *Wnt1-Cre*. While both of these Cre lines equally target the mid-facial region, they differentially target the anterior region of the skull base. Comprehensive analysis of these two types of *Evc2* mutant lines allows us to delineate the craniofacial abnormalities due to *Evc2* loss of function in the neural crest derived tissues and the secondary abnormalities due to the affected skull base. The results here are potentially applicable to understand postnatal mid-facial development in other types of ciliopathies.

Compared to their global mutant counterparts, we believe that two types of *Evc2* cKO mice, *Evc2 P0* mutants and *Evc2 Wnt1* mutants, are great tools in helping to elucidate the pathological mechanism leading to the mid-facial defects. Our phenotypic analysis at P8 and P28 indicated that mid-facial defects were recapitulated in *Evc2 Wnt1* mutants, but less extent in *Evc2 P0* mutants. The *Evc2 P0* mutants show a smaller head (Figure 4.1 A, 2nd row) and differences in some of the parameters (Figure 4.2 A,B) at P8, which are consistent with our previous report [20]. However, many of the differences are compensated by P28 (Figure 4.1 B, 2nd row and Figure 4.3 A,B). In contrast, the *Evc2 Wnt1* mutants show comparable size of a head at P8 but become smaller at P28 (Figure 4.1 A,B, 4th row), and more parameters show differences at P28 than P8 (Figure 4.2 C,D and Figure 4.3 C,D). Those facts strongly suggest that tissues that are specifically positive for *Wnt1*-Cre mediated recombination play a critical role for post-natal mid-facial development. Considering the impacts of shortened skull base on the mid-facial region as shown in Figure 4.4

A and that loss of *Evc2* leads to early fusion of ISS in *Evc2 Wnt1* mutants, we believe that the differential *Evc2* deletion efficiency mediated by *P0-Cre* and *Wnt1-Cre* at the anterior region of the skull base is a major reason leading to the differential mid-facial defects in these two types of *Evc2* cKO mice.

Differential phenotypic differences between *Evc2* global mutants, *Evc2 P0* mutants and *Evc2 Wnt1* mutants suggest that different pathological mechanisms lead to various craniofacial defects due to *Evc2* mutations. For example, viscerocranial length (E-Bu and E-Pr), erupted upper incisor length (Pr-Iu), erupted lower incisor length (Id-Ii), cranial base length (So-E) are due to the *Evc2* loss of function within the neural crest cells. In contrast, the nasal bone to cranial base (ANL/SoEL), nasal bone to premaxilla (ANL/PrNL), premaxilla to cranial base (PrEL/SoEL), upper incisors to cranial base (BuEL/SoEL), premaxilla to cranial vault (PrEL/PoEL), premaxilla to cranial vault (BuEL/PoEL), upper incisor inclination (MuPrL/PrIuL), lower incisor inclination and (MlIiL/IdIiL), are due to the unique spatial activity of the *Wnt1-Cre* driver. Since the skull base connects the posterior and mid-facial regions, the shortened skull base is a well-known cause of mid-facial defects [24, 26]. Therefore, our data suggest that the differential Cre recombination efficiency mediated by the *Wnt1-Cre* and *P0-Cre* lineage cells within the anterior part of the skull base leads to the differential impacts on the pre-mature fusion of ISS and the length of the skull base, which secondarily leads to the shortened and downward-angled facial defects observed in the *Evc2 Wnt1* mutants.

Similar to the appendicular bones, the skull base develops through endochondral ossification, wherein the cartilage primordium forms first, followed by mineral deposition. The proliferation and maturation of chondrocytes at the synchondrosis in the skull base is quite important for skull base elongation [26]. In this study, we found loss of function of *Evc2* results in

premature closure of the ISS, which connects the presphenoid bone and the basisphenoid bone, before P8 in *Evc2* global mutant and in *Evc2 Wnt1* mutant. We previously reported that loss of function of *Evc2* results in severe chondrodysplastic dwarfism; however, we never observed premature closure of appendicular growth plates through adult stages [16]. Those data suggest that a function of *Evc2* to maintain cartilage is different between appendicular growth plates and synchondroses. A potential mechanism leading to the premature fusion of ISS is a subject under active investigation.

In this study, we used both *P0-Cre* and *Wnt1-Cre* to specifically delete *Evc2* in the neural crest derived cells. Despite largely overlapping targeted regions within the facial regions of *P0-Cre* and *Wnt1-Cre* [21, 22] (our own comparisons, data not shown), small differences have been noticed between those Cre lines by multiple studies [27-30]. Particularly, our recent studies demonstrated that both *P0-Cre* and *Wnt1-Cre* differentially target neural crest cells emerging at the anterior, middle and posterior portions of the head during embryogenesis [30]. Previously, we reported a neural crest-specific disruption of TGF-beta activating kinase 1 (*Tak1*) using *Wnt1-Cre* and *P0-Cre*, respectively [31, 32]. While *Tak1 P0* mutants do not show overt craniofacial phenotypes at the birth [31], *Tak1 Wnt1* mutants develop cleft palate secondarily to the micrognathia [32]. This is another example that *Wnt1-Cre* and *P0-Cre* result in distinctive phenotypes. In the current study, we identified that *P0-Cre* and *Wnt1-Cre* differentially target the anterior regions of the skull base, and we took advantage of those differences to identify the pathophysiological mechanism leading to the mid-facial defects in *Evc2* mutant mice. However, there is a formal possibility that the differential Cre activity within the unknown types of cells or tissues contributing to the differential mid-facial defects in *Evc2 P0* mutants and *Wnt1* mutants.

We will further investigate an involvement of the premature fusion of the ISS to the mid-facial defects in our mutant mouse models.

Wnt1-Cre is known to target the brain [21], while *P0*-Cre is not expressed in the central nervous system. However, it is unlikely that the differential mid-facial defects observed in the *Evc2 Wnt1* mutants and *Evc2 P0* mutants are secondary effects of the differential Cre targeting within the brain. Firstly, the mid-facial region is not in direct contact with the brain and thus brain development should not have an impact on the development of the mid-facial region. Secondly, despite the fact that *Evc2* is a positive regulator of Hedgehog signaling, there are no brain developmental defects observed in patients or mice. Recent studies also suggest that the transgenic construct in *Wnt1-Cre* mouse line transiently elevates WNT signaling during craniofacial development [33]. It is unlikely that this is the reason leading to differential mid-facial defects observed in the *Evc2 Wnt1* mutants and *Evc2 P0* mutants. Our analysis demonstrated that no overt head shape differences between *Evc2* $^{fl/+}$ and *Evc2* $^{fl/+}$*; Wnt1-Cre*, suggesting the transiently elevated WNT signaling due to *Wnt1-Cre* did not leads to craniofacial abnormalities.

By specifically deleting *Evc2* in neural crest-derived tissues, we were able to generate a mouse model of human EvC that recapitulates the mid-facial defects associated with EvC syndrome. Multiple analyses at different developmental stages confirm the critical role of the skull base during face elongation and development within the first month and demonstrate that the mid-facial defects in EvC syndrome are largely due to the premature fusion of the ISS in the skull base. Examination and targeting the shortened skull is therefore a suggested therapeutic option for the mid-facial defect in EvC patients.

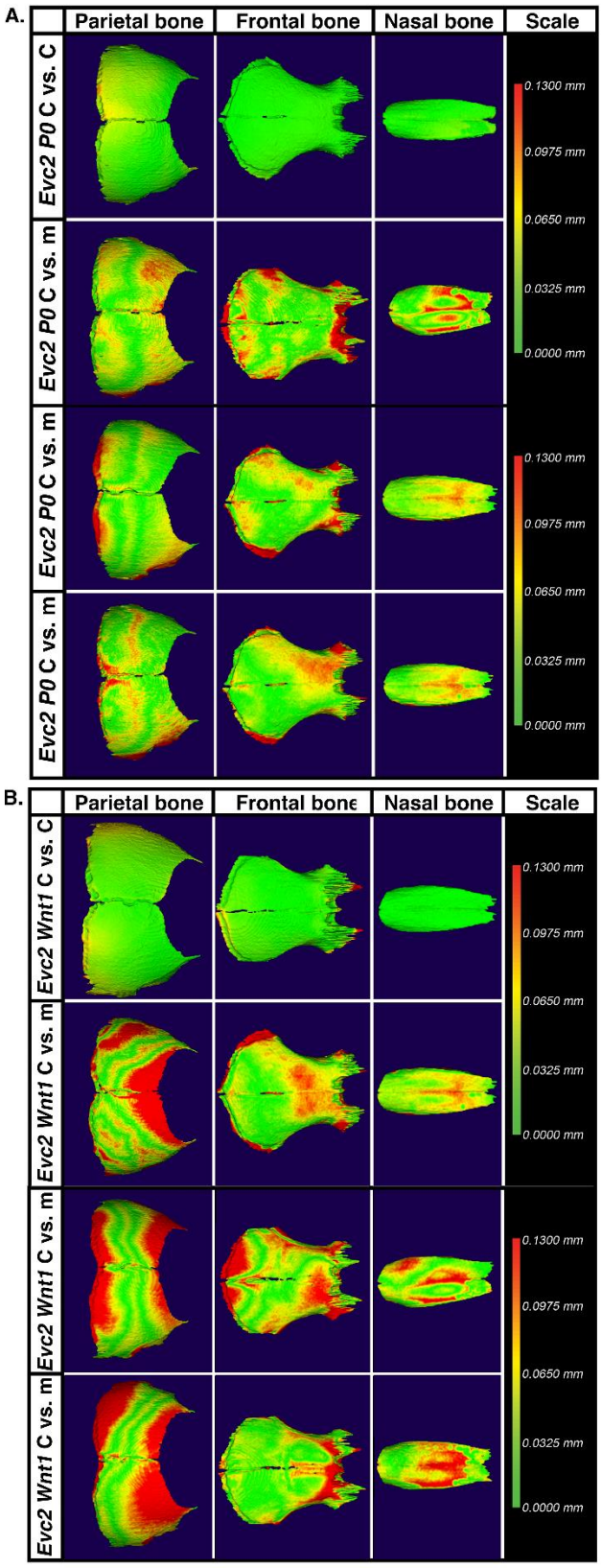

Figure 4.7: Skull bone superimposition.

A. Superimposition of each skull bones within the *Evc2 P0* group. Comparisons of two controls (*Evc2 P0* C vs. C) and three additional pairs of control and mutant (*Evc2 P0* C vs. m) are shown. B. Superimposition of each skull bones within the *Evc2 Wnt1* group. Comparisons of two controls (*Evc2 Wnt1* C vs. C) and three additional pairs of control and mutant (*Evc2 Wnt1* C vs. m) are shown.

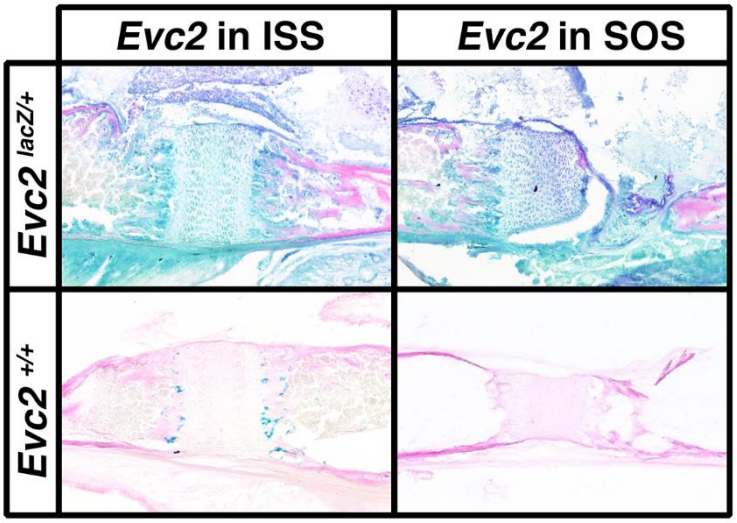

Figure 4.8: *Evc2* expression in synchondrosis in the skull base.
Beta-galactosidase activity from the *lacZ* knock-in allele of *Evc2* locus was used as a surrogate of the expression of *Evc2*. The skull bases from $Evc2^{lacZ/+}$ at P10 were stained with X-gal followed by eosin counter staining. Robust staining (blue) was detected in the ISS and the SOS. $Evc2^{+/+}$ littermates were used as negative controls.

4.5 References

1. McKusick VA, Egeland JA, Eldridge R, Krusen DE: Dwarfism in the Amish I. The Ellis-Van Creveld Syndrome. *Bull Johns Hopkins Hosp* 1964, 115:306-336.
2. Baujat G, Le Merrer M: Ellis-van Creveld syndrome. *Orphanet J Rare Dis* 2007, 2:27.
3. Ruiz-Perez VL, Tompson SW, Blair HJ, Espinoza-Valdez C, Lapunzina P, Silva EO, Hamel B, Gibbs JL, Young ID, Wright MJ *et al*: Mutations in two nonhomologous genes in a head-to-head configuration cause Ellis-van Creveld syndrome. *Am J Hum Genet* 2003, 72(3):728-732.
4. Andersen E, Sonnesen L, Kjaer MS, Fischer Hansen B, Kjaer I: The prenatal cranial base complex and hand in Turner syndrome. *Eur J Orthod* 2000, 22(2):185-194.
5. Caparros-Martin JA, Valencia M, Reytor E, Pacheco M, Fernandez M, Perez-Aytes A, Gean E, Lapunzina P, Peters H, Goodship JA *et al*: The ciliary Evc/Evc2 complex interacts with Smo and controls Hedgehog pathway activity in chondrocytes by regulating Sufu/Gli3 dissociation and Gli3 trafficking in primary cilia. *Hum Mol Genet* 2013, 22(1):124-139.
6. Dorn KV, Hughes CE, Rohatgi R: A Smoothened-Evc2 complex transduces the Hedgehog signal at primary cilia. *Dev Cell* 2012, 23(4):823-835.
7. Takeda H, Takami M, Oguni T, Tsuji T, Yoneda K, Sato H, Ihara N, Itoh T, Kata SR, Mishina Y *et al*: Positional cloning of the gene LIMBIN responsible for bovine chondrodysplastic dwarfism. *Proc Natl Acad Sci U S A* 2002, 99(16):10549-10554.
8. Murgiano L, Jagannathan V, Benazzi C, Bolcato M, Brunetti B, Muscatello LV, Dittmer K, Piffer C, Gentile A, Drogemuller C: Deletion in the EVC2 gene causes chondrodysplastic dwarfism in Tyrolean Grey cattle. *PLoS One* 2014, 9(4):e94861.
9. Ellis RW, van Creveld S: A Syndrome Characterized by Ectodermal Dysplasia, Polydactyly, Chondro-Dysplasia and Congenital Morbus Cordis: Report of Three Cases. *Arch Dis Child* 1940, 15(82):65-84.
10. da Silva EO, Janovitz D, de Albuquerque SC: Ellis-van Creveld syndrome: report of 15 cases in an inbred kindred. *J Med Genet* 1980, 17(5):349-356.
11. Varela M, Ramos C: Chondroectodermal dysplasia (Ellis-van Creveld syndrome): a case report. *Eur J Orthod* 1996, 18(4):313-318.
12. Eidelman E, Odont D, Rosenzweig KA: Ellis-Van Creveld Syndrome; Report of a Case. *Oral Surg Oral Med Oral Pathol* 1965, 20:174-179.
13. Prabhu SR, Daftary DK, Dholakia HM: Chondroectodermal dysplasia (Ellis-van Creveld syndrome): report of two cases. *J Oral Surg* 1978, 36(8):631-637.
14. Ruiz-Perez VL, Blair HJ, Rodriguez-Andres ME, Blanco MJ, Wilson A, Liu YN, Miles C, Peters H, Goodship JA: Evc is a positive mediator of Ihh-regulated bone growth that localises at the base of chondrocyte cilia. *Development* 2007, 134(16):2903-2912.
15. Zhang HH, Takeda H, Tsuji T, Kamiya N, Rajderkar S, Louie K, Collier C, Scott G, Ray M, Mochida Y *et al*: Generation of Evc2/Limbin Global and Conditional KO Mice and Its Roles during Mineralized Tissue Formation. *Genesis* 2015, 53(9):612-626.

16. Zhang HH, Kamiya N, Tsuji T, Takeda H, Scott G, Rajderkar S, Ray MK, Mochida Y, Allen B, Lefebvre V *et al*: Elevated Fibroblast Growth Factor Signaling Is Critical for the Pathogenesis of the Dwarfism in Evc2/Limbin Mutant Mice. *Plos Genetics* 2016, 12(12).
17. Zhang H, Takeda H, Tsuji T, Kamiya N, Kunieda T, Mochida Y, Mishina Y: Loss of Function of Evc2 in Dental Mesenchyme Leads to Hypomorphic Enamel. *J Dent Res* 2016:22034516683674.
18. Badri MK, Zhang H, Ohyama Y, Venkitapathi S, Alamoudi A, Kamiya N, Takeda H, Ray M, Scott G, Tsuji T *et al*: Expression of Evc2 in craniofacial tissues and craniofacial bone defects in Evc2 knockout mouse. *Arch Oral Biol* 2016, 68:142-152.
19. Badri MK, Zhang HH, Ohyama Y, Venkitapathi S, Kamiya N, Takeda H, Ray M, Scott G, Tsuji T, Kunieda T *et al*: Ellis Van Creveld2 is Required for Postnatal Craniofacial Bone Development. *Anatomical Record-Advances in Integrative Anatomy and Evolutionary Biology* 2016, 299(8):1110-1120.
20. Kwon EK, Louie K, Kulkarni A, Yatabe M, Ruellas ACO, Snider TN, Mochida Y, Cevidanes LHS, Mishina Y, Zhang H: The Role of Ellis-Van Creveld 2(EVC2) in Mice During Cranial Bone Development. *Anat Rec (Hoboken)* 2018, 301(1):46-55.
21. Danielian PS, Muccino D, Rowitch DH, Michael SK, McMahon AP: Modification of gene activity in mouse embryos in utero by a tamoxifen-inducible form of Cre recombinase. *Curr Biol* 1998, 8(24):1323-1326.
22. Yamauchi Y, Abe K, Mantani A, Hitoshi Y, Suzuki M, Osuzu F, Kuratani S, Yamamura K: A novel transgenic technique that allows specific marking of the neural crest cell lineage in mice. *Developmental Biology* 1999, 212(1):191-203.
23. Engstrom C, Linde A, Thilander B: Craniofacial morphology and growth in the rat. Cephalometric analysis of the effects of a low calcium and vitamin D-deficient diet. *Journal of anatomy* 1982, 134(Pt 2):299-314.
24. Vora SR, Camci ED, Cox TC: Postnatal Ontogeny of the Cranial Base and Craniofacial Skeleton in Male C57BL/6J Mice: A Reference Standard for Quantitative Analysis. *Front Physiol* 2015, 6:417.
25. Wei X, Thomas N, Hatch NE, Hu M, Liu F: Postnatal Craniofacial Skeletal Development of Female C57BL/6NCrl Mice. *Front Physiol* 2017, 8:697.
26. Nie X: Cranial base in craniofacial development: developmental features, influence on facial growth, anomaly, and molecular basis. *Acta Odontol Scand* 2005, 63(3):127-135.
27. Wang SK, Komatsu Y, Mishina Y: Potential contribution of neural crest cells to dental enamel formation. *Biochem Biophys Res Commun* 2011, 415(1):114-119.
28. Suzuki J, Yoshizaki K, Kobayashi T, Osumi N: Neural crest-derived horizontal basal cells as tissue stem cells in the adult olfactory epithelium. *Neurosci Res* 2013, 75(2):112-120.
29. Liu HX, Komatsu Y, Mishina Y, Mistretta CM: Neural crest contribution to lingual mesenchyme, epithelium and developing taste papillae and taste buds. *Developmental Biology* 2012, 368(2):294-303.
30. Chen GQ, Ishan M, Yang JW, Kishigami S, Fukuda T, Scott G, Ray MK, Sun CM, Chen SY, Komatsu Y *et al*: Specific and spatial labeling of P0-Cre versus Wnt1-Cre in cranial neural crest in early mouse embryos. *Genesis* 2017, 55(6).
31. Liu X, Hayano S, Pan H, Inagaki M, Ninomiya-Tsuji J, Sun H, Mishina Y: Compound mutations in Bmpr1a and Tak1 synergize facial deformities via increased cell death. *Genesis* 2018, 56(3):e23093.

32. Yumoto K, Thomas PS, Lane J, Matsuzaki K, Inagaki M, Ninomiya-Tsuji J, Scott GJ, Ray MK, Ishii M, Maxson R *et al*: TGF-beta-activated kinase 1 (Tak1) mediates agonist-induced Smad activation and linker region phosphorylation in embryonic craniofacial neural crest-derived cells. *J Biol Chem* 2013, 288(19):13467-13480.
33. Lewis AE, Vasudevan HN, O'Neill AK, Soriano P, Bush JO: The widely used Wnt1-Cre transgene causes developmental phenotypes by ectopic activation of Wnt signaling. *Developmental Biology* 2013, 379(2):229-234.

Chapter 5: Role of *Evc2/Limbin* on molar morphology and oral function

5.1 Introduction

As the gateway to the body, structural variation within the craniofacial region has significant health and nutritional impacts that extend beyond its anatomic boundaries. Dysfunction within this region requires functional adaptation or compensation for the sustenance of life and, long-term, confers increased risk of metabolic disorders that pose a significant clinical burden [1–3]. The impact of nutritional imbalance coupled with the high incidence of human craniofacial anomalies make the process of mastication a critical component when studying the functional and physiological outcomes of musculoskeletal disorders within this region [4]. Mastication is the rhythmic reduction of ingested food into smaller particles that maximize enzymatic interaction, digestive efficiency, and nutrient acquisition [5]. This process is uniquely a mammalian behavior that requires precise motor input and coordination of craniofacial musculature and components of the cranial system, specifically the jaws and teeth [6,7].

Ingested items represent conglomerates of non-uniform particle size and masticatory effectiveness is defined as the completeness with which a defined amount of material is reduced to a certain mean particle size [8]. Efficiency can be determined via a standardized wet sieve protocol that has been applied to studies involving numerous mammalian species [9,10]. Factors affecting efficiency include tooth anatomy and number as well as chewing force, duration, direction, and intensity. Studies have shown that greater efficiency, which is represented by a lower mean fecal particle size (FPS), is correlated with tooth number and surface area complexity (e.g., age-related attrition), factors also related to chewing frequency, bite force, food choice (e.g., soft

food preference), and longevity [1,7,8,11–13]. While many of these variables can be measured and controlled for in a laboratory setting, FPS represents a conveniently non-invasive alternative for assessing efficiency. Unlike digesta (i.e., food within the stomach that has not entered the intestines), fecal material has passed through the entire digestive tract and has been exposed to additional changes. However, these changes are small and only significant when feeding on soft material (e.g., kelp) [14,15].

Ellis-van Creveld syndrome (EVC; MIM ID #225500) is a rare congenital disorder that significantly affects the craniofacial region. Although characterized by more conspicuous signs such as disproportionate dwarfism and postaxial polydactyly (e.g., 6-7 fingers per appendage), patients present with a dental phenotype that includes hypoplastic enamel, congenitally missing teeth (i.e., hypodontia), abnormally shaped teeth (e.g., taurodontic or bulbous teeth), and premature eruption and exfoliation [16–19]. Patients also develop a progressively abnormal craniofacial morphology which includes mandibular prognathism, maxillary deficiency, skeletal open bite, and prominent frontal bossing that gives patients a concave-shaped lateral profile. These individuals thus require extensive prosthodontic rehabilitation (e.g., dentures and implants) and orthodontic management beginning from a young age [20,21]. Despite craniofacial signs suggesting significantly impaired chewing efficiency, detailed descriptions of molar morphology and oral function in patients with EVC are limited.

Mouse models for EVC were developed by targeting orthologs of the two causative genes (i.e., *Evc* or *Evc2/Limbin*) and have been critical for providing insight into disease pathogenesis [22–26]. *Evc2/Limbin* is highly expressed in the skull base and facial skeleton (i.e., viscerocranium), both of which are derived from neural crest cells (NCCs) [26–28]. NCCs represent a special population of migratory cells that contribute to mineralized structures within

the craniofacial region and maintain their identity despite divergence from the ectoderm in early gastrulation [29]. NCC-specific conditional knockout animal models of *Evc2/Limbin* (referred to as *Evc2/Limbin*-cKO) have revealed that expression within these cells is important for determining craniofacial morphology, results in abnormal incisors reminiscent of those in EVC patients, and circumvents perinatal lethality issues seen in conventional or global knockout animal models [25,30,31]. Furthermore, muscles of mastication are not derived from NCCs [32] suggesting that functional deficits are fundamental outcomes of dysmorphology in NCC-derived structures. Whether NCC-driven anatomic variation results in oral functional alteration and deficiency has yet to be investigated and is necessary to both broaden our understanding of functional disease outcomes and further the utility of *Evc2/Limbin*-cKO as a model of human disease.

In this study, we report molar dysmorphology and chewing functional deficits in NCC-specific *Evc2/Limbin*-cKO mice. Despite no change in the total number of molars, those present in *Evc2/Limbin*-cKO mice were taurodontic and had less complex coronal anatomy. These dental morphologic findings complement our previous craniofacial observations and, collectively, recapitulate signs seen in patients with EVC. Chewing functional metrics such as chewing rate and bite force were also reduced in *Evc2/Limbin*-cKO mice. However, despite evidence to suggest reduced chewing efficiency, average FPS was not different between *Evc2/Limbin*-cKO mice and their control counterparts. These findings suggest the presence of an adaptive mechanism that compensates for fundamental shortcomings in craniofacial and dental morphology.

5.2 Materials and Methods

5.2.1 Animal Model

All animals and experiments were performed in accordance with the policies and federal laws for the judicious use of vertebrate animals, as approved by the Institutional Animal Care and Use Committee at the University of Michigan. *Evc2/Limbin* floxed mice were generated by our group and reported previously [33]. Neural crest cell (NCC)-specific conditional knockout mice for *Evc2/Limbin* (referred to as *Evc2/Limbin*-cKO) were created by crossing *Evc2/Limbin* floxed mice with *Wnt1-Cre* mice[34]. "Control" animals did not have *Evc2/Limbin* homozygous deletions (i.e., $Evc2^{fx/+}$;$Wnt1^{(-)}$, $Evc2^{fx/fx}$;$Wnt1^{(-)}$, or $Evc2^{fx/+}$;$Wnt1^{(+)}$) and were compared against their *Evc2/Limbin*-cKO (i.e., $Evc2^{fx/fx}$;$Wnt1^{(+)}$) littermates. Analyses were performed at postnatal days P28, P42, P66, and P120.

5.2.2 µCT Imaging

Micro-CT scanning of fixed heads was performed at the University of Michigan using a Micro-CT core (µCT40 Scanco Medical, Bassersdorf, Switzerland). Scan settings were the following: voxel size 18µm, 55kVp, 109µA, 0.5mm AL filter, and integration time 500ms.

5.2.3 Image Segmentation and Analysis

Structures of interest were segmented and converted to 3D mesh models from µCT data using ITK-SNAP (itksnap.org, open source software developed by grants and contracts from the United States National Institutes of Health). Individual molar linear measurements (i.e., mesiodistal length, buccolingual width, incisocervical length) and volumes were divided into coronal and radicular segments using the cementoenamel junction (CEJ) as a boundary. Incisocervical length, mesiodistal length, buccolingual width, and linear distances between landmarks (Tables 5.1 and 5.2) were computed using the "CMF Reg tool" and "Q3DC tool"

developed in 3D Slicer (slicer.org, open source software). Molar occlusal surface areas, defined as all suprabulge polygons visible from the coronal view, were acquired and computed in MeshLab (Institute of Information Science and Technologies, Pisa, Italy). Normalized occlusal surface area (S_n) was calculated as follows:

$$S_n = S_m / S_s$$

S_m represents the surface area (mm^2) of all suprabulge surface polygons of a single molar. S_s represents the surface area of a sphere with the same volume as a molar's crown. Using the known volume (V_m; mm^3) of the molar crown:

$$S_s = 4\pi * (3/4\pi)^{2/3} * (V_m)^{2/3} \approx 0.0796 * (V_m)^{2/3}$$

Table 5.1: Landmarks and Descriptions Used for Linear Analysis

Landmarks		Description
Upper Jaw	Bu	Point on the premaxilla between the jaw bone and the lingual surface of the upper incisors
	Mu	Point on the intersection between the maxillary bone and mesial surface of the upper first molar
	U1	Point on the mesial occlusal fossa of the upper first molar
	U3	Point on the distal occlusal fossa of the upper third molar
	U4	Point on the intersection between the maxillary bone and distal surface of the upper third molar
	Mf	Center of the mandibular fossa in the temporal bone
Lower Jaw	Ml	Point on the intersection between the mandibular alveolar bone and the mesial surface of the first molar
	Bl	Point on the intersection between the lingual surface of the lower incisors and the most anterior part of the lingual alveolar bone
	Gn	Point on the most inferior contour of the angular process of the mandible
	Go	The most posterior point on the angular process of the mandible
	L1	Point on the mesial occlusal fossa of the lower first molar
	L3	Point on the distal occlusal fossa of the lower third molar
	L4	Point on the intersection between the mandibular bone and the distal surface of the lower third molar
	Cd	Center of the condylar head

Table 5.2: Segments and Descriptions Used for Linear Analysis

Landmarks		Segment
Upper Jaw	Mu-Bu	Palatal length
	Mf-Mu	Length of longest maxillary tooth lever
	Mf-U4	Length of shortest maxillary tooth lever
	Mf-Bu	Effective upper jaw length
	U1-U3	Length of upper occlusal table
Lower Jaw	Ml-Bl	Mandibular lingual alveolar bone length
	Go-Ml	Length of longest mandibular tooth lever
	Go-L4	Length of shortest mandibular tooth lever
	Go-Bl	Effective mandibular length
	L1-L3	Length of lower occlusal table
	Cd-Gn	Mandibular height

5.2.4 Fluoroscopic Recording

Sterilized 0.25mm diameter spherical tantalum markers (Bal-Tec, Los Angeles, CA, USA) were implanted in the cranium and jaw while animals were under general anesthesia (1-5% isoflurane with balanced O_2). Briefly, indentations were made using saline irrigation and a dental handpiece (1500rpm maximum) equipped with a 0.25mm round carbide bur. Markers were then

seated within the indentations and immobilized using Vetbond (3M, St. Paul, MN, USA). Animals were given an intramuscular injection of carprofen (5mg/kg) following surgery and monitored daily through 7 days post-surgery for signs of discomfort (e.g., scruffy appearance and/or lethargy) and suture hygiene.

High-speed biplanar fluoroscopy was recorded at 250 frames/s using two synchronized high-speed video cameras (Oqus 310; Qualisys, Göteborg, Sweden) mounted on the output ports of two fluoroscopes [OEC-9000 (General Electrics, Boston, MA, USA) refurbished by Radiological Imaging Services (Hamburg, PA, USA)]. On average, radiation exposures were set at 80 kVp and 4.5 mA to provide sufficient contrast between markers and bones. Recordings were initiated upon the start of chewing and lasted ~10s. Replicate recordings were captured a minimum of 1 hour after initial radiation exposure, after which animals were euthanized via CO_2 overdose followed by bilateral pneumothorax.

5.2.5 High Speed Video Acquisition

High-speed video from the sagittal view was recorded at 300 frames/s using a digital camera (EX-F1; Casio, Tokyo, Japan). Recordings were initiated upon the start of chewing and lasted 10s. Replicate recordings were captured a minimum of 1 hour after initial data acquisition.

5.2.6 Chewing Frequency Determination

Chewing frequency was determined from either high-speed fluoroscopic (see Section 5.2.4) or digital recordings (see Section 5.2.5) using either XMALab (open source software developed by grants and contracts from the United States National Science Foundation) or Kinovea (kinovea.org, open source software), respectively. Chew cycles were defined by the period of time or number of frames between maximum jaw openings; single chews were omitted from analysis.

Bursts of >3 rhythmic chews and no less than 15 chews/trial were used to calculate mean chewing frequency per animal.

5.2.7 Bite Force Measurement

Bite force was recorded using a piezo electric force transducer (model 9203, Amherst, NY, USA) mounted between two parallel steel plates separated by 0.5-1 mm and attached to an amplifier (model 5995, Kistler). The transducer was calibrated prior to each trial session to ensure linear readings across its entire range. Briefly, hand-restrained mice were brought into proximity of the parallel bite plates which they readily and rhythmically bit. Maximal bite force readings were extracted using LabChart 8 (ADInstruments, Colorado Springs, CO, USA). Animals were given 15 minutes of rest between replicate trials.

5.2.8 Food Processing Rate

Food processing rate was defined as the amount of time needed to ingest food (i.e., single autoclaved, unsalted sunflower seed) of a given mass. Time recording was initiated upon the start of visible food processing and continued until either: (1) the seed was completely consumed or (2) a total time of 5 minutes, after which remaining material was collected and weighed. Trials per tested individual were scored as either “finished” (i.e., seed completely consumed within the 5 minutes) or “not finished” (i.e., seed partially consumed with material remaining after 5 minutes).

5.2.9 Fecal Particle Sorting

Fecal samples collected over the course of 1 week from mice fed a standard chow diet (LabDiet, St. Louis, MO, USA), were stored at 4°C until sorting and analysis. Briefly, samples were desiccated at 103°C overnight then rehydrated in water under gentle agitation (55rpm on Lab-Line orbital shaker; Barnstead, Dubuque, IA, USA) for 3 hours. Rehydrated samples were

then rinsed with water at a rate of 2L/min through wire mesh sieves [pore sequence (μm): 2000-850-425-250-125-63-32] placed on a sieve shaker (Performer III SS-3, Gilson, Lewis Center, OH, USA) for 15 minutes. Sorted samples were again dried at 103°C overnight before final weighing. Mean fecal particle size was calculated according to the Fritz *et al.* 2012:

$$\text{dMEAN} = \sum_{i=1}^{n} p(i) * \frac{S(i+1)+S(i)}{2}$$

Sieves are ordered from size $S(1)$ (minimum) up to $S(n)$ (maximum pore size). Because the proportion of dried material p(i) retained on a sieve includes particles smaller than $S(n+1)$ but larger than $S(n)$, particles on $S(n)$ were converted to an average between $S(n)$ and $S(n+1)$.

5.2.10 Statistical Analysis

Comparisons between 2 groups were analyzed by Student t-test (*p < 0.05; **p < 0.01; ***p < 0.001, **** p< 0.0001). All tests were performed using the statistical software Microsoft Excel 2011 (Microsoft, Redmond, WA, USA).

5.3 Results

5.3.1 Molar numbers are unchanged in *Evc2/Limbin*-cKO mice

Neural crest-specific disruption of *Evc2/Limbin* does not affect the number of molars (i.e., 3) per quadrant in *Evc2/Limbin*-cKO mice (Figure 5.1 A). Both maxillary and mandibular molars were aligned along a clear occlusal plane and were positioned appropriately (i.e., mandibular molars approximately ½ tooth length ahead of maxillary molars) so that none were expected to be unopposed during mastication. However, 2 of 5 *Evc2/Limbin*-cKO mice analyzed at postnatal day P28 exhibited unilateral fusion of the first 2 molars in either the mandibular or maxillary arch

(Figure 5.1 B). These observations suggest that any changes in chewing performance in *Evc2/Limbin*-cKO mice would reflect finer scale differences in tooth morphology as opposed to macro, or whole tooth, level changes.

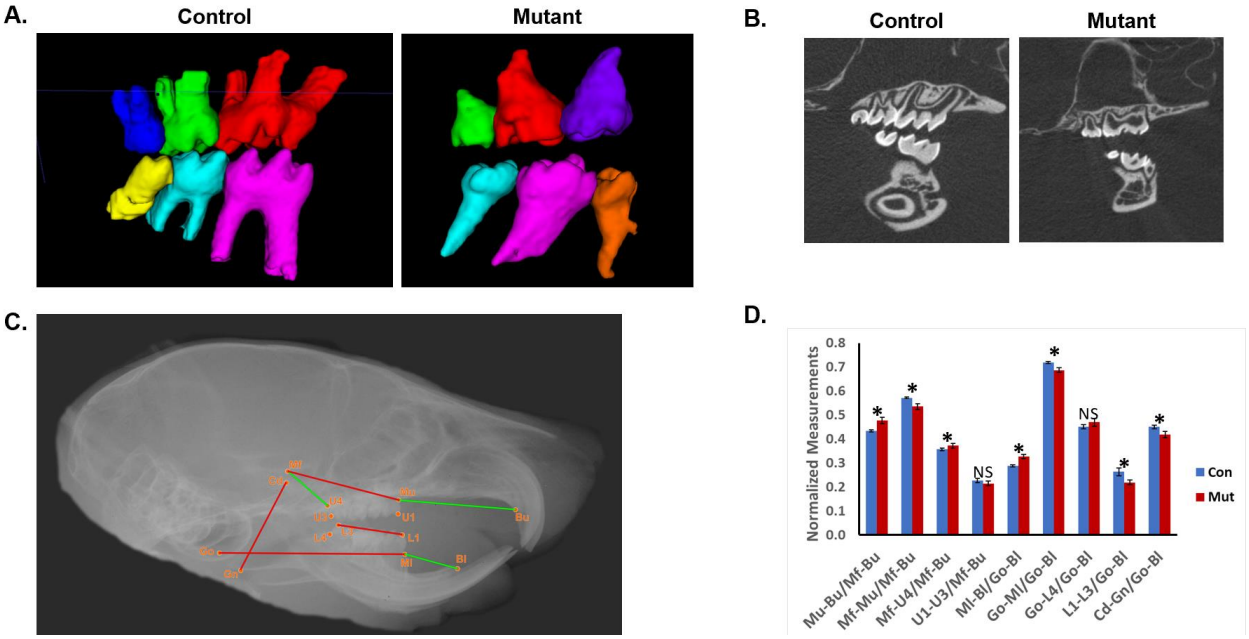

Figure 5.1: Comparison of gross dental and craniofacial morphology.
(A) Lingual view of mandibular left molars in Control and *Evc2/Limbin*-cKO mutants. (B) Single tomographic images illustrating abnormal fusion of the two anteriormost molars in cKO mice. (C) Diagram indicating linear measurements with significant differences. Significantly increased measurements are shown in green and significantly decreased measurements are shown in red. (D) Graphs indicating measurements (also shown on C) with significant differences between Control and *Evc2/Limbin*-cKO mutants (N=4-5 at P28, * $p < 0.05$). Values are averages ± SD.

5.3.2 *Evc2/Limbin*-cKO mice have abnormal molar proportions

We previously reported incisor dysmorphology in this and another neural crest cell-specific *Evc2/Limbin*-cKO mouse model [31]. Molars of *Evc2/Limbin*-cKO mice at P28 were dysmorphic and appeared “bulbous” or taurodontic due to abnormal radicular and coronal proportions (Figure 5.2 A, B). Crown to root length ratio (measured in the incisocervical dimension) was significantly

larger in *Evc2/Limbin*-cKO mice suggesting the presence of either longer crowns or shorter roots (Figure 5.2 C). Reduced coronal buccolingual to mesiodistal length ratios further indicated that molar occlusal surfaces were rounder than those of their control counterparts (Figure 5.2 D). Though these trends (i.e., longer and rounder crowns) held true for most *Evc2/Limbin*-cKO mouse molars, changes in morphology were most pronounced in the second most anterior teeth in both arches. Coincidentally, these teeth were also the largest teeth in their respective arches (Figure Supplemental 5.5 A-H) suggesting that the observed morphologic changes could have a proportionate effect on chewing performance.

The ordinal difference between the largest molar tooth in *Evc2/Limbin*-cKO mice and their control counterparts (i.e., second most anterior vs. anteriormost, respectively) led us to reconsider the identity of each molar in *Evc2/Limbin*-cKO mice despite no change in total tooth number. Though discernible in both the maxillary and mandibular arches, morphologic differences were most apparent for the anteriormost mandibular molar (Figure 5.2 A, B). Although mice do not have premolars, this tooth (referred to as M_0) had proportions dissimilar to any *Evc2/Limbin*-cKO or control molars and consistently had a spherical crown and single, conical root – features similar to mandibular premolars described in other mammals [35]. Additional embryonic data suggesting that these anteriormost "molars" represent either vestigial premolars or abnormal tooth buds resulting from conditional *Evc2/Limbin* deletion led us to reorder *Evc2/Limbin*-cKO molars as M0-M1-M2 and speculate that M3 failed to develop (Figure 5.7). Because the identities of anteriormost (i.e., M0) and posteriormost (i.e., M3) molars remain suppositions based on current evidence, we only compared M1s and M2s as these were consistently present in both *Evc2/Limbin*-cKO and control mice.

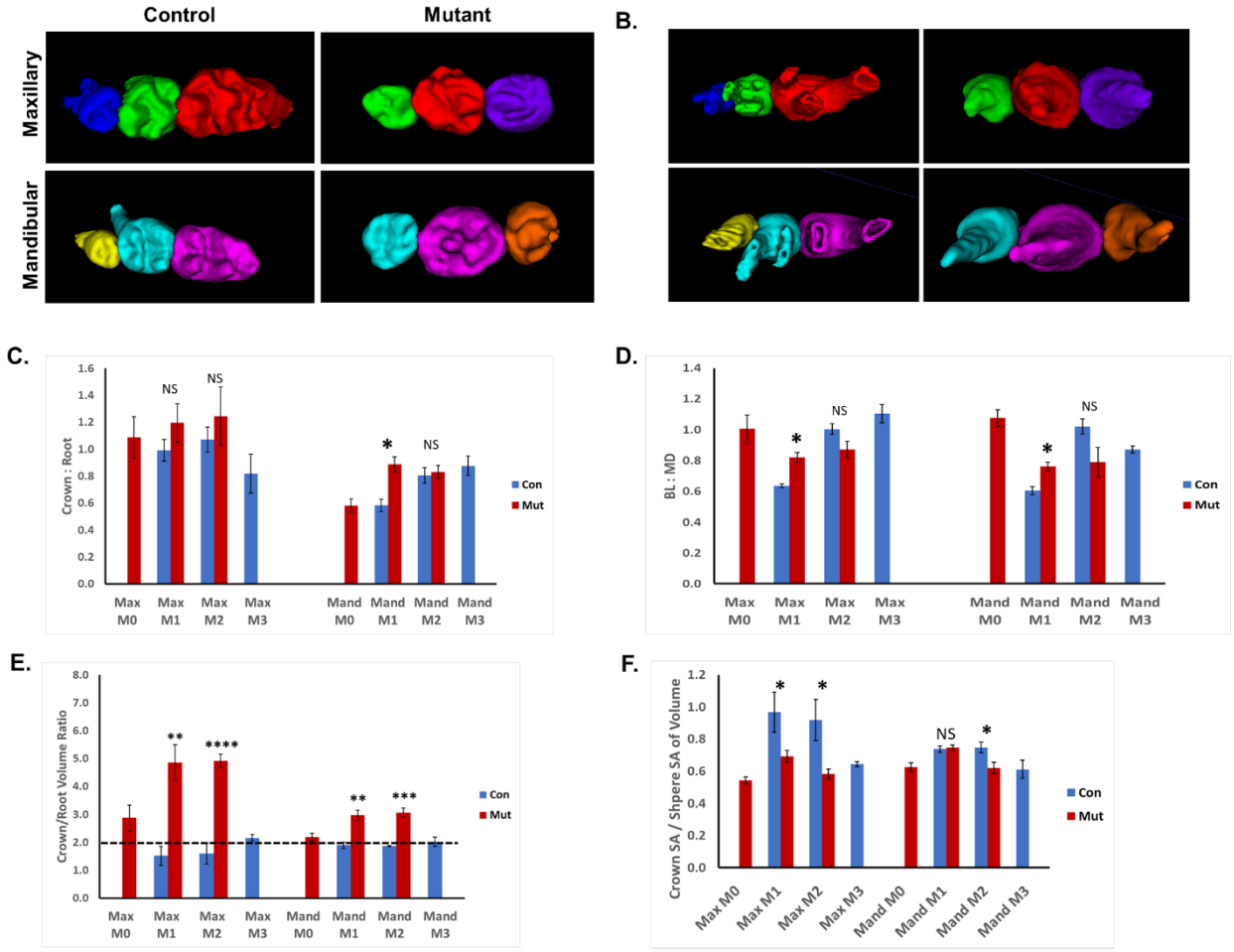

Figure 5.2: Differential molar morphology.
(A) Occlusal view of mandibular left molars (maxillary and mandibular) illustrating changes in crown morphology in Control and *Evc2/Limbin*-cKO mutants. (B) Incisal view of the same molars illustrating changes in root morphology. Graphs of molar measurements are as follows: (C) crown:root length ratio measured in the incisocervical direction, (D) buccolingual:mesiodistal length ratio, (E) crown:root volume, and (F) normalized coronal surface area. (N=4-5 for Control and *Evc2/Limbin*-cKO mutants at P28, respectively; * $p < 0.05$, ** $p<0.01$, *** $p<0.001$, **** $p<0.0001$). Values are averages ± SD.

5.3.3 Molar volumes are reduced in *Evc2/Limbin*-cKO mice

We next assessed molar coronal and radicular volumes to further confirm the basis of "bulbous" or taurodontic tooth appearance. Although all volumes (i.e., whole tooth, coronal, and radicular) were significantly smaller in *Evc2/Limbin*-cKO mice at P28, their significantly larger crown to root volume ratios indicated the presence of disproportionally large crowns (Figures 5.2

E and 5.5 E-G). However, this volume ratio disparity may have be compounded by root dysmorphology as those of *Evc2/Limbin*-cKO mice were consistently fused into a single, conical-like structure vs. the 3 or 2 roots seen in control maxillary and mandibular molars, respectively. The volumetric and linear measurement results suggest that *Evc2/Limbin* expression in neural crest cells plays a role in both overall tooth morphology (e.g., crown shape and root number) and root elongation. In the context of chewing performance, altered crown morphology could reduce the surface available for mechanical food reduction thereby decreasing efficiency.

5.3.4 Molar coronal surfaces are less complex in *Evc2/Limbin*-cKO mice

We next investigated coronal surface morphology as this represents the critical interfacial site between teeth and ingested material. Cusp identification in *Evc2/Limbin*-cKO molars was unreliable due to abnormal and irregular crown morphology. Linear measurements indicated that, compared to controls, *Evc2/Limbin*-cKO mice had reduced arch lengths and less coronal surface area (Figures 5.1 C-D and 5.5 H). These results were unsurprising considering the reduced molar size in *Evc2/Limbin*-cKO mice at P28 (Figure 5.5 A-G). However, normalization of surface area against crown volume revealed that *Evc2/Limbin*-cKO mice had less complex crown morphology, evidence suggestive of decreased mechanical reductive capacity (Figure 5.2 F). This trend of decreased surface complexity was consistent amongst *Evc2/Limbin*-cKO molars except for the second most anterior mandibular molar (M1) which had a characteristic deep pit in its distal half (Figure 5.2 A). Because molar morphologic analyses were performed at P28 (i.e., shortly after weaning and the transition to hard food), we assumed that any alterations in chewing functions (i.e., chewing rate or bite force) or efficiency represent fundamental outcomes of conditional *Evc2/Limbin* deletion-induced tooth morphologic changes.

5.3.5 Chewing rate is decreased in *Evc2/Limbin*-cKO mice

Mammalian mastication represents the cumulative output of coordinated interactions between the nervous system and craniofacial structures (i.e., jaws, teeth, and muscles of mastication). Because the muscles of mastication are non-neural crest derived, we first turned to chewing rate as a means of assessing whether NCC-driven anatomic (i.e., dental and craniofacial) variation results in oral functional changes. Sexually mature *Evc2/Limbin*-cKO mice at P120 chewed significantly slower and with more inter-cycle timing variation than their control counterparts (Figures 5.3 A and B). Fewer chews per unit time translates to lessened cumulative stress applied to ingested particles and thereby suggests decreased food reductive efficiency. However, chewing involves multiple inputs and additional functional evidence was needed to support this conclusion.

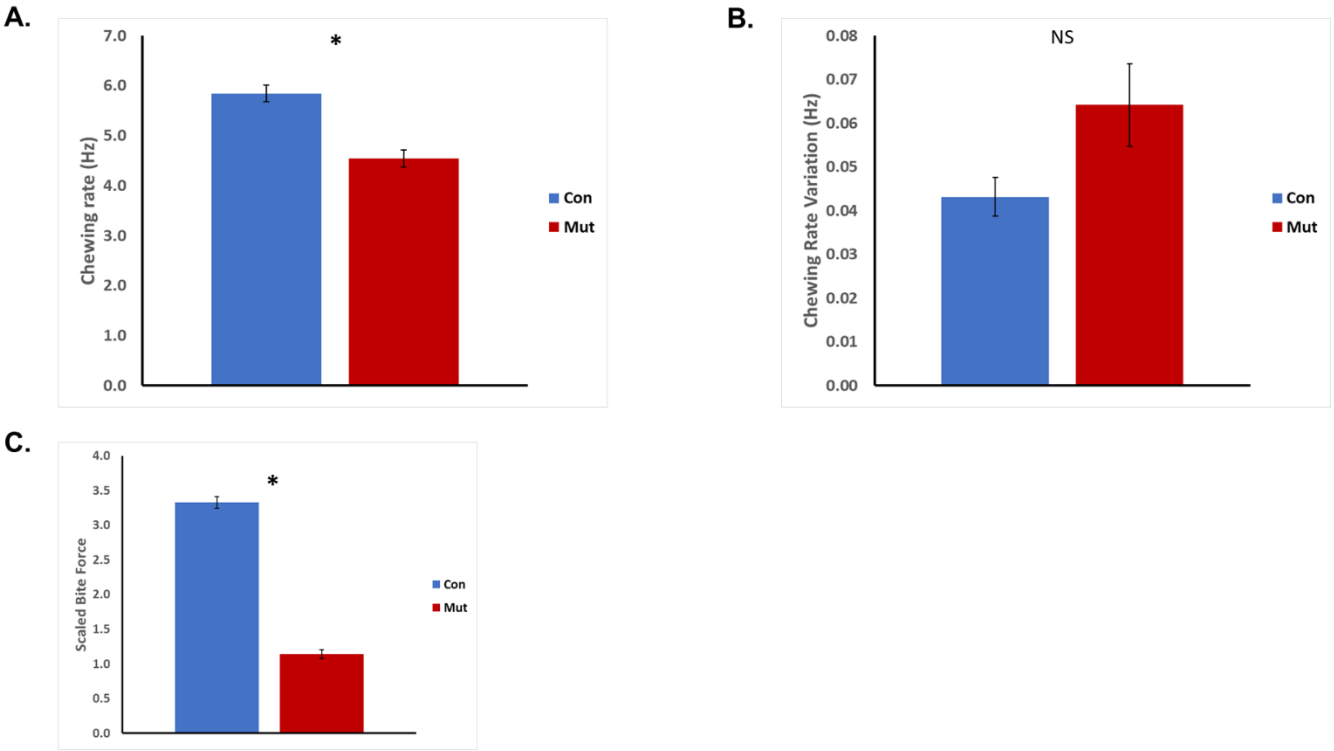

Figure 5.3: Oral performance measures in mature mice.

(A) Chewing rate of mice at P120. (B) Chewing rate variation (reported as SEM) in mice at P120. (C) Bite force of mice at P66. (N=4-6 for Control and *Evc2/Limbin*-cKO, respectively; * $p < 0.05$). Values are averages ± SD unless otherwise noted.

5.3.6 Bite force is reduced in *Evc2/Limbin*-cKO mice

Since mechanical reduction is affected by both the duration and magnitude (e.g., number of chews and force, respectively) of applied forces, we next assessed maximal bite force in *Evc2/Limbin*-cKO mice. Bite force of *Evc2/Limbin*-cKO mice was significantly reduced at P67 compared to their control counterparts (Figure 5.3 C). Though bite force scales with body size (i.e., greater bite force with increased body mass) and though *Evc2/Limbin*-cKO mice are ~30% smaller by body weight (Figure 5.6), the marked reduction in bite force defies established models and was interpreted as a representation of functional deficiency. This evidence also compliments chewing rate data and, since both involve the same craniofacial structures, further suggests that chewing efficiency should be compromised by *Evc2/Limbin*-deletion induced molar variation.

5.3.7 Fecal particle size is not affected in *Evc2/Limbin*-cKO mice

Molar morphologic and chewing functional data collectively suggest that chewing efficiency should be decreased in *Evc2/Limbin*-cKO mice. However, neither average fecal particle size nor particle distribution at P120 significantly differed between *Evc2/Limbin*-cKO and control mice (Figures 5.4 A and B). The similar values between experimental groups yet significant differences compared to undigested food (Figure 5.4 A and B) was surprising and insinuates the existence of a compensatory mechanism that occurs during either feeding or along the gastrointestinal system.

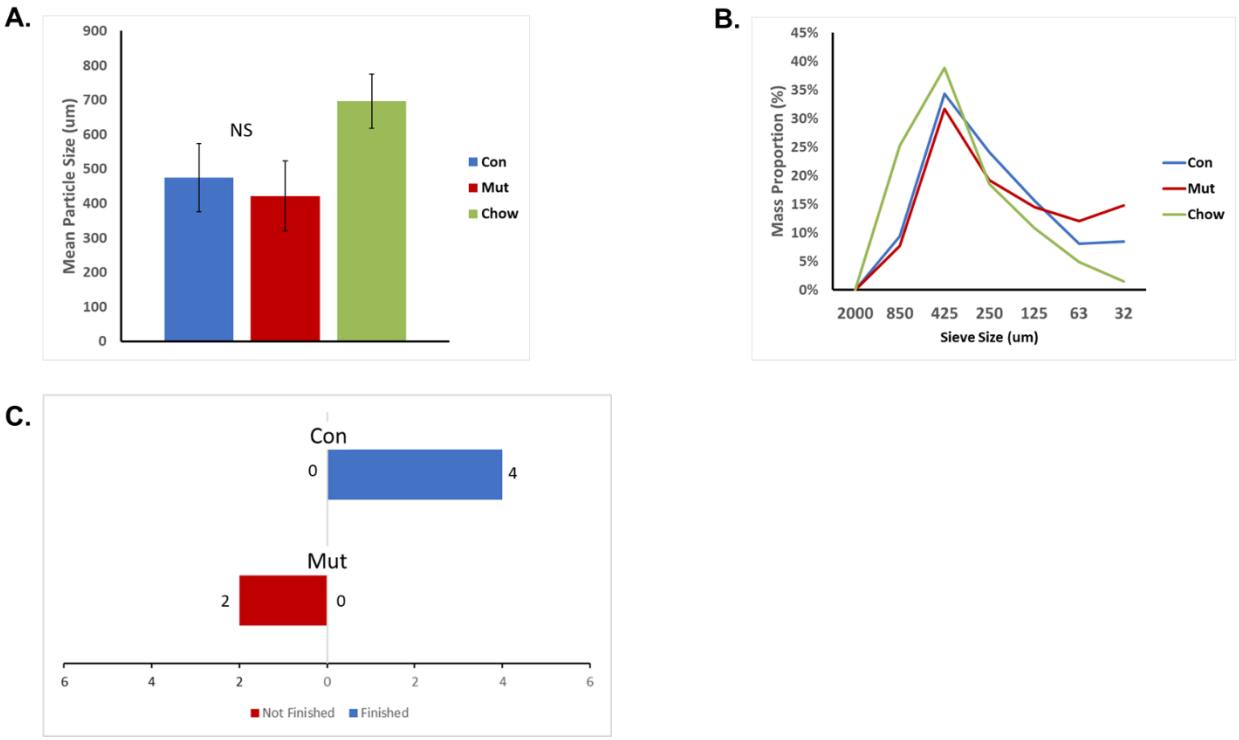

Figure 5.4: Measures of chewing performance in mature mice.
(A) Average fecal particle size of mice at P120 compared to standard chow diet. (B) Distribution of recovered particles within sorted feces and standard chow diet. (N=4 for Control and 6 for *Evc2/Limbin*-cKO, respectively; * $p < 0.05$). Values are averages ± SD (C) Number of individuals either finishing or not finishing a standardized food item (i.e., sunflower seed) during a 5 min food processing trial. (N=4 for Control and 2 for *Evc2/Limbin*-cKO, respectively)

5.3.8 Feeding bouts are increased in *Evc2/Limbin*-cKO mice

We finally sought to identify how *Evc2/Limbin*-cKO mice could be compensating for anatomic deficiencies. We turned to behavioral modification over gastrointestinal changes (e.g., gut motility) since *Evc2/Limbin* expression was conditionally disrupted in neural crest cells which widely contribute to structures of the head and neck region. Compared to controls, which were able to finish the given task within 5 min (4 out of 4), processing time for a given amount of food was significantly increased for the cKO (i.e., none of them finished processing the food within 5 min (2 out of 2)) (Figure 5.4 C). Therefore, *Evc2/Limbin*-cKO mice may compensate for less effective food reduction by spending more time feeding.

5.4 Discussion

This work used X-ray computed microtomography and digital segmentation to describe the 3-dimensional morphology of molars in *Evc2/Limbin*-cKO mice. While high resolution imaging is neither necessary nor feasible for most clinical cases, its application provided critical insight into the diminutive dental anatomic variations resulting from *Evc2/Limbin* deletion in neural crest cells. Tooth formation requires spatiotemporally coordinated interaction between cells of different origin (i.e., ectodermal-derived dental epithelium and neural crest-derived dental mesenchyme) [36,37]. Following prenatal crown completion, postnatal root formation begins with the apical migration and fusion of the inner and outer enamel epithelium into a structure called Hertwig's epithelial root sheath (HERS). The epithelial derived HERS subsequently affects root morphology as well as root dentin formation through its interaction with mesenchymal cells of the dental papilla [38,39]. Observed differences in both crown and root morphology in *Evc2/Limbin*-cKO mice suggests that *Evc2/Limbin* expression in neural crest cells is: (1) necessary for both prenatal crown development and postnatal root elongation and (2) secondarily affects non-NCC derived structures such as enamel. Though this study did not attempt to expound upon the mechanisms of NCC and non-NCC interaction in the teeth and craniofacial musculature, the importance of *Evc2/Limbin* during perinatal developmental stages critically aligns with our previous observations where *Evc2/Limbin*-cKO mouse incisor and midfacial dysmorphology is present shortly after birth and becomes progressively worse with postnatal age [31].

Evc2/Limbin-cKO mice provide a clinically relevant model of a human disease and tool for studying the oral functional outcomes following fundamental changes in craniofacial morphology. The recapitulation of molar phenotypes (e.g., taurodontic molars with conical roots) between human patients and *Evc2/Limbin*-cKO mice provides insights into the mechanism of

disease pathogenesis [18,19,40]. For example, previous studies have shown that Hedgehog (Hh) signaling is attenuated in a different (note: non-NCC specific) conditional knockout model for *Evc2/Limbin* [41]. Though it would be overly simplistic to attribute all phenotypic outcomes to disruptions in Hh signaling, Hh expression in the dental epithelium (note: non-NCC derived) is regulated by the NCC-derived dental mesenchyme and, critically, determines crown size and root length [42–44]. Disruptions in Hh signaling also affect tooth number and patterning thereby providing insight into the identity of anteriormost molars observed in this study [44,45]. Regardless, the presence of fundamental differences in dental morphology and prolonged survival of *Evc2/Limbin*-cKO mice to advanced ages — postnatal lethality is common is both human patients with EVC and conventional or global knockout mouse models — establishes them as a convenient tool for assessing oral function.

Interactions between mesodermal and neural crest-derived structures extend beyond perinatal dental and craniofacial development. In terms of functional interaction, none are more important for sustained survival than the rhythmic coordination between muscles, teeth, and jaws during feeding. Variables such as tooth number (e.g., total number and opposing or functional units) and quality (e.g., coronal anatomy and integrity) as well as chewing force, duration, and magnitude all affect the crushing efficiency that occurs during mastication [7,8]. Though most patients with EVC are described as having congenitally missing and/or abnormal teeth, changes in chewing efficiency would likely reflect anterior vs. posterior presentation patterns, specifically the bias towards misshapen posterior teeth (i.e., molars and premolars)[18,19]. Rhythmic food reduction occurs along the occlusal surfaces of posterior teeth which are misshapen, but do not differ in terms of total number or functional (i.e., opposing upper and lower tooth) units, in both human EVC patients and *Evc2/Limbin*-cKO mice. This molar phenotypic consistency and the

demonstration of reduced occlusal surface area in *Evc2/Limbin*-cKO mice further supports their use as a clinically relevant disease model and tool for elucidating the effects of finer scale tooth changes on chewing performance.

As previously mentioned, chewing effectiveness is a byproduct of dental anatomic form and function during chewing behaviors. Despite collective anatomic (i.e., molar shape and surface area) and functional evidence (i.e., decreased bite force and chewing rate) suggesting that chewing effectiveness would be reduced in *Evc2/Limbin*-cKO mice, the insignificant difference in average fecal particle size indicated that *Evc2/Limbin*-cKO mice compensated for their anatomical shortcomings. Chewing behavior adaptation in this study manifested as prolonged food processing time (i.e., greater total number of chews) since *Evc2/Limbin*-cKO mice were, unlike their control counterparts, unable to consume a single sunflower seed during a 5-minute feeding trial. Extended feeding bouts increase the period of tooth/food interaction and, in the absence of pre-processing (e.g., licking to soften food or using cutlery to mechanically reduce items), represent straightforward compensatory behavioral modifications employed by humans and non-human primates alike[11,46,47]. However, because feeding bout length represents a single component of chewing behavior, it would be interesting to assess per chew particle reduction since: (1) each cycle exponentially reduces food particle size within the ingested bolus and (2) significantly more or lesser quality chews (e.g., chewing stroke alterations) may indicate other sources of variation (e.g., pain)[8]. Regardless, both the limitations of modification and whether readouts assessed in this study represent function and/or efficiency in innate or non-adapted states requires further investigation. For example, enamel hypoplasia or structural abnormalities in the temporomandibular joint may cause physical discomfort thereby altering bite force and chewing rate. Variation in the muscle size and fiber orientations within the tongue and masticatory muscles

may also interfere with bolus manipulation and the generation of sufficient masticatory forces necessary for reduction.

In conclusion, we report changes in molar root and crown shape as well as decreased coronal complexity in a neural crest cell specific knockout mouse model for *Evc2/Limbin*. These mice attain similar measures of chewing efficiency and compensate for both structural and functional deficiencies (e.g., molar dysmorphology, decreased bite force, and reduced chewing rate) by increasing the length of feeding bouts. This detailed description of dental anatomic variation and oral function in an animal model of EVC provides a foundation for future studies regarding the functional outcomes of craniofacial dysmorphology.

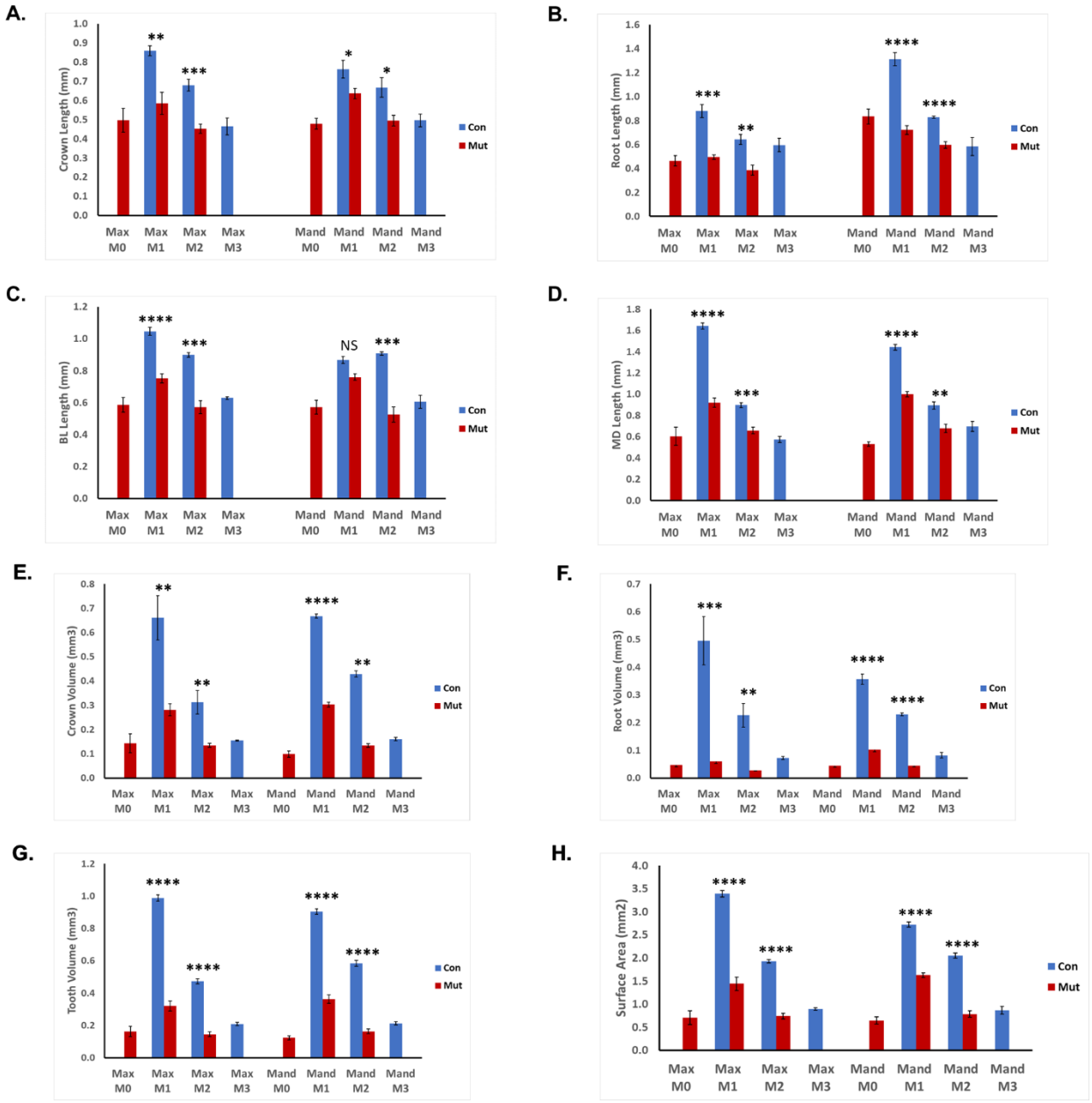

Figure 5.5: Non-normalized measurements

Graphs of measurements are as follows: (A) incisocervical crown length. (B) incisocervical root length, (C) maximal buccolingual molar width, (D) maximal mesiodistal molar length, (E) crown volume (mm^3), (F) root volume (mm^3), (G) whole molar volume (mm^3), (H) coronal surface area (mm^2). (N=4-5 for Control and *Evc2/Limbin*-cKO mutants at P28, respectively; * $p < 0.05$, ** $p<0.01$, *** $p<0.001$, **** $p<0.0001$). Values are averages ± SD.

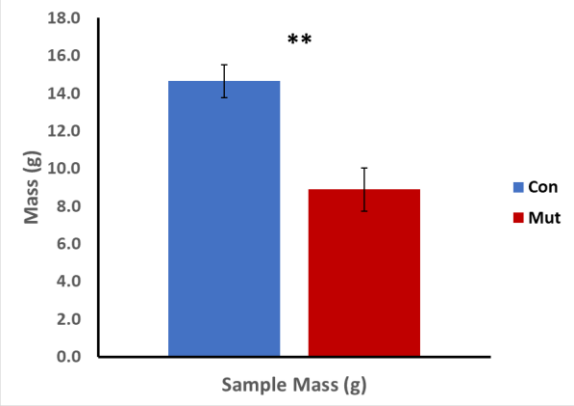

Figure 5.6: Comparison of Control and *Evc2/Limbin*-cKO body mass
Body mass of mice used for analysis. (N=4-5 for Control and *Evc2/Limbin*-cKO mutants at P28, respectively; * $p < 0.05$). Values are averages ± SD.

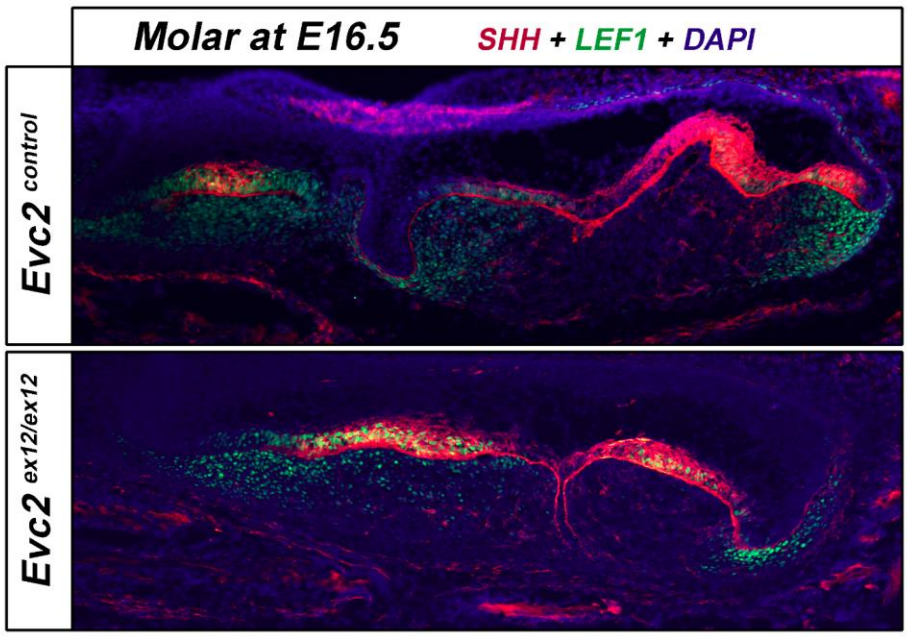

Figure 5.7: Ectopic anteriormost molar in *Evc2/Limbin*-cKO mice.
Immunofluorescence indicating the locations of SHH (red) and LEF1 (green) in the mandible at e16.5. SHH labels the enamel knot. LEF1 labels WNT signaling responsive cells within the dental mesenchyme. Anteriormost molar in *Evc2/Limbin*-cKO panel (bottom) is smaller and dysmorphic compared to the control counterpart (top).

5.5 References

1. Ansai T, Takata Y, Soh I, Akifusa S, Sogame A, Shimada N, et al. Relationship between chewing ability and 4-year mortality in a cohort of 80-year-old Japanese people. Oral Dis 2007;13:214–9. doi:10.1111/j.1601-0825.2006.01269.x.
2. Montes ABM, Oliveira TM De, Gavaio MBD, Barbosa T de S. Occlusal , chewing , and tasting characteristics associated with orofacial dysfunctions in children with unilateral cleft lip and palate : a case-control study. Clin Oral Investig 2018;22:941–50. doi:10.1007/s00784-017-2173-4.
3. Friedlander AH, Weinreb J, Friedlander I, Yagiela JA. Metabolic syndrome: Pathogenesis, medical care and dental implications. J Am Dent Assoc 2007;138:179–87. doi:10.14219/jada.archive.2007.0134.
4. Van Der Bilt A. Oral Rehabilitation Assessment of mastication with implications for oral rehabilitation : a review. J Oral Rehabil 2011;38:754–80. doi:10.1111/j.1365-2842.2010.02197.x.
5. Hiiemae KM. Feeding in Mammals. ACADEMIC PRESS; 2000. doi:10.1016/b978-012632590-4/50014-9.
6. Crompton AAW, Parker P. structures that distinguish them from reptiles Evolution of the Mammalian Masticatory Apparatus. Am Sci 1978;66:192–201.
7. van der Bilt A, Engelen L, Pereira LJ, van der Glas HW, Abbink JH. Oral physiology and mastication. Physiol Behav 2006;89:22–7. doi:10.1016/j.physbeh.2006.01.025.
8. Pérez-Barbería FJ, Gordon IJ. Factors affecting food comminution during chewing in ruminants: A review. Biol J Linn Soc 1998;63:233–56. doi:10.1006/bijl.1997.0183.
9. Fritz J, Streich WJ, Schwarm A, Clauss M. Condensing results of wet sieving analyses into a single data: A comparison of methods for particle size description. J Anim Physiol Anim Nutr (Berl) 2012;96:783–97. doi:10.1111/j.1439-0396.2011.01183.x.
10. Clauss M, Steuer P, Erlinghagen-Lückerath K, Kaandorp J, Fritz J, Südekum KH, et al. Faecal particle size: Digestive physiology meets herbivore diversity. Comp Biochem Physiol -Part A Mol Integr Physiol 2015;179:182–91. doi:10.1016/j.cbpa.2014.10.006.
11. Millette JB, Sauther ML, Cuozzo FP. Behavioral responses to tooth loss in wild ring-tailed lemurs (Lemur catta) at the Beza Mahafaly Special Reserve, Madagascar. Am J Phys Anthropol 2009;140:120–34. doi:10.1002/ajpa.21045.
12. Millette JB, Sauther ML, Cuozzo FP, Ness JL. The impact of dental impairment on ring-tailed lemur food processing performance. Am J Phys Anthropol 2012;148:238–48. doi:10.1002/ajpa.21571.
13. Laird MF, Vogel ER, Pontzer H. Chewing efficiency and occlusal functional morphology in modern humans. J Hum Evol 2016;93:1–11. doi:10.1016/j.jhevol.2015.11.005.
14. Poppi DP, Norton BW, Minson DJ, Hendricksen RE. The validity of the critical size theory for particles leaving the rumen. J Agric Sci 1980;94:275–80. doi:10.1017/S0021859600028859.
15. Schwarm A, Ortmann S, Fritz J, Flach E, Rietschel W, Clauss M. No distinct stratification of ingesta particles and no distinct moisture gradient in the fore-stomach of non-ruminants: The wallaby, peccary, hippopotamus, and sloth. Mamm Biol

2013;78:412–21. doi:10.1016/j.mambio.2013.04.001.
16. Ellis RWB, Van Creveld S. A syndrome characterized by ectodermal dysplasia, polydactyly, chondro-dysplasia and congenital morbus cordis: Report of three cases. Arch Dis Child 1940;15:65–84. doi:10.1136/adc.15.82.65.
17. da Silva EO, Janovitz D, de Albuquerque SC. Ellis-van Creveld syndrome: report of 15 cases in an inbred kindred. J Med Genet 1980;17:349–56.
18. Cahuana A, Palma C, Gonzáles W, Geán E. Oral manifestations in Ellis-van Creveld syndrome: Report of five cases. Pediatr Dent 2004;26:277–82.
19. Tuna EB, Koruyucu M, Kürklü E, Çifter M, Gençay K, Seymen F, et al. Oral and craniofacial manifestations of Ellis–van Creveld syndrome: Case series. J Cranio-Maxillofacial Surg 2016;44:919–24. doi:10.1016/j.jcms.2016.04.025.
20. Hanemann JAC, de Carvalho BCF, Franco EC. Oral manifestations in Ellis-van Creveld syndrome: report of a case and review of the literature. J Oral Maxillofac Surg 2010;68:456–60. doi:10.1016/j.joms.2009.07.026.
21. Naqash TA, Alshahrani I, Simasetha S. Ellis-van creveld syndrome: A rare clinical report of oral rehabilitation by interdisciplinary approach. Case Rep Dent 2018;2018. doi:10.1155/2018/8631602.
22. Ruiz-Perez VL, Ide SE, Strom TM, Lorenz B, Wilson D, Woods K, et al. Mutations in a new gene in Ellis-van Creveld syndrome and Weyers acrodental dysostosis. Nat Genet 2000;24:283–6. doi:10.1038/73508.
23. Ruiz-Perez VL, Tompson SW, Blair HJ, Espinoza-Valdez C, Lapunzina P, Silva EO, et al. Mutations in two nonhomologous genes in a head-to-head configuration cause Ellis-van Creveld syndrome. Am J Hum Genet 2003;72:728–32. doi:S0002-9297(07)60589-8 [pii].
24. Takeda H, Takami M, Oguni T, Tsuji T, Yoneda K, Sato H, et al. Positional cloning of the gene LIMBIN responsible for bovine chondrodysplastic dwarfism. Proc Natl Acad Sci U S A 2002;99:10549–54. doi:10.1073/pnas.152337899152337899 [pii].
25. Zhang H, Takeda H, Tsuji T, Kamiya N, Rajderkar S, Louie K, et al. Generation of Evc2/Limbin global and conditional KO mice and its roles during mineralized tissue formation. Genesis 2015;53:612–26. doi:10.1002/dvg.22879.
26. Ruiz-Perez VL, Blair HJ, Rodrigues-Andres ME, Blanco MJ, Wilson A, Liu YN, et al. Evc is a positive mediator of Ihh-regulated bone growth that localises at the base of chondrocyte cilia. Development 2007;134:2903–12. doi:10.1242/dev.007542.
27. Badri MK, Zhang H, Ohyama Y, Venkitapathi S, Alamoudi A, Kamiya N, et al. Expression of Evc2 in craniofacial tissues and craniofacial bone defects in Evc2 knockout mouse. Arch Oral Biol 2016;68:142–52. doi:10.1016/j.archoralbio.2016.05.002.
28. Mishina Y, Snider TN. Neural crest cell signaling pathways critical to cranial bone development and pathology. Exp Cell Res 2015;325:138–47. doi:10.1016/j.yexcr.2014.01.019.
29. Noden DM. The Role of the Neural Crest in Patterning of Avian Cranial Skeletal , Connective , and Muscle Tissues. Dev Biol 1983;96:144–65.
30. Kwon EK, Louie K, Kulkarni A, Yatabe M, Ruellas AC de O, Snider TN, et al. The Role of Ellis-Van Creveld 2(EVC2) in Mice During Cranial Bone Development. Anat Rec 2018. doi:10.1002/ar.23692.
31. Kulkarni AK, Louie KW, Yatabe M, De Oliveira Ruellas AC, Mochida Y, Cevidanes LHS, et al. A Ciliary Protein EVC2 / LIMBIN Plays a Critical Role in the Skull Base for

Mid-Facial Development. Front Physiol 2018;9:1–13. doi:10.3389/fphys.2018.01484.
32. Ziermann JM, Diogo R, Noden DM. Neural crest and the patterning of vertebrate craniofacial muscles. Genesis 2018;56. doi:10.1002/dvg.23097.
33. Zhang H, Takeda H, Tsuji T, Kamiya N, Rajderkar S, Louie K, et al. Generation of Evc2/Limbin global and conditional KO mice and its roles during mineralized tissue formation. Genesis 2015;53:612–26. doi:10.1002/dvg.22879.
34. Danielian PS, Muccino D, Rowitch DH, Michael SK, McMahon AP. Modification of gene activity in mouse embryos in utero by a tamoxifen-inducible form of Cre recombinase. Curr Biol 1998;8:1323–6.
35. Ota MS, Nakahara T, Kanri Y, Kozawa Y, Ohazama A, Aoba T, et al. Patterning of Molar Tooth Roots in Mammals. J Oral Biosci 2009;51:193–8. doi:10.1016/S1349-0079(09)80003-0.
36. Lungová V, Radlanski RJ, Tucker AS, Renz H, Míšek I, Matalová E. Tooth-bone morphogenesis during postnatal stages of mouse first molar development. J Anat 2011;218:699–716. doi:10.1111/j.1469-7580.2011.01367.x.
37. Thesleff I, Hurmerinta K. Tissue Interactions in Tooth Development. Differentiation 1981;18:75–88. doi:10.1111/j.1432-0436.1981.tb01107.x.
38. Kim TH, Bae CH, Lee JC, Ko SO, Yang X, Jiang R, et al. β-Catenin is required in odontoblasts for tooth root formation. J Dent Res 2013;92:215–21. doi:10.1177/0022034512470137.
39. Li J, Parada C, Chai Y. Cellular and molecular mechanisms of tooth root development. Dev 2017;144:374–84. doi:10.1242/dev.137216.
40. Da Silva EO, Janovitz D, Cavalcanti De Albuquerque S. Ellis-van Creveld syndrome: Report of 15 cases in an inbred kindred. J Med Genet 1980;17:349–56. doi:10.1136/jmg.17.5.349.
41. Zhang HH, Kamiya N, Tsuji T, Takeda H, Scott G, Rajderkar S, et al. Elevated Fibroblast Growth Factor Signaling Is Critical for the Pathogenesis of the Dwarfism in Evc2/Limbin Mutant Mice. Plos Genet 2016;12. doi:ARTN e100651010.1371/journal.pgen.1006510.
42. Liu Y, Feng J, Li J, Zhao H, Ho TV, Chai Y. An Nfic-hedgehog signaling cascade regulates tooth root development. Dev 2015;142:3374–82. doi:10.1242/dev.127068.
43. Nakatomi M, Morita I. Sonic Hedgehog Signaling is Important in Tooth Root Development. J Dent Res 2006;85:427–31.
44. Dassule HR, Lewis P, Bei M, Maas R, McMahon AP. Sonic hedgehog regulates growth and morphogenesis of the tooth. Development 2000;127:4775–85.
45. Seo H, Amano T, Seki R, Sagai T, Kim J, Cho SW, et al. Upstream Enhancer Elements of Shh Regulate Oral and Dental Patterning. J Dent Res 2018;97:1055–63. doi:10.1177/0022034518758642.
46. Zelig R, Jones VM, Touger-Decker R, Hoskin ER, Singer SR, Byham-Gray L, et al. The Eating Experience: Adaptive and Maladaptive Strategies of Older Adults with Tooth Loss. JDR Clin Transl Res 2019;4:217–28. doi:10.1177/2380084419827532.
47. Mishellany-Dutour A, Renaud J, Peyron MA, Rimek F, Woda A. Is the goal of mastication reached in young dentates, aged dentates and aged denture wearers? Br J Nutr 2008;99:121–8. doi:10.1017/S0007114507795284.

Chapter 6: Summary and Future Work

6.1 Regulation of Complex Tissue Regeneration

Based on our previous studies (Chapter 1.2) indicating the occurrence of cellular reprogramming following craniofacial muscle injury, we utilized an unbiased high throughput approach to identify how this process is temporally regulated at the transcriptional level (Chapter 2). This work not only investigated a novel regeneration model and modality that circumvents an inherent issue (i.e., lack sufficient numbers of replacement cells) of many tissue engineering approaches, but challenged the prevailing notion that regeneration recapitulates embryonic development (Chapter 3).

Analysis of differentially expressed genes (DEG) at two time points early in the muscle regeneration process (i.e., 9 and 18 hours post injury (hpi)) allowed us to identify over 6000 candidates that could play a role in craniofacial muscle regeneration. Due to the large number of candidates, we next applied two types of gene annotation analyses (i.e., gene ontology (GO) terms and Kyoto Encyclopedia of Genes and Genomes (KEGG) pathways) and discovered consistency between the results. Convinced of the validity of annotation-based conclusions, we then sought to identify pathways that supported published observations and mechanisms within our muscle regeneration model. Downregulated terms and pathways included those involved in muscle differentiation, development, and function – reassuring findings considering the loss of myocyte identity and muscle-to-mesenchymal transition observed in the injured muscle stump. Upregulated terms and pathways included catabolic and lysosomal processes – also reassuring findings considering the necessity of autophagy in our muscle regeneration model.

Though subsequent clustering of DEG based on temporal expression patterns further validated our regeneration model, the identification of transiently upregulated genes critically revealed that epigenetic modification may underlie myocyte reprogramming. Genes within the "transient upregulation" group (i.e., differential expression only at 9hpi) included known epigenetic regulators including *ezh2*, *prmt5,* and *prmt7*. *In vivo* knockdown experiments revealed that these genes were necessary for both cellular reprogramming – assessed as the percentage of proliferating myoblast-like cells present – and anatomic regeneration. This differed from a "late upregulation" (i.e., differential expression at 18hpi) gene such as the extracellular matrix component *fn1a* which was necessary for anatomic regeneration but not cellular reprogramming.

Also among the "transient upregulation" cluster of DEG were those encoding twist transcription factors, elements known to affect craniofacial muscle development and epithelial to mesenchymal transitions during tumorigenesis. Of the 4 zebrafish twist paralogs (i.e., *twist1a*, *twist1b*, *twist2*, and *twist3*), we discovered that only *twist3* was necessary for adult muscle regeneration and did so by affecting early steps (i.e., cellular reprogramming as assessed by myoblast proliferation) during this process. This role differed from *twist1a*, *twist1b*, and *twist2* which were previously shown to affect craniofacial morphology and which we demonstrated were necessary for embryonic extraocular muscle development. Results from this work not only support the potential of our identified DEG as targets for regenerative therapies but suggest that, despite subfunctionalization amongst paralogs, twist transcription factors have an evolutionarily conserved role during myogenesis.

6.2 Craniofacial Dysmorphology and Oral Functional Outcomes

Using our unique mouse model of a rare human genetic disorder (Chapter 1.1), we investigated the etiology of craniofacial dysmorphology (Chapter 4) using a combined

cephalometric and tomographic imaging approach. The midfacial phenotypic similarities between our model and human patients with Ellis-van Creveld syndrome (EVC) further supported its clinical relevance and led us to consider additional utility as a tool for assessing oral function in fundamentally altered craniofacial states. Novel analyses of molar morphology and chewing effectiveness (Chapter 5) revealed how animals compensate for suboptimal craniofacial morphology and may provide insight into rehabilitation strategies and functional assessments in similarly affected human patients.

Conventional or global knockout (KO) mouse models of EVC recapitulate many human disease signs, including high levels of postnatal lethality. We circumvented this issue and studied the role of a causative gene (i.e., *Evc2*) in the craniofacial region by conditionally knocking it out (cKO) in neural crest-derived cells. Cephalometric analyses at multiple time points (i.e., postnatal days P8 and P28) and using two different neural crest-specific Cre-recombinase divers (i.e., *Wnt1-Cre* and *P0-Cre*) demonstrated differences in skull shape and facial profile which, generally, became worse with advancing age. Significantly different angular and linear measurements between the skulls of cKO and control mice predominantly involved structures within the neurocranium and viscerocranium, regions with significant contributions from neural crest cells. These changes in craniofacial measurements within both cKO mouse lines were also comparable KO mice suggesting that *Evc2* expression in neural crest cells is important during craniofacial development.

Despite superficial similarities between *Wnt1-Cre* and *P0-Cre* mice at P8, more widespread angle-based craniofacial dysmorphology in *Wnt1-Cre* mice at P28 led us to investigate the etiology of these differences. Shape-based analyses indicated significant shortening of the neural crest-derived anterior skull base coincident with premature fusion of the intrasphenoidal

synchondrosis. These results were also supported by higher recombination efficiency within the anterior skull base of *Wnt1-Cre* mice. Considering how the skull base serves as the connector between posterior and anterior skull elements and its effects upon facial profile, we concluded that skull base deficiencies secondarily lead to midfacial dysmorphology in both *Evc2*-cKO mice and human EVC patients.

After establishing *Evc2*-cKO mice as a clinically relevant model with fundamental changes in craniofacial morphology, we then used it as a tool to investigate the relationship between form and function within this region. Mastication represented a convenient readout of complex interactions between neural crest and non-neural crest derived structures (e.g., jaws, teeth, and masticatory muscles) and parameters such as bite force and chewing rate were significantly decreased in *Evc2*-cKO mice. Shape-based analysis of molar teeth also confirmed taurodontism and indicated reduced coronal surface area complexity. However, the insignificant differences in chewing efficiency suggest that animals compensated for anatomic shortcomings via behavioral modification (i.e., increase feeding bout length). Results from this work thereby provide insight into the adaptive strategies used to sustain function and, ultimately, survival following changes in craniofacial morphology.

6.3 Future Work

The work in this dissertation sought to address the need to achieve both anatomic regeneration and restoration of function following congenital or traumatic changes in craniofacial morphology. Investigation into the temporal regulation of adult tissue regeneration and gene subfunctionalization has led to the identification of multiple pathways that represent potentially druggable targets for future regenerative therapies. Assessment and characterization of the

functional outcomes in states of congenital craniofacial dysmorphology provide insight into form-function relationships and represent potential metrics by which successful rehabilitation may be measured. However, future studies must further elucidate the mechanisms underlying tissue regeneration as well as assess adaptation by evaluating function at various developmental or post-acute injury time points.

Knockdown experiments provided the phenotypic validation necessary to conclude that specific DEG were important during the muscle regeneration process. However, time availability and the lack of reactive anti-zebrafish antibodies precluded comprehensive testing of all 6000 DEG. Epigenetic modifications present attractive targets for future studies and/or therapeutics considering: (1) overrepresentation of the GO term "regulation of gene expression, epigenetic" within our gene set and (2) the demonstrated importance of genes (i.e., *ezh2* and *suz12a*) involved in histone methylation and epigenetic silencing. The reversible nature of epigenetic modifications also fits the narrative of cellular reprogramming while conserved chromatin structure across species allows antibody-based validation of translational knockdown. Specific targets of interest include the likes of *prmt1* and *hdac1* – genes involved in histone methylation and deacetylation machinery, respectively – as well as zebrafish paralogs of pluripotency markers (e.g., *myca* and *mycb*).

Our functional investigation using *Evc2*-cKO mice suggested that changes in molar morphology and surface characteristics were associated with decreases in chewing metrics (i.e., bite force and chewing rate). However, these changes were seemingly compensated for by increased food processing time (i.e., chewing bout) resulting in non-significant changes in average fecal particle size or distribution. Whether changes in tooth morphology or chewing performance (i.e., bite force and chewing rate) inherently affect chewing effectiveness requires further

investigation. Issues that must be addressed are: (1) the temporal development of compensatory mechanisms and (2) effect of acute (e.g., mechanically induced) changes to coronal anatomy. Chewing metrics and performance were assessed in sexually mature mice that had been feeding on standard chow for >2months. Because mice could have potentially developed compensatory behaviors over this time, it is necessary to repeat testing at an early point (e.g., P28 or shortly after weaning) to determine the presence or absence of innate functional deficiency. A complimentary approach to additional testing of cKO mice would be to induce acute changes (e.g., tooth extraction or occlusal reduction) and assess functional outcomes immediately following modification. These experiments are important next steps to uncovering the relationship between oral form and function using our mouse model.

In conclusion, the work in this dissertation uses two vastly different models united under the overall goal of uncovering the basis of craniofacial muscle regeneration leading to restoration of chewing function. Application of and insight gained by using these tools establishes an influential platform for discovery that extends beyond the gateway of the mouth.